

PERFORMANCE EFFECTS OF DISSOCIATED HYDROGEN IN
NUCLEAR THERMAL PROPULSION ENGINES

By

Richard Adam Gorrell

Bachelor of Science – Aerospace Engineering
Missouri University of Science & Technology
2004

Master of Engineering – Space Operations
University of Colorado, Colorado Springs
2010

Master of Science – Operational Art and Strategy
Air University
2016

A dissertation submitted in partial fulfillment
of the requirements for the

Doctor of Philosophy – Mechanical Engineering

Department of Mechanical Engineering
Howard R. Hughes College of Engineering
The Graduate College

University of Nevada, Las Vegas
May 2024

Dissertation Approval

The Graduate College
The University of Nevada, Las Vegas

May 6, 2024

This dissertation prepared by

Richard Adam Gorrell

entitled

Performance Effects of Dissociated Hydrogen in Nuclear Thermal Propulsion Engines

is approved in partial fulfillment of the requirements for the degree of

Doctor of Philosophy – Mechanical Engineering
Department of Mechanical Engineering

Yi-Tung Chen, Ph.D.
Examination Committee Chair

Hui Zhao, Ph.D.
Examination Committee Member

Alexander Barzilov, Ph.D.
Examination Committee Member

Jeremy Cho, Ph.D.
Examination Committee Member

Balakrishnan Naduvalath, Ph.D.
Graduate College Faculty Representative

Alyssa Crittenden, Ph.D.
*Vice Provost for Graduate Education &
Dean of the Graduate College*

Abstract

PERFORMANCE EFFECTS OF DISSOCIATED HYDROGEN IN NUCLEAR THERMAL PROPULSION ENGINES

By

R. Adam Gorrell

Dr. Yitung Chen, Advisory Committee Chair

Professor and Chair, Department of Mechanical Engineering

University of Nevada, Las Vegas

Nuclear thermal propulsion (NTP) research considers hydrogen dissociation as negligible to design and analysis of propulsion engines. This study reintroduces chemically reacting flow to NTP engine analysis for investigation of the dissociation effect on engine performance. A first-principles approach observes the basic chemical mechanism and reaction within the high-speed, high-temperature NTP flow to baseline expected atomic hydrogen levels and validate equilibrium. A surface reaction study looks into hydrogen absorption through dissociation and its effect on the boundary layer, and bulk flow. For total performance, the resulting dissociated flow is analyzed through nozzle expansion and performance metrics calculated.

All historic reactor inlet conditions can be assumed to be at equilibrium for atomic hydrogen values at, or below, 1% and remain at equilibrium until approximately 1600 K. Beyond this temperature, all reactors operated in non-equilibrium at worst conditions of sonic velocity, with one reactor operating as low as 51% of equilibrium but converged toward equilibrium at the outlet. All historic NTP reactors correlated with equilibrium at reactor outlet within 82%. Hydrogen dissociation is present in all historic NTP reactors, but all atomic hydrogen levels were

below 0.5% molar fraction of total concentration when considering bulk flow temperatures and any speed up to the sonic speed.

Historic reactors demonstrate that similar NTP systems must consider non-equilibrium near the outlet above 1600 K as well as if the flow is disrupted from trace amounts below 1600 K. Highest core exit temperatures contains the highest dissociated atomic hydrogen while highest operating pressures cause the reactor to closely follow equilibrium. Reactor inlets that contain less than 1% molar fraction atomic hydrogen can be assumed to reach equilibrium by the reactor outlet.

NTP reactors contain a notable crossflow velocity near the reactor outlet due to the absorption of hydrogen into the NTP cladding material. Tungsten is selected as the cladding of choice due to concerning indications of high hydrogen penetration rates in molybdenum-tungsten (Mo-W) alloy. Zirconium carbide (ZrC) was rejected due to its historic issues with mass loss and carbon chemical reaction but proves to be a promising future candidate. The effects of the boundary layer were in questions as crossflow velocity reached 80 mm/s into NTP cladding resembling a form of wall suction. The absorption of hydrogen has a small effect on the thermal boundary layer. This demonstrated that the fluid mechanics of NTP reactors must consider the surface reaction of dissociated hydrogen flow in design and optimization of NTP engines. A follow-on computational fluid dynamics (CFD) looked closely at the boundary layer effects, assuming wall transpiration of hydrogen and provide the most accurate velocity and mass flow rates exiting the reactor and entering the chamber.

A 2-D axisymmetric computational fluid dynamics (CFD) model of the KIWI 4BE nuclear reactor provided the highest quality of chamber conditions for NTP. Atomic hydrogen was found to double over simple 1-D assumptions assuming equilibrium, equilibrium conditions, and assuming centerline temperature. For the KIWI 4BE model, 0.7% molar fraction of atomic

hydrogen entered the NTP “Chamber” accompanied by a significant velocity decrement of 7% less than non-chemically reacting assumptions. The thermal profile changes appear relatively insignificant while the “1/7th” turbulent velocity profile was not accurate and needs further update. Analysis of zirconium carbide indicated that hydrogen absorption maybe greatly suppressed but further operational conditions are needed for testing. Further computations were completed in 1-D rocket nozzle expansion to fully understand the performance effect.

Calculation of the changing atomic hydrogen level requires a chemical analysis throughout nozzle expansion. NASA Chemical Equilibrium Analysis Application provides the tools to complete this analysis. The specific impulse is found for the chemically reacting flow and non-chemically reacting flow cases and compared. The specific impulse demonstrates the superior efficiency of the KIWI B4E engine over liquid engines. Despite reduced velocity and increased atomic hydrogen, the chemically reacting flow model produced a slight increase in specific impulse of 0.9% over the non-chemically reacting flow model. Modeling of NTP engines will underestimate the engine performance if chemically reacting flow is not considered.

Acknowledgements

I'd like to thank Dr. Yitung Chen for his guidance, flexibility, and mentorship over the last four years. Dr. Chen taught me the focus of a Ph.D. and challenged me to hone my research questions and pursue a rich and confident survey of literature to support my work and extend the body of knowledge. He continually allowed non-standard meeting times and weekend reviews to support my full-time active-duty Air Force career. I particularly appreciate his professional academic mentorship in my job search and credentialing so that I could become a college professor myself. I hope to emulate his teaching principles and guidance for my future Ph.D. students. I want to thank him for reviewing my manuscripts and this dissertation. My family and I are profoundly and forever grateful for his immense support.

I want to thank my dissertation committee members, Dr. Hui Zhao, Dr Alexander Barzilov, Dr. Jeremy Cho, and Dr. Balakrishnan Naduvalath, for their time and insightful comments.

I can't begin to express my appreciation for the patience and support of my family during four years of "nights and weekends," all spent to earn my Ph.D. while also working full-time. Their love and dedication were extreme, and I look forward to supporting them in the coming years. It's Dad's turn to do the dishes.

Dedication

To my wife who supports me, and my daughters, asking nothing in return. I have no success without her support. Her care, compassion, and grace are endless. I love you, Natalie.

Table of Contents

Abstract	iii
Acknowledgements.....	vi
Dedication.....	vii
List of Tables.....	xii
List of Figures.....	xiii
List of Nomenclature	xv
Chapter 1 Overview, Literature Review, and Primer on NTP	1
1.1. Overview	1
1.2. A Primer on Nuclear Thermal Propulsion (NTP)	2
1.3. Surface Reactions included with Bulk Flow Reactions	6
1.4. Reactor Outlet Study for Rocket Chamber Conditions	9
Chapter 2 Equilibrium Validation of Dissociation in NTP	13
2.1. The Elementary Chemical Reaction Mechanism of Hydrogen Dissociation	13
2.2. Literature Review for the Correct Chemical Reaction Mechanism	15
2.3. Assumed Conditions in the NTP Reactor	20
2.4. Non-Equilibrium Considerations of NTP Reactors	24
2.5. Existence of Atomic Hydrogen in Historic NTP Reactors	30
Chapter 3 Surface Reaction Dissociation and Impact on NTP Flow	36
3.1. Materials and Methods	36
3.2. Theory	38
3.2.1 Adsorption Equation.....	38

3.2.2	Desorption Equation	41
3.2.3	Absorption Equation	42
3.2.4	Mass Flow, Calculation of v_w into Wall	42
3.3.	Findings/Results	43
3.3.1	Coverage Decreases with Increasing Surface Temperature and Gas Temperature	43
3.3.2	Coverage Approaches $\theta_{eq} = 0$ beyond 2000 K.....	45
3.3.3	Crossflow is Maximum at NTP Reactor Outlet	46
3.4.	Discussion	48
Chapter 4	CFD Analysis of Dissociation Reactions in NTP Flow	55
4.1	Methods and Measurements	55
4.1.1	Basic CFD Geometry Setup and Boundary Condition Assumptions.....	55
4.1.2	Rejection of LES and Selection of RANS	55
4.1.3	Solution Steering.....	56
4.1.4	RANS Convergence and the Transient State	56
4.1.5	Selection of the Pseudo-transient Method	57
4.2	Theory	58
4.2.1	Compressible, Reynolds-Averaged Navier-Stokes Equations	58
4.2.2	Species Conservation.....	59
4.2.3	Selection of $k - \omega$ SST Model.....	59
4.2.4	Calculation of y^+ for Placement.....	60
4.3	Results	60

4.3.1	Temperature and Velocity Boundary Layer Development of the Chemically Reacting Flow	60
4.3.2	Atomic Hydrogen near Reactor Outlet	64
4.4	Discussion	65
4.4.1	Atomic Hydrogen Species Profile	65
4.4.2	Total Temperature Remains Relatively Unchanged between the Cases.	67
4.4.3	Boundary Layer Average Velocity is Reduced from Non-Chemically Reacting Flow	69
4.4.4	ZrC Cladding as a Superior Cladding.....	73
4.4.5	Reactor Channel CFD Performance.....	74
Chapter 5 NTP Rocket Performance with Dissociated Hydrogen Chamber Conditions.....		76
5.1	Methods and Measurements	76
5.1.1	NASA Chemical Equilibrium Analysis (CEA) for Rocket Applications.....	76
5.1.2	Finite Area Combustor Analysis	76
5.1.3	NTP Property Alignment with Combustor Outlet.....	77
5.2	Theory	77
5.2.1	Non-chemically Reacting Flow versus Chemically Reacting Equilibrium and Frozen Flow	77
5.2.2	Nozzle Expansion is Isentropic with Chemical Reactions	78
5.3	Results	80
5.3.1	Specific Impulse.....	80
5.3.2	Atomic Hydrogen Recombination in Nozzle.....	81

5.4 Discussion	81
5.4.1 Specific Impulse Increase in Efficiency	81
5.4.2 Superiority of Specific Impulse to Liquid Engines	82
Chapter 6 Conclusions and Future Works	83
References	86
Curriculum Vitae	98

List of Tables

Table 1. KIWI-4BE operating conditions	4
Table 2. Plasma Arrhenius equations and expression	13
Table 3. Statistical thermodynamic speed of sound of equilibrium hydrogen.....	22
Table 4. Historic NTP reactors & equilibrium behaviors of disassociated atomic hydrogen	34
Table 5. White’s exploration of porous pipe flow.....	53
Table 6. Timescale of the various flow phenomena.....	57
Table 7. Cross-section locations for analysis along reactor	62
Table 8. CEA calculations at throat and supersonic expander exit for KIWI B4E with chemically reacting flow	80

List of Figures

Fig. 1. KIWI-4BE overview design and fuel element schematics	4
Fig. 2. Schematic of NTP reactor.....	5
Fig. 3. Velocity and thermal boundary layer within a pipe flow.....	5
Fig. 4. Hydrogen adsorption, desorption, and absorption phenomena	6
Fig. 5. Culmination of NTP channels in chamber with supersonic expander.....	11
Fig. 6. Reaction rate coefficient comparison for model selection	15
Fig. 7. Finite-rate equilibrium at relaxation times compared to thermodynamic/Gibbs equilibrium	18
Fig. 8. Depiction of control volume.....	19
Fig. 9. Considered NTP reactor temperature profiles	23
Fig. 10. Dissociation reaction rates at various molar atomic hydrogen and temperature levels...	25
Fig. 11. Percentage of control volume in non-equilibrium up to 100%.....	27
Fig. 12. KIWI-4BE reactor dissociation line within a reaction rate field.....	29
Fig. 13. Expansion of equilibrium zone at slower flow speeds for Mach 0.5 (left) and Mach 0.1 (right)	30
Fig. 14. Rise to equilibrium for varying temperature profiles	32
Fig. 15. Disturbances in high non-equilibrium reaching equilibrium at reactor outlet.....	35
Fig. 16. Initial sticking coefficient of tungsten for NTP reactor incident temperatures	40
Fig. 17. Adsorption/desorption equilibrium levels on tungsten cladding	44
Fig. 18. Surface coverage of hydrogen at equilibrium as a percent of saturation.....	45
Fig. 19. Crossflow velocity due to hydrogen absorption	47
Fig. 20. Stanton numbers for various F values	50

Fig. 21. Velocity profiles for various F values.....	51
Fig. 22. Plot of total temperature at percentage of circular duct radii	61
Fig. 23. Thermal boundary profile at selected cross sections along the axis of the reactor.....	63
Fig. 24. Turbulent boundary layer profile at selected cross sections along the axis of the reactor.	64
Fig. 25. Molecular hydrogen species molar fraction (X_{H_2}) throughout reactor. Atomic hydrogen species molar fraction is $1 - X_{H_2}$	65
Fig. 26. Atomic hydrogen species profile approaching the chamber.....	66
Fig. 27. Temperature difference between non-chemically reacting and chemically reacting flow. Non-Chemically reacting flow was always higher than chemically reacting flow indicated by a positive temperature difference.....	68
Fig. 28. Increasing thermal conductivity in the boundary layer	69
Fig. 29. Velocity difference between non-chemically reacting and chemically reacting flow. Non- Chemically reacting flow was always higher than chemically reacting flow indicated by a positive velocity difference.....	70
Fig. 30. Radial velocity in the region of significant absorption under chemically reacting flow.	71
Fig. 31. Comparison of turbulent boundary layer at same locations under chemically reacting flow. Velocity is normalized by V_{max} at centerline flow.	72
Fig. 32. Absorption coefficient comparison between tungsten cladding (dashed line) versus zirconium cladding as colored lines calculated absorption coefficients from literature.....	74
Fig. 33 Reactor channel, chemically reacting, CFD results with increasing grid resolution at inlet, middle, and outlet.....	75
Fig. 34. Notional “combustion chamber” finite area between stations 1 and 4.....	77

List of Nomenclature

Letters

A	Cross sectional area, m^2
A^*	Cross sectional area of nozzle throat, m^2
A	Surface area of the NTP cladding, m^2
a	Speed of sound, $m\ s^{-1}$
a_e	Speed of sound, thermodynamic equilibrium, $m\ s^{-1}$
C	Concentration, $mol\ m^{-3}$
$CV_{\%}$	Control volume percentage
C_T	Total concentration, $mol\ m^{-3}$
D	Hydraulic diameter, m
D	Diffusion coefficient, $m^2\ s^{-1}$
e	Electron
e	Specific energy, $J\ kg^{-1}$
E	Activation energy, $J\ mol^{-1}$
E_d	Desorption energy, $J\ mol^{-1}$
F	Ratio of wall velocity to freestream velocity
ΔG_0	Gibbs free energy of formation, $J\ mol^{-1}$
h, h	Specific enthalpy, $J\ mol^{-1}\ kg^{-1}$
H	Atomic hydrogen (Gas)
$[H]$	Concentration of atomic hydrogen, $mol\ m^{-3}$
H^+	Proton

H_2	Diatomic hydrogen (Gas)
$[H_2]$	Concentration of diatomic hydrogen, mol m^{-3}
ΔH_0	Enthalpy of formation, J mol^{-1}
$h\nu$	Reaction energy release
I_{sp}	Specific impulse, m s^{-1}
k	Boltzmann constant, J K^{-1}
k	Reaction rate coefficient, $\text{m}^3 \text{mol}^{-1} \text{s}^{-1}$
k_r	Reverse reaction rate coefficient, $\text{m}^6 \text{mol}^{-2} \text{s}^{-1}$
K	Equilibrium constant
k_{abs}	Reaction coefficient, s^{-1}
m	Mass of one hydrogen molecule, kg
M	Mach number
M	Third body molecule (aka. Bath Gas)
\dot{m}	Mass flow rate kg s^{-1}
\dot{m}	Mass flow rate into wall, kg s^{-1}
n	Occupied sites per surface area, sites m^{-2}
n_T	Total tungsten atoms per surface area, atoms m^{-2}
n_s	Total absorbed hydrogen atoms at saturation, atoms m^{-2}
$\frac{dn}{dt}$	Rate of molecular hydrogen accumulation per surface area, $\text{molecules m}^{-2} \text{s}^{-1}$
$\frac{dn}{dt}_{ads}$	Rate of molecular hydrogen adsorption per surface area, $\text{molecules m}^{-2} \text{s}^{-1}$
$\frac{dn}{dt}_{des}$	Rate of molecular hydrogen desorption per surface area, $\text{molecules m}^{-2} \text{s}^{-1}$

$\frac{dn}{dt}_{abs}$	Rate of molecular hydrogen absorption per surface area, molecules $m^{-2} s^{-1}$
P, P	Operating pressure, $N m^{-2}$
P_H	Partial pressure atomic hydrogen, $N m^{-2}$
P_{H_2}	Partial pressure molecular hydrogen, $N m^{-2}$
P_0	Stagnation operating pressure, $N m^{-2}$
q	Heat flux per surface heat, $W m^{-2}$
R	Universal gas constant, $8.314 J mol^{-1} K^{-1}$
$Rate_T$	Total rate reaction rate, $mol m^{-3} s^{-1}$
$Rate$	Reaction rate, $mol m^{-3} s^{-1}$
$Rate_r$	Reverse reaction rate $mol m^{-3} s^{-1}$
Re_D	Reynolds number, hydraulic diameter
Re_w	Wall Reynolds number
r_0	Radius of one NTP channel, m
s	Sticking coefficient
s_0	Initial sticking coefficient
ΔS_0	Entropy of formation, $J mol^{-1} K^{-1}$
T	Chamber temperature, K
T_0	Stagnation chamber temperature, K
T_0	Standard temperature, 298 K
T	Temperature, K, (Unitless with Exponent)
T_g	Gas temperature, or bulk temperature, K
T_s	Surface temperature, K

ΔT	Freestream and wall temperature difference, K
t	Time, s
U, u	Axial velocity, m s^{-1}
u_{max}	Maximum centerline velocity, m s^{-1}
U_{Mean}	Mean freestream and boundary layer velocity, m s^{-1}
U_{H_2}, U_e	Axial freestream velocity, m s^{-1}
v	Specific volume, $\text{m}^3 \text{kg}^{-1}$
v_w	Velocity into the wall, m s^{-1}
v_*	Friction velocity, m s^{-1}
X_H	Molar fraction of atomic hydrogen
$X_{H,0}$	Molar fraction of atomic hydrogen, stepped
X_{H_2}	Molar fraction of diatomic hydrogen
$X_{H,Eq}$	Atomic hydrogen molar fraction at chemical equilibrium
$\Delta X_{H,Eq}$	Difference from selected molar fraction of atomic hydrogen to equilibrium
$\Delta X_{H,Reaction}$	Change in molar fraction of atomic hydrogen from reaction
y^+	Normalized distance from wall (Unitless)
z, x	Axial distance, m
Δz	Discretized axial length, m
Δz_{sub}	Sub-grid discretized axial length of Δz , m

Greek

γ	Specific gas constant, $\text{J kg}^{-1} \text{K}^{-1}$
δ	Width of one tungsten atomic layer, m
θ	Coverage ratio
θ_{eq}	Coverage ratio at adsorption-desorption equilibrium
μ	Dynamic viscosity, $\text{kg m}^{-1} \text{s}^{-1}$
ν	Frequency factor, $\text{m}^2 \text{s}^{-1}$
ν	Kinematic viscosity, $\text{m}^2 \text{s}^{-1}$
ρ	Hydrogen density, kg m^{-3}
τ_w	Wall shear stress, N m^{-2}
ϕ	Flux of the incident hydrogen molecules, $\text{molecules m}^{-2} \text{s}^{-1}$

Chapter 1 Overview, Literature Review, and Primer on NTP

1.1. Overview

The treatment of hydrogen dissociation in nuclear thermal propulsion (NTP) systems is either over-simplified or neglected in performance analyses as well as in computational fluid dynamics (CFD) models. NTP systems operate at high temperatures and under high-speed flows with a goal to operate for tens of hours at a time [1]. Precise knowledge of dissociation in NTP systems is necessary to track even small amounts of atomic hydrogen that may lead to degraded performance, incorrect designs, and corrosive effects.

This study seeks to validate atomic hydrogen levels by investigating the chemical kinetics of an array of historic NTP engines. The approach uses data provided at the inlet and outlet conditions while varying several internal parameters to best understand behaviors across multiple NTP cases.

Prior to modeling, CFD must have *a priori* knowledge if a system operates at chemical equilibrium. CFD operating at non-equilibrium must consider significant non-linearity of partial differential equations extending computation time and complicating convergence. The results of this study will support future CFD work by validating the dissociation assumption and determine if the chemical reaction operates at equilibrium.

Hydrogen dissociation is rarely considered in the high-temperature flow of nuclear thermal propulsion (NTP) engine performance. The dissociation of surface reactions is likewise ignored in design and optimization. Dissociation in the flow can remove energy from the fluid while it is heated; atomic hydrogen can later recombine, adding energy at unknown locations in the engine and altering performance.

1.2. A Primer on Nuclear Thermal Propulsion (NTP)

The goal of NTP systems is to maximize fuel efficiency, also referred to as specific impulse. This is done by using the lowest molecular weight exhaust gas, namely hydrogen, heated to the highest possible exhaust temperatures and expanded in a nozzle to supersonic speeds [2]. These high temperatures can break the hydrogen gas covalent bond in an endothermic reaction removing energy from the flow, changing the molecular weight of the gas mixture, and shifting the thermodynamic properties including thermal conductivity [3, 4]. However, NTP systems of the 1960s and 1970s often, admittedly, neglected hydrogen dissociation [5].

From 1991 to 2007, the American Institute of Physics hosted the Space Nuclear Power and Propulsion Symposium. Very few research articles noted hydrogen dissociation and virtually all assumed hydrogen dissociation at chemical equilibrium. The symposium provided updates to NTP research of the 1960s and 1970s and, arguably, was the premier source for NTP research of the time. These 16 volumes contained over 20,000 pages of nuclear power research with more than 3,000 pages devoted exclusively to NTP. An exhaustive review of this library returned four articles studying hydrogen dissociation. One article stressed the accurate measurement of gas and surface temperatures to understand dissociation, but only cites equilibrium values at varying temperatures [6]. Low-pressure, pellet-bed reactor NTP designs acknowledged a critical issue in omission of dissociation modeling proposing as much as a 13.8% increase in required power to overcome hydrogen dissociation effects with minimal analysis [7]. Other low-pressure research abandoned finite-rate dissociation analysis assuming equilibrium throughout a reactor core and rocket nozzle as a valid *a priori* assumption [8]. Finally, one publication attempted to solve dissociation in NTP systems but only examined a low-pressure chamber and nozzle omitting any reactor analysis [9].

Recently, a variety of NTP research has focused on fully solving neutronics, hydraulics, and material properties continuing to assume global dissociation equilibrium. Thermodynamic properties are refined in one research article focused on NTP dissociation, also noting a significant enhancement in heat transfer due to dissociation, however chemical equilibrium is chosen over finite-rate calculations for simplicity [10]. New reactor designs look to low-enriched uranium (LEU) through new moderation configurations. The fuel elements of these designs operate at similar temperature profiles to this study [11]. As will be elaborated below, the pressure-dependence of this study allows analysis at increased fuel element pressures that are relevant to low-enriched uranium designs.

To create future accurate models, correct designs, and precise calculations for specific impulse, a better understanding of the non-equilibrium chemically reacting hydrogen flow in NTP systems is required. Historic NTP engines provide an excellent vantage point to provide perspective on this effect and observe its behavior under high-speed, high-temperature fluid dynamics.

Historic NTP reactors were made up of hexagons containing constant area pipes that are very smooth and heated via radiation and thermal heat transfer. The KIWI-4BE, used as a baseline example throughout this study, is a cylindrical reactor with thousands of “coolant” channels running through hexagonal uranium fuel elements with fuel loadings and groupings to pass heat to the hydrogen passing through the coolant channels. Table 1 shows the operating conditions of the KIWI-4BE, and Fig. 1 shows the components and fuel elements.

Table 1. KIWI-4BE operating conditions [12]

Mass Flow Rate (kg/s)	31.8
Fuel Exit Average Temperature (K)	2,330
Chamber Temperature (K)	1,980
Chamber Pressure (MPa)	3.49
Core Inlet Temperature (K)	104
Core Inlet Pressure (MPa)	4.02
Periphery and Structural Mass Flow Rate (kg/s)	2.0

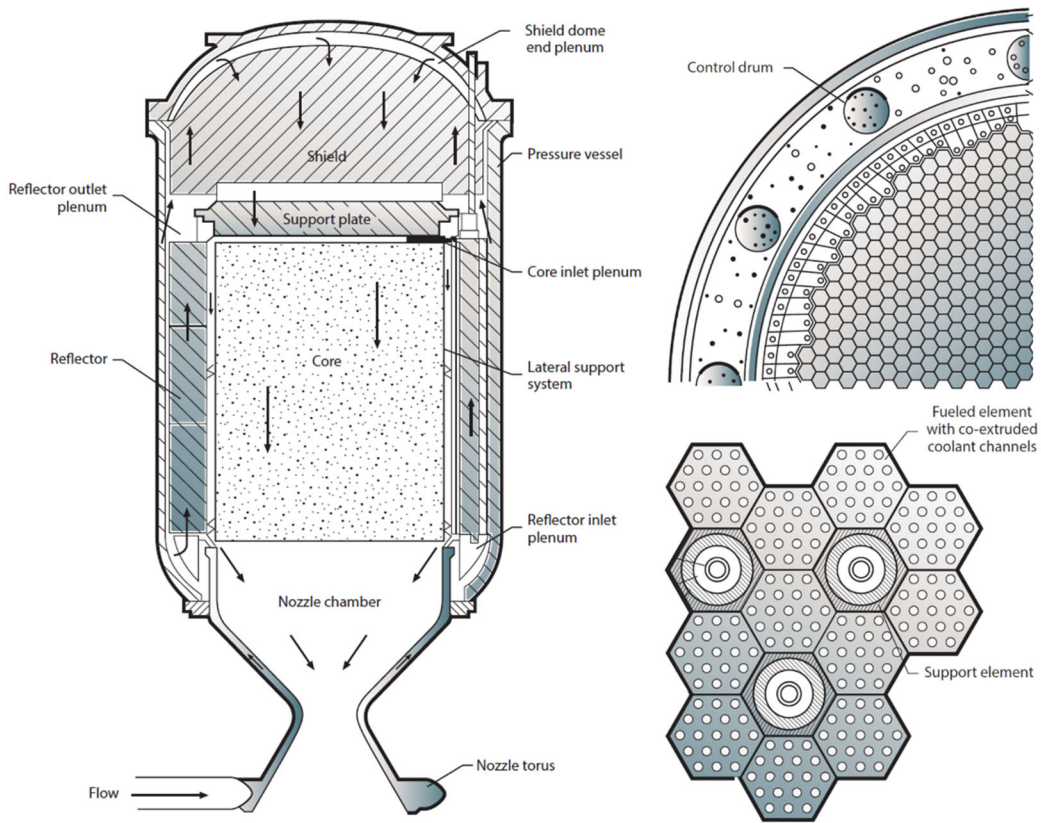


Fig. 1. KIWI-4BE overview design and fuel element schematics [13]

NTP engines are designed around maximized mass flow rates and heat transfer from reactor walls to hydrogen propellant flow. The goal is to maximize the specific impulse which is a measure

of fuel efficiency similar to efforts in hypersonics [14]. Engines use nuclear fuel and a moderator to heat a hydrogen flow to above 2500 K as in Fig. 2. Thousands of circular ducts permit hydrogen to enter at low temperatures where it is heated. Reynolds numbers are usually above 10^5 indicate fully turbulent pipe flow from reactor entry to reactor exit. After heated it passes through an expansion and divergent section, accelerating to supersonic speeds. Fig. 3 shows the typical velocity and thermal profile for circular duct flow.

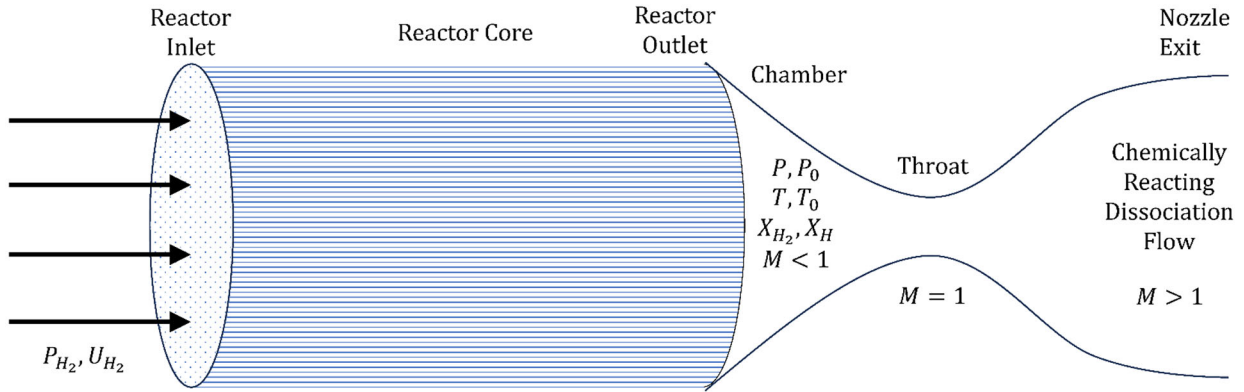


Fig. 2. Schematic of NTP reactor

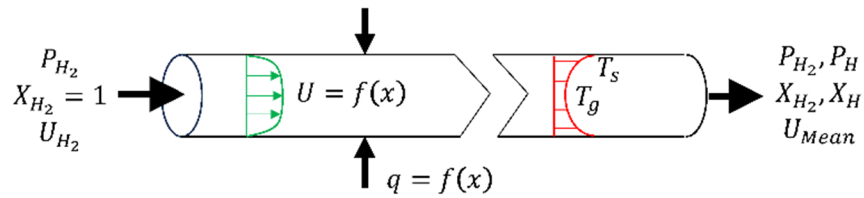


Fig. 3. Velocity and thermal boundary layer within a pipe flow

1.3. Surface Reactions included with Bulk Flow Reactions

This study revisits historic and modern NTP engines also to investigate fluid mechanics changes due to hydrogen dissociating surface reactions in the reactor cladding materials. The focus is the boundary layer effects within a single channel to describe all channels. Adsorption, desorption, and absorption of hydrogen into the pipe wall cladding results in a perpendicular mass transfer and velocity into the wall, altering the fluid boundary layer and heat transfer as in Fig. 4.

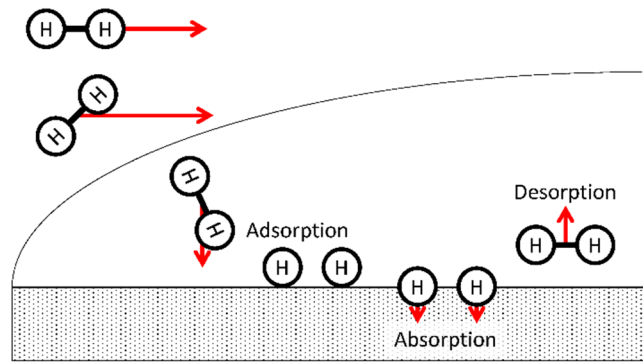


Fig. 4. Hydrogen adsorption, desorption, and absorption phenomena

The historic KIWI B4E engine is again used for calculations requiring geometric design and alter to mimic modern low-enriched uranium (LEU) reactors for any comparisons.

Hydrogen surface reactions occur through the concepts of adsorption, desorption, and absorption. Adsorption is the effect where hydrogen molecules attract to and stick to the cladding surface. An incident molecule adheres to the surface with some probability, known as the sticking coefficient, s . Adsorption is usually a function of the sticking coefficient and the mass flux of the incoming hydrogen molecules. Desorption is the opposite process, where hydrogen is released

from the surface due to the energized sticking surface. The energy transferred to the particle permits it to escape the attractive forces and eject from the surface. Particles with enough energy upon adsorption may *absorb* into the surface. Absorption is the surface process where energetic particles overcome an energy barrier and penetrate a cladding material.

In 1912, Dr. Irving Langmuir won the Nobel Prize for his findings in studying hydrogen surface dissociation on tungsten. Many would make slight modifications to his experiment to refine the conclusions [15]. Desorption would prove to contain both an activation barrier, E_d , and frequency factor, ν , and be validated as a second-order kinetic reaction mechanism [16].

Alnot et al. experimentally confirmed the initial sticking coefficient of tungsten under a variety of gas and surface conditions [17]. Smith et al. formulated the rate equation of the desorption of hydrogen from tungsten considering observed surface reorientation phenomenon [18]. Other experiments including molecular dynamics (MD) simulations, would map out a variety of potential adsorption and desorption activation energies for various surface plane alignments and situations [19].

Dr. Frauenfelder would find that upon adsorption of hydrogen, the atoms would penetrate and permeate into nuclear reactor cladding materials [20]. Modern-day reactor studies including tokamak design continue to use his high-temperature data as the most valid source for both high and low-temperature hydrogen diffusion calculations [21]. The most recent work shows that the largest energy barrier to overcome is the actual penetration of the surface of the cladding material and not the diffusion once inside the reactor cladding [22].

Studies in wall suction also emulate the mass flux found in NTP. The most current forms of suction to stabilize the turbulent boundary layer in pipe flow reaching a constant boundary layer along the length of an object. This flow control resembles this phenomenon of absorption but at

higher crossflow velocities [23]. Avsarkisov et al. show for significant crossflow velocities of suction the mean velocity profile changes shrinking the turbulent boundary layer [24]. Heat transfer is not greatly impacted by low levels of wall suction as described below.

NTP cladding material has shifted designs over the generations. Zirconium carbide (ZrC) was used in legacy NTP engines. Carbides were abandoned due to the production of methane in the propellant stream [25]. Modern engines use a molybdenum-tungsten (Mo-W) alloy where tungsten is 30% of the alloy under very similar temperature profiles and gradients with some designs operating at pressures 3 MPa greater than the KIWI B4E engine of historic NTP engines [26].

The alloying of tungsten with molybdenum helps decrease weight but produces an interfere cladding to pure tungsten. Molybdenum is a good heat conductor while remaining low in a neutron thermal absorption cross-section compared to tungsten [27]. Both molybdenum and tungsten share a similar number of trapped hydrogen atoms when exposed at the roughly the same temperature [28]. Molybdenum contains a permeability which is three thousand times greater than that of tungsten at increased operating pressures [29]. Alloying molybdenum with tungsten creates grain boundaries where hydrogen diffusion is increased by up to 5 times [30]. This study selects single-crystalline tungsten as the study cladding material and is used throughout due to its superiority to molybdenum-tungsten alloy but further considerations will be made for the molybdenum-tungsten alloy as the cladding material [31]. Wall absorption will come into question in this document and comparison to zirconium carbide cladding will be analyzed.

Ultra-safe nuclear plans to use a zirconium carbide (ZrC) cladding with their fuel configuration [32]. Research is relatively sparse on hydrogen adsorption and desorption rates on the zirconium surface [33]. Density functional theory (DFT) provides some insight into individual

atom surface interactions, but virtually no research is found at the fluence levels expected in NTP, and only mass loss rates are considered as opposed to surface reaction rates [34, 35]. ZrC does contain some useful data on penetrative diffusion which is compared later in the analysis [36].

However, at NTP temperatures, carbon from within zirconium is known to experience vaporization from the cladding leaving vacancies inviting additional hydrogen diffusion into the cladding [37]. This will expel the heavy molecules of methane and acetylene into what should be a minimized molecular mass ratio. These vacancies are expected to be only temporary in nature while a protective barrier of zirconium hydride (ZrH) is created in the cladding and establishes a barrier from further penetrative diffusion [38]. The interplay of continually vaporizing carbon and diffusion of hydrogen into these voids requires further research but is not covered in this analysis.

Surface reactions within the cladding are supported by a vast array of literature focused on hydrogen desorption, adsorption, and absorption in tungsten. However, very little information is available on the surface-normal diffusion, also known as penetration, for molybdenum-tungsten.

With the yet unknown states of zirconium carbide as well as molybdenum-tungsten, tungsten is selected as a behavior analysis of the highest technology-ready level cladding for use in nuclear thermal propulsion reactors. This study attempts to understand the trend information when chemically reacting flow and surface flow interactions are returned to the model.

1.4. Reactor Outlet Study for Rocket Chamber Conditions

Rocket propulsion contains several design considerations and assumptions permitting correct design and optimization. The assumptions include a flow assumed to be zero, or negligible, in the combustion chamber [39], maximum temperature, and a known species condition. Overall, rocket propulsion depends on accurate and compliant chamber conditions.

Nuclear thermal propulsion (NTP) expands the working propellant in a nozzle similar to liquid and solid propulsion systems. This similar use requires an accurate knowledge of the entry conditions, or NTP “chamber,” though combustion does not explicitly occur in NTP systems.

NTP relies on the highest chamber temperatures and lowest molecular weight of the propellant to achieve maximum fuel efficiency. William Emrich describes the fuel efficiency of the engine in Equation (1) [40].

$$I_{sp} = \sqrt{\frac{2\gamma}{\gamma - 1} \frac{R}{M} T_c} \quad (1)$$

From Equation (1), the dominant terms are assumed to be the chamber temperature T_c and the molecular mass of the propellant, M . Based on this assumption, the highest chamber temperature and the lowest molecular mass propellant produces the best fuel efficiency. These two items can help determine if including chemically reacting flow changes the engine performance.

This study accomplishes a 2-D analysis of chemically reacting flow considering the dissociation of hydrogen in bulk and surface reactions of NTP systems, assuming a KIWI 4BE geometry. Where available, equilibrium chemical reactions are the only thing under consideration and all analysis is done as a 1-D axial analysis [41].

Modeling nuclear thermal propulsion as a rocket propulsion process requires matching of flow properties at specific locations. The analysis finds flow properties as they exit individual circular heating ducts. These channels culminate in a chamber prior to de Laval nozzle expansion. Fig. 5 shows that culmination of NTP channels in chamber with supersonic expander.

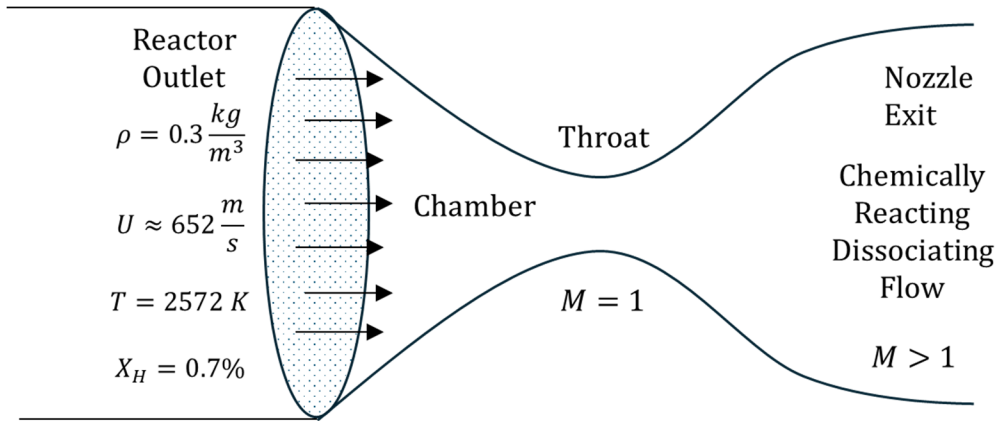


Fig. 5. Culmination of NTP channels in chamber with supersonic expander

Calculation of the changing atomic hydrogen level requires a chemical analysis throughout nozzle expansion. NASA Chemical Equilibrium Analysis Application provides the tools to complete this analysis. The specific impulse is found for the chemically reacting flow and non-chemically reacting flow cases and compared.

Research into high Mach number flows encountered bodies undergoing chemical reactions [42]. To account for these effects, high-temperature flows had to incorporate a chemical reaction of flows along bodies. Specifically, properties would change between calorically perfect gases and chemically reacting gases. Combining the previously mentioned concepts of non-equilibrium, identifying the current, and accurate, values for gas properties became a challenge for closed form solutions.

In a de Laval nozzle, these challenges were mitigated by exploring both frozen flows and equilibrium flows. For calorically perfect gases, the static-to-stagnation ratios as well as throat-to-exit ratio could be calculated based solely off Mach number. A frozen flow assumes zero chemical

reactions and uses the Mach number for these calculations. However, for an equilibrium flow, the properties become a function of temperature.

Numerical calculations of non-equilibrium reactions in de Laval nozzle flow fall between frozen and equilibrium flow. This provides a good check where frozen flow provides the lower bound of 1-D temperature profile through the nozzle while equilibrium flow provides the upper bound. Non-equilibrium solutions should fall between these values. Adaptive grids were found necessary through the nozzle to establish stability of the solution. Numerical calculations showed that significant non-equilibrium is present [43].

Chapter 2 Equilibrium Validation of Dissociation in NTP

2.1. The Elementary Chemical Reaction Mechanism of Hydrogen Dissociation

The chemical reaction mechanism in this study is shown to be a simple unimolecular, pressure-dependent equation for molecular hydrogen dissociation, also known as a decomposition reaction. To illustrate this simplification, consider the reduction of a validated chemical reaction mechanism for hydrogen plasma. Hydrogen plasma begins with diatomic hydrogen gas that dissociates and then splits into fundamental protons and electrons. Increasing temperatures are required to provide energy for this reaction. A validated chemical reaction mechanism for generating hydrogen plasma is shown in Table 2.

Table 2. Plasma Arrhenius equations and expression [44]

	Reaction	A (cm ⁶ mol ⁻² s ⁻¹)	n (unitless)	E (kJ mol ⁻¹)
1	$2\text{H} + \text{M} \rightleftharpoons \text{H}_2 + \text{M}$	$6.40 \cdot 10^{17}$	1.0	0
2	$\text{H}^+ + \text{e}^- + \text{M} \rightleftharpoons \text{H} + \text{M}$	$5.26 \cdot 10^{26}$	2.5	0
3	$\text{H}_2 + \text{e}^- \rightarrow 2\text{H} + \text{e}^-$	$1.91 \cdot 10^{11}$	-1.0	-203
4	$\text{H}^+ + \text{e}^- \rightarrow \text{H} + \text{h}\nu$	$3.77 \cdot 10^{13}$	0.58	0

The “M” noted in the equation represents the species, or molecule, of the surrounding medium, also known as a third body, that provides the pressure on the reaction. The double arrows indicate a reversible reaction; this example uses the reverse of reactions 1 and 2 for illustration. The reverse of reaction 1 is the dissociation step followed by the reverse of reaction 2 that initiates

the generation of hydrogen plasma via reactions 3 and 4. Additional ionizing intermediate steps are available for this mechanism beyond reaction 4 but will prove unnecessary to this example. Equation (2) is the rate coefficient for the data in Table 2 where A is the pre-exponential factor, n is the rate exponent, E is the activation energy, R is the universal gas constant, and T is the absolute temperature in Kelvin.

$$k = AT^{-n}e^{E/RT} \quad (2)$$

The reverse of reaction 2 is calculated using the equilibrium constant (K) in Equation (3) to solve for the backward rate coefficient (k_r). The Gibbs free energy of formation (ΔG_0) of reaction 2 is found from a standard chemical reference source [45].

$$K = \frac{k}{k_r} = e^{\frac{-\Delta G_0}{RT}} \quad (3)$$

Upon variations analysis, the backward rate coefficient is insignificant at historic and current NTP reactor conditions and supports a unimolecular, single-step mechanism which is the reverse of reaction 1. Calculations were made across a range of atomic hydrogen concentrations, from 1 MPa to 100 MPa third-body pressure, and from a temperature of 200 K to 3000 K. NTP systems usually operate below 3000 K and between 2 and 14 MPa. Proton and electron production was extremely small. Therefore, at NTP conditions, this first step of ionization does not occur and therefore does not initiate the following steps of plasma generation. Historic and current NTP solid fuel designs can be assumed to be below the threshold for plasma generation; only the unimolecular dissociation reaction shown in reaction 1 (reverse) occurs. Disassociation of molecular hydrogen is known to have no other intermediate states and proceeds directly from products to reactants [46]. This illustration validates that a reduced, single unimolecular, pressure dependent finite rate

equation adequately models the production of atomic hydrogen in NTP systems. However, better models of reaction 1 are available and described below.

2.2. Literature Review for the Correct Chemical Reaction Mechanism

Review of the literature requires a careful selection of the finite-rate dissociation equation to replace reaction 1 that is applicable to NTP systems. Fig. 6 displays reaction rate coefficients for five candidates. The backward reaction, as described later, is illustrated for a quick comparison.

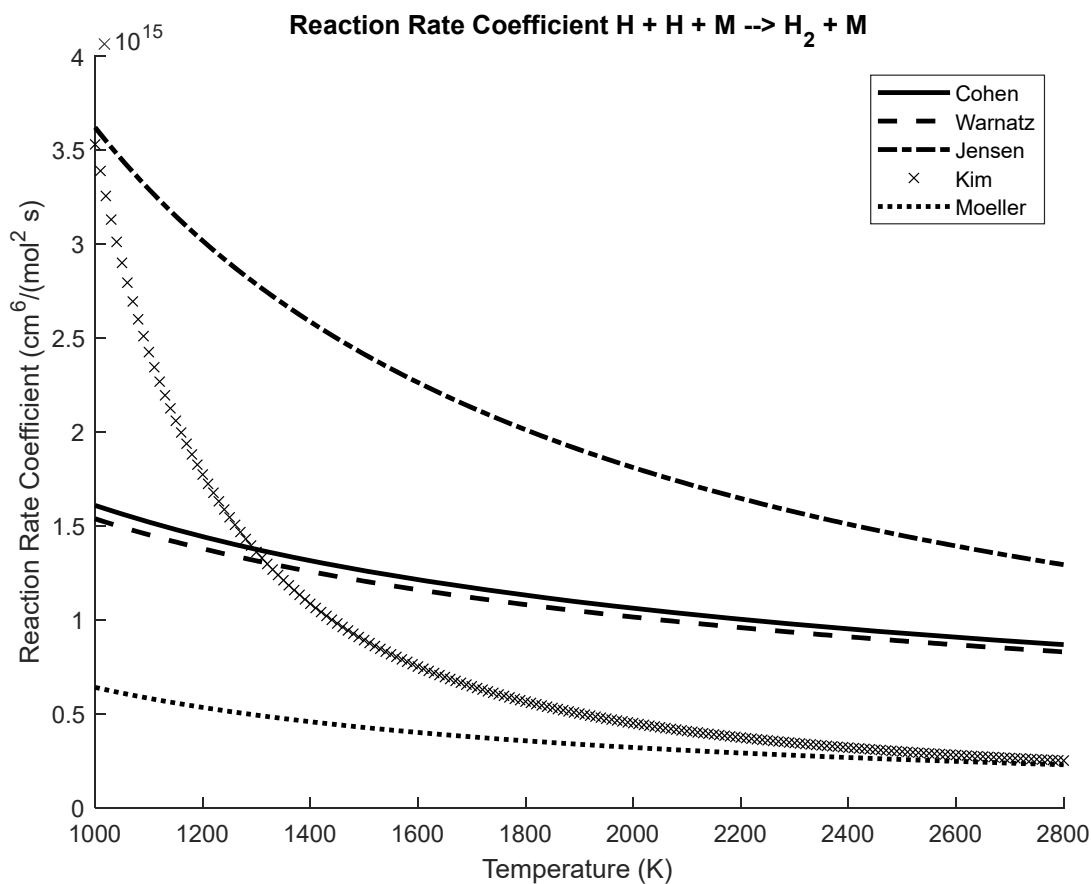


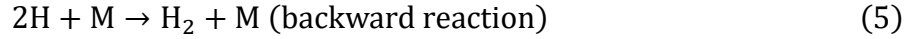
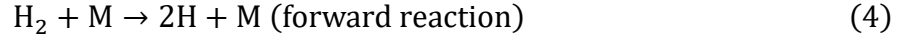
Fig. 6. Reaction rate coefficient comparison for model selection

One publication analyzed finite-rate coefficients from two sources: a literature survey accomplished by Baulch et al. in and a rocket exhaust flow field from Jensen [47]. While, Baulch identified Moeller as the recommended source, this is stated as applicable for hydrogen between 2500-5000 K [48]. Since this is largely beyond the operating range of most NTP systems, Moeller is not selected for the model. One symposium publication from 1994 studied a low-pressure nuclear thermal rocket operating around 3000 K [49]. Without clear reference, the publication uses the rate coefficient labeled Kim in Fig. 6. This closely correlates with the Moeller rate coefficient for high temperature models. Likewise, Kim is not selected.

An updated literature review from 2005 recommends a 1983 finite-rate mechanism by Cohen et al. [50]. This model uses low temperature data, reverse rate data converted using the equilibrium constant, as well as multiple sources of high temperature data from shock tube experiments [51]. Warnatz made a similar recommendation that closely matches Cohen within the applicable temperature region of interest [52]. While an outlier, Jensen also matched within a factor of 2.4. While shock tube experiments are done at lower pressures, these rates are often used at higher pressures such as in combustion. Cohen's rate coefficient provides a credible finite-rate coefficient for historic NTP reactors coefficient in the gap between low and high temperature targeting the operating temperatures and high pressures. Additionally, Cohen formulated the rate coefficient using a pure bath gas (third body) of molecular hydrogen gas, H₂ which is important for including relevant rate data. Cohen is selected as a credible rate coefficient and shown in below equations.

The elementary hydrogen dissociation reaction is modeled using logarithmic empirical curve-fits of data experiments as originally introduced by Arrhenius. Chemical reactions occur in a manner at which probability and temperature are always producing forward and backward

reactions. The hydrogen dissociation, named the forward reaction, and the combination, named the backward reaction, are displayed in Equations (4) and (5).



Equations (6) and (7) show the individual rates from Cohen of the forward and backward reactions which are first- and second-order kinetic reactions, respectively [53].

$$\text{Rate} = k \cdot [\text{H}_2][\text{M}] \text{ where } \text{M} = \text{H}_2 \text{ (forward reaction)} \quad (6)$$

$$\text{and } k = 8.612 \times 10^{11} \text{ T}^{-0.7} e^{-52530/\text{T}}$$

$$\text{Rate}_r = k_r \cdot [\text{H}]^2[\text{M}] \text{ where } \text{M} = \text{H}_2 \text{ (backward reaction)} \quad (7)$$

$$\text{and } k_r = 1.015 \times 10^5 \text{ T}^{-0.6}$$

This model is validated by the equilibrium constant derived from thermodynamic values and Gibbs Free Energy. Equation (8) solves for the Gibbs free energy of formation. Enthalpy of formation (ΔH_0) and entropy (ΔS_0) can be calculated from products and reactants of Equation (4) using a thermodynamic source for entry into Equation (8) [54].

$$\Delta G_0 = \Delta H_0 - T_0 \Delta S_0 \quad (8)$$

Equations (6) and (7) can be validated by observing two formulations of the equilibrium constant. Equations (6) and (7) are converted to moles per cm^3 and input into the central expression of Equation (3) above. This expression is the finite-rate equilibrium if the reaction rates are allowed to continue for a period. Equation (8) can be input into the right-hand expression of Equation (3) above for comparison to the central expression. Fig. 7 validates the model by depicting a good

correlation between the finite-rate equilibrium and thermodynamic, or Gibbs, equilibrium at historic NTP values. Below 2000 K, the values for comparison are virtually identical.

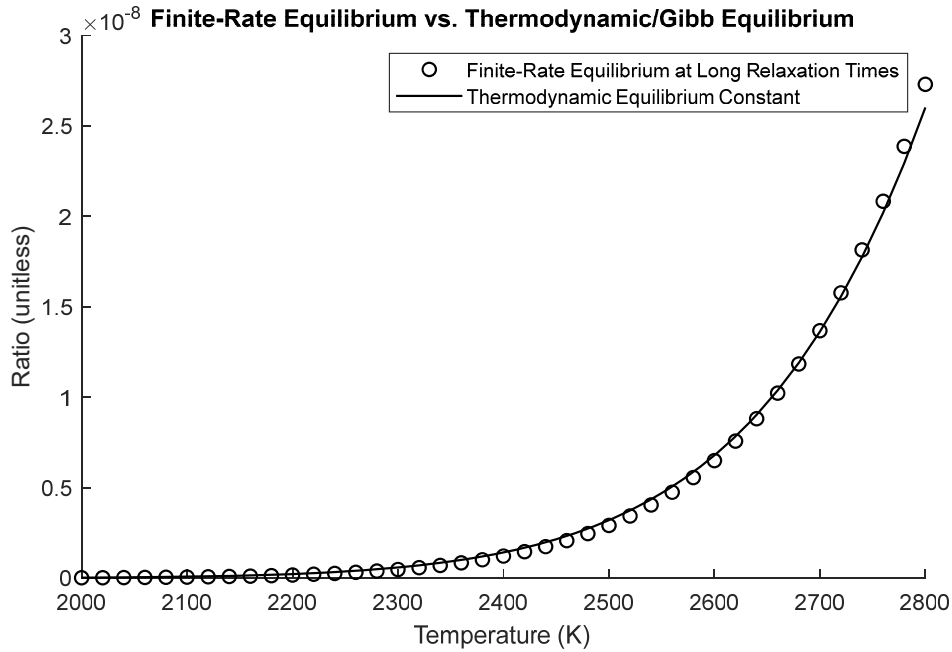


Fig. 7. Finite-rate equilibrium at relaxation times compared to thermodynamic/Gibbs equilibrium

The total rate of the reaction is found by subtracting the backward reaction from the forward reaction and arriving at the total reaction rate, which is the production of atomic hydrogen shown in Equations (9) and (10).

$$\text{Rate}_T = \frac{d[\text{H}]}{dt} = \text{Rate} - \text{Rate}_r = k \cdot [\text{H}_2]^2 - k_r \cdot [\text{H}]^2[\text{H}_2] \quad (9)$$

$$\text{where } [\text{H}_2] = X_{\text{H}_2} C_T, \quad [\text{H}] = X_{\text{H}} C_T, \quad X_{\text{H}} + X_{\text{H}_2} = 1$$

$$\text{Rate}_T = k[(1 - X_H) C_T]^2 - k_r X_H^2 (1 - X_H) C_T^3 \text{ where } C_T = \frac{P}{RT} \quad (10)$$

Of note, all temperatures produce forward and backward chemical reactions altering their concentration until reaching a limit of equilibrium. Given an initial concentration and temperature, a chemical reaction will begin that either increases, or decreases, the atomic hydrogen. Upon reaching a specific concentration, the derivative becomes zero and the chemical reaction rates for forward and backward are equal. This is referred to as the point of equilibrium.

Equilibrium flow in a CFD control volume can be assumed if the chemical reactions reach equilibrium much faster than the time it takes for the flow to transit the control volume. The approach of this study is to observe the reactions occurring within a constant-size control volume throughout the reactor, shown in Fig. 8, to identify equilibrium. If the reactions do not reach equilibrium prior to the flow exiting the control volume, then equilibrium is not possible [55].

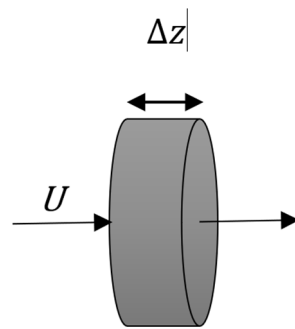


Fig. 8. Depiction of control volume

2.3. Assumed Conditions in the NTP Reactor

The mass flow rate through the NTP coolant channels leads to turbulent flow. Equation (11) shows the Reynolds number for pipe flow.

$$Re_D = \frac{\rho U D}{\mu} \quad (11)$$

Above a Re_D of 2000, pipe flow will be turbulent. Assuming the KIWI-4BE parameters at inlet conditions, the Reynolds number is on the order of 92,000 or 10^5 , which indicates fully turbulent pipe flow [56, 57]. Consequently, turbulent pipe flow of smooth pipes establishes a flat, and predominantly, uniform velocity profile near the average velocity for pipe flow [58]. Assuming thin boundary layers, this establishes a virtually universal flow speed that is the average flow velocity. Therefore, this supports an assumption that the flow speed is everywhere the average flow velocity for this early analysis.

Dividing the mass flow rate among the thousands of individual channels shows a subsonic inlet condition for all coolant channels. The KIWI-4BE contains 1,542 Fuel Elements with 19 coolant channels per fuel element. Some elements contain less channels to create the circular reactor. The total number of coolant channels is 29,172. The total mass flow rate of 31.8 kg/s must be divided among these coolant channels equaling 0.96 gm/s of hydrogen per channel [59]. The diameter of each coolant channel is 0.254 cm. Considering the viscosity and density of the hydrogen at a temperature of 104 K, Equation (12) shows the solution for the inlet velocity as 19.86 m/s [60].

$$\dot{m} = \rho U A \quad U = \frac{\dot{m}}{\rho A} = \frac{4\dot{m}}{\pi \rho D^2} \quad (12)$$

The speed of sound is the ratio of the resulting change in pressure divided by the change in density in a compressible flow along a constant line of entropy. Processes that are non-isentropic produce a distinct form of the speed of sound equation through a variety of assumptions in the elementary laws of thermodynamics. The speed of sound, at equilibrium chemical reactions, is shown in Equation (13) [61].

$$a^2 = \left(\frac{\partial P}{\partial \rho} \right)_s \quad a_e^2 = \gamma RT \frac{[1 + (1/p)(\delta e / \delta v)_T]}{[1 - \rho(\delta h / \delta p)_T]} \quad (13)$$

Data tables are available to solve Equation (13) for the complex quantum calculations of statistical thermodynamics [62]. At high temperatures, the vibrational and rotational energy levels excite requiring separate forms of basic thermodynamic equations. Statistical thermodynamics charts accurately display thermodynamic properties, for a specific pressure, for hydrogen capturing the quantum effects including the speed of sound. Further, the table can be used to curve-fit the speed of sound. Table 3 shows the range of data used to curve-fit the speed of sound. All above assumptions solve to an inlet Mach number of 0.02; the speed of sound at 104 K is approximately 1190 m/s.

Table 3. Statistical thermodynamic speed of sound of equilibrium hydrogen [63]

(Pressure = 40 atm)

Temperature (K)	a_e / a_0
300	1.048
600	1.482
1000	1.906
1200	2.080
1400	2.237
1600	2.381
1800	2.516
2000	2.641
2200	2.757
2400	2.862
$a_0 = 1.2559 \text{ km/s}$	

With only heating, Rayleigh flow shows that the maximum speed in the pipe is the sonic speed of the hydrogen gas. Heated pipe flow is a non-isentropic process that, if originally subsonic, will increase flow velocity up to the speed of sound and no farther. The flow speed will never exceed the speed of sound.

The neutron fluence of NTP reactors usually follows a cosine thermal energy flux generating a near-sinusoidal temperature profile [64]. However, the temperature profiles can vary slightly in shape among historic and current NTP reactors. Low-enriched uranium fuel element designs also operate at similar temperature profiles to this study with comparable hydrogen flow speeds [65]. Therefore, a variety of profiles are modeled including linear, square, and quarter-root along with sinusoidal with all curves fit to the inlet and outlet NTP reactor temperatures. Fig. 9 displays the considered profiles.

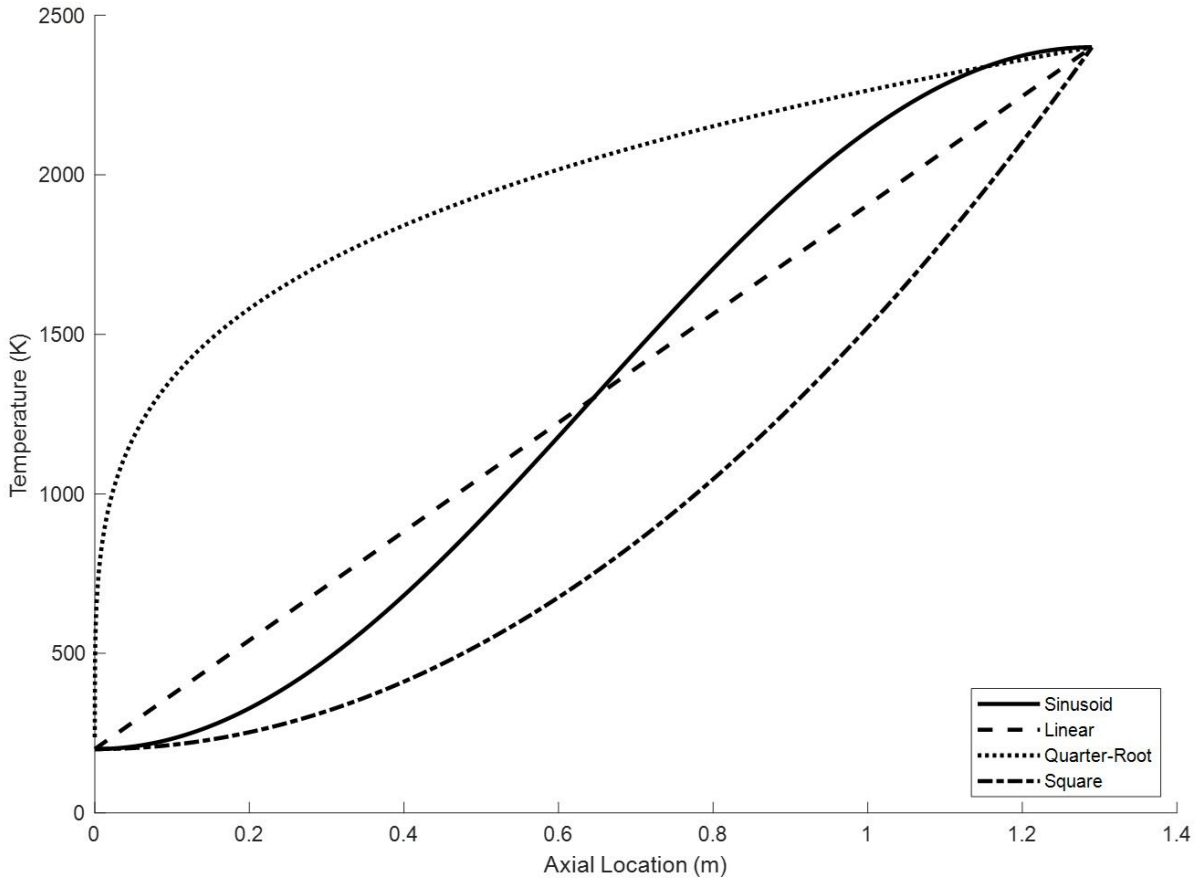


Fig. 9. Considered NTP reactor temperature profiles

NTP reactors contain operating pressure losses, but the pressure is assumed to negligibly change due to the lack of large pressure change phenomenon. At subsonic speeds, no shockwaves exist in the flow changing the pressure. Heating will cause the flow to accelerate, but it will not go beyond sonic conditions. The phenomenon of flow pressure changes center around wall losses from boundary layers, friction, or choked flow in the form of shockwaves. As mentioned earlier, boundary layers are neglected in this analysis and flow is assumed average over the cross-section.

Further, the NTP reactor channel walls are known to be smooth. This study adopts a constant universal pressure assumed from the outlet. The pressure losses are revisited later in the analysis.

2.4. Non-Equilibrium Considerations of NTP Reactors

At reactor NTP inlets, small amounts of atomic hydrogen, up to 1% molar fraction, are consumed at extremely high reaction rates. The Arrhenius equation demonstrates two specific regions: a predominant region of negative reaction rates that combine atomic hydrogen and a very small region of positive reaction rates that dissociate to make atomic hydrogen. Between these regions, a line of equilibrium represents near-zero reaction rates. Fig. 10 displays the solid-black equilibrium line along with the gradients of negative (top-left) and positive (bottom-right) reaction rates.

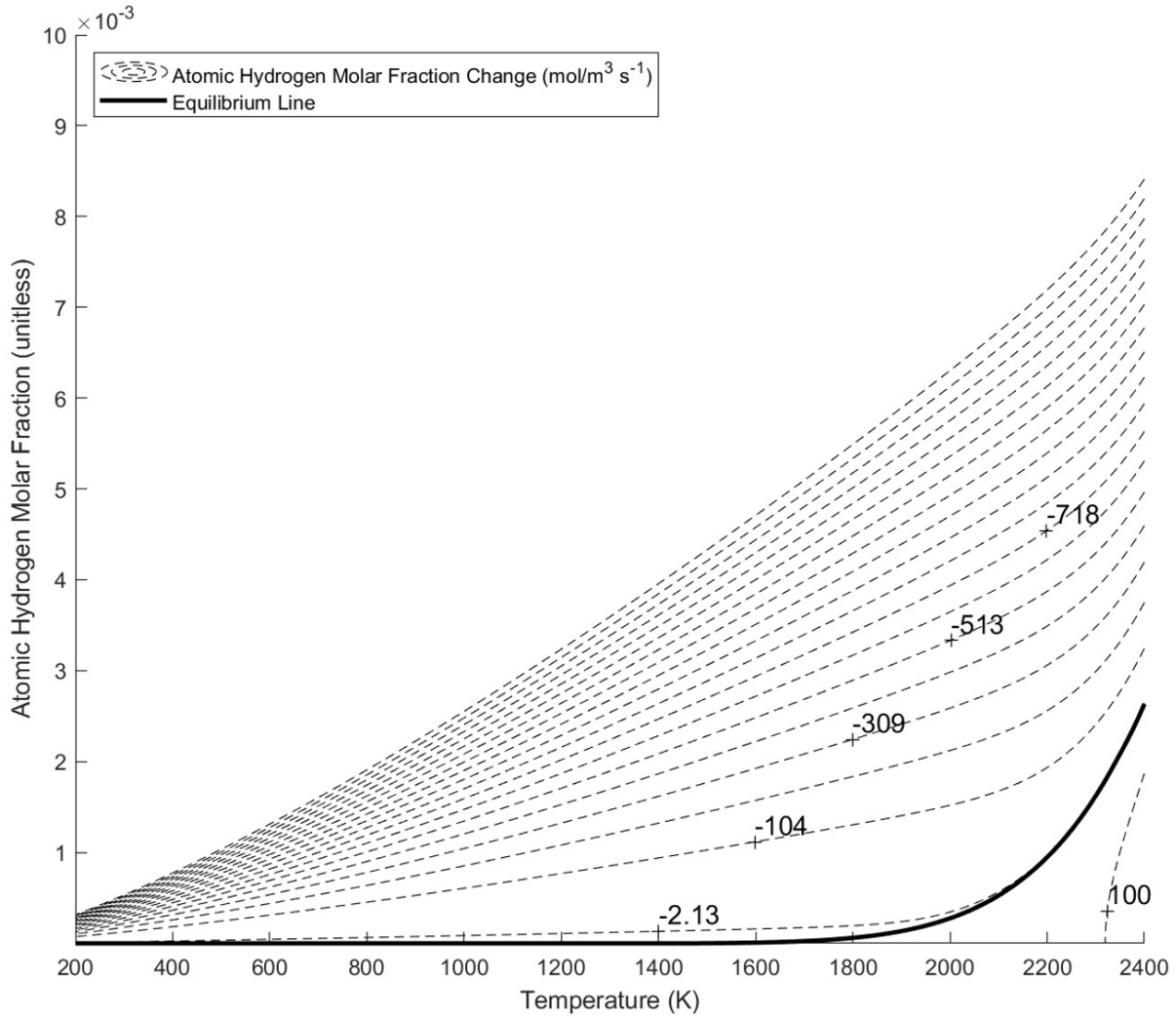


Fig. 10. Dissociation reaction rates at various molar atomic hydrogen and temperature levels

Numerically integrating the reaction rate equation shows that trace amounts of atomic hydrogen all rapidly reach equilibrium within the control volume and can be assumed to be at equilibrium. Equation (14) shows the definite integral that is numerically integrated to determine the time to equilibrium. The assumption is that the engine is operating without a change of concentration with respect to time. Additionally, the change in total concentration is assumed to

be negligible across the control volume due to the negligible temperature change across the control volume while pressure is globally assumed constant.

$$\begin{aligned} \frac{dX_H}{dt} &= k(1 - X_H)^2 C_T - k_r X_H^2 (1 - X_H) C_T^2 + \frac{(1 - X_H) d C_T}{C_T dt} \\ \frac{1}{C_T} \frac{dX_H}{dt} &= k \left[1 - 2X_H + \left(1 - \frac{k_r}{k} C_T \right) X_H^2 + \frac{k_r}{k} C_T X_H^3 \right] \\ \int_0^t dt &= \frac{1}{C_T k} \int_{X_H}^{X_{H,eq}} \left[\frac{1}{1 - 2X_H + \left(1 - \frac{k_r}{k} C_T \right) X_H^2 + \frac{k_r}{k} C_T X_H^3} \right] dX_H \end{aligned} \quad (14)$$

To understand if the flow can be considered in equilibrium, the time to equilibrium must be compared to the time the flow remains in the control volume. Equation (15) is a ratio of the equilibrium time, t , to control volume resident time expressed as $\Delta z/a_e$.

$$CV_{\%} = \frac{t}{\Delta z/a_e} \quad (15)$$

Atomic hydrogen values of 0.1%, 0.5%, and 1% molar fraction produced equilibrium in the first 1%, 0.3%, and 0.2%, respectively, of the control volume assuming flow at sonic speeds. All inlet atomic hydrogen levels react so quickly that equilibrium is reached within the control volume and can be assumed to be at equilibrium.

Beyond inlet conditions, behaviors of non-equilibrium are evident using approximations. Assuming a sinusoidal temperature profile and sonic flow, the change in molar atomic hydrogen along the reactor axis can be expressed by Equation (16).

$$\frac{dX_H}{dz} = \frac{dX_H}{dt} \left(\frac{dz}{dt} \right)^{-1} \quad (16)$$

Multiplying this value by the control volume discretized size provides an approximation for the percentage of control volume in non-equilibrium. Dividing the molar fraction distance-to-equilibrium by Equation (16) provides an approximation that describes where equilibrium is reached in the control volume. Equation (17) shows this approximation. Fig. 11 displays the equation across the field of interest.

$$CV_{\%} \approx \frac{X_H - X_{H,Eq}}{\frac{dX_H}{dz} \Delta z} \approx \frac{\Delta X_{H,Eq}}{\Delta X_{H,Reaction}} \quad (17)$$

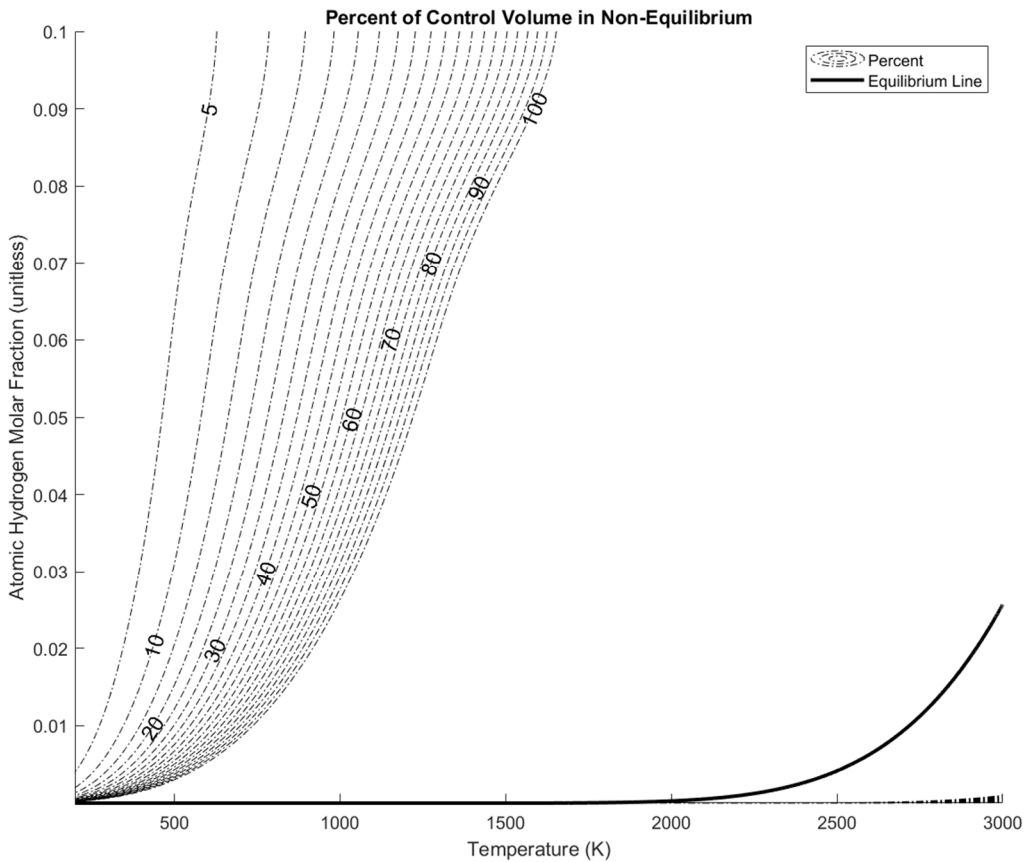


Fig. 11. Percentage of control volume in non-equilibrium up to 100%

The gradient area at the far left of Fig. 11 represents the region where reaction rates rapidly drive the atomic hydrogen to equilibrium before the end of the control volume. At 50%, the dissociation reaction reaches equilibrium at $\Delta z/2$ of the control volume. In the other regions without gradients, the reaction rate reaches equilibrium outside of the control volume and would require multiple control volumes to reach equilibrium. In fact, at higher temperatures, it takes upwards of 3.2 cm, or 2.5% of the length of the entire reactor to reach equilibrium. This demonstrates that at sonic speeds, flow within the field downstream of the inlet must be considered non-equilibrium.

Near the outlet, the flow will diverge and exhibit non-equilibrium behavior before ultimately reaching equilibrium before exit. Any inlet atomic hydrogen will remain at equilibrium until approximately 1600 K. Beyond 1600 K, the reactor enters non-equilibrium where atomic hydrogen production lags the equilibrium proportions by as much as 54% with flow at sonic speeds. Equation (18) shows the discretized stepping process that models an NTP reactor using Equation (17) where Δz_{sub} is the discretized step assumed 100 times smaller than the original Δz used in Equation (17).

$$X_H = X_{H,0} + \frac{dX_H}{dz} \Delta z_{sub} \quad (18)$$

Fig. 12 illustrates the operating line for the KIWI-B4E assuming global sonic conditions as a worst-case analysis.

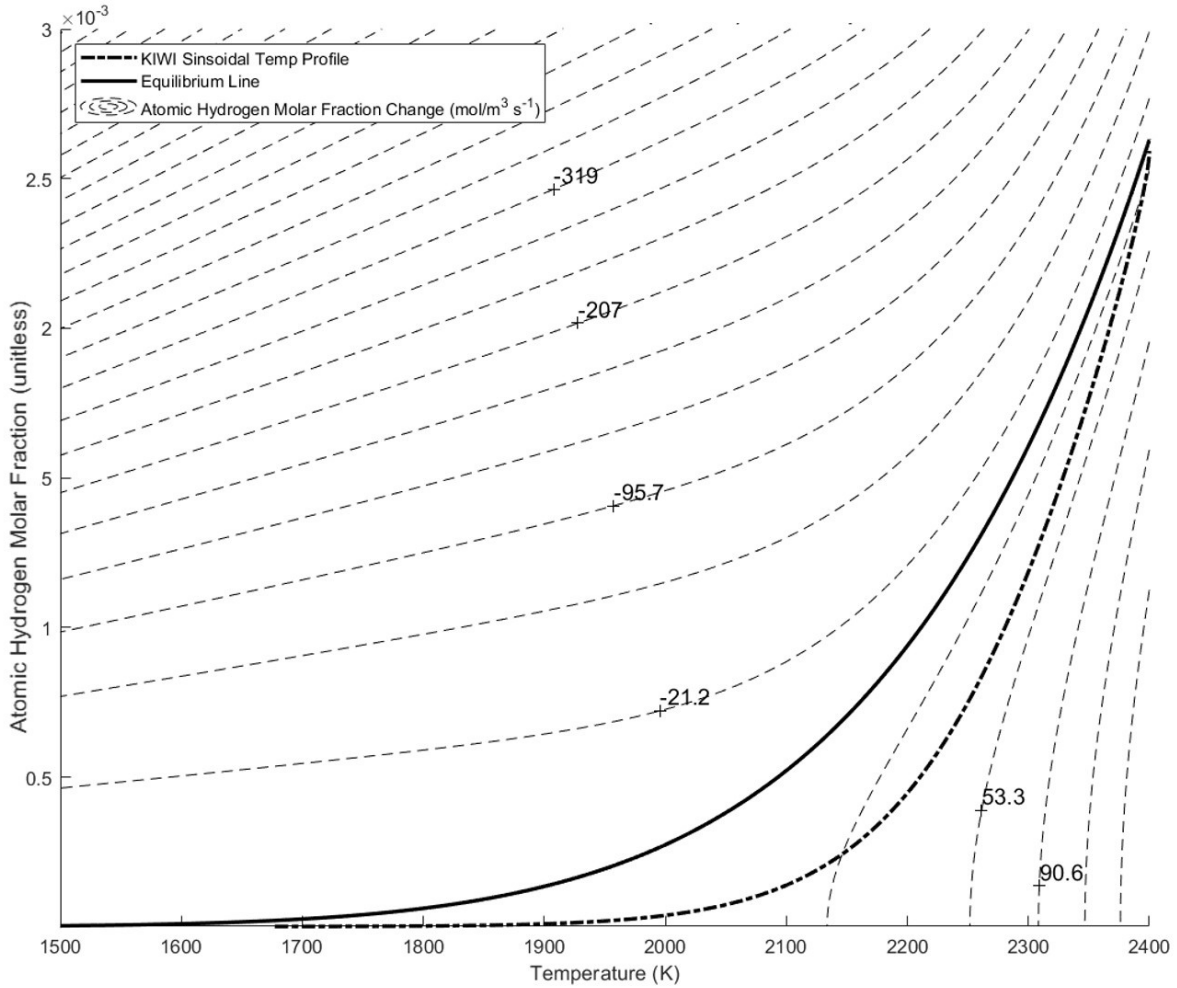


Fig. 12. KIWI-4BE reactor dissociation line within a reaction rate field

The positive reaction rates at the bottom-right of Fig. 12 increase the atomic hydrogen molar fraction back to equilibrium. The reactor closely approaches equilibrium at the exit providing a confident data point that the KIWI-4BE is at equilibrium prior to the rocket nozzle.

2.5. Existence of Atomic Hydrogen in Historic NTP Reactors

At slower than sonic speeds, all non-equilibrium effects are reduced. Slower global flow speeds permit the speed of the reaction rate to become dominant. The non-equilibrium region shrinks, and the field of equilibrium grows. However, the majority of the field remains in non-equilibrium. Fig. 13 shows flow speeds universally at Mach number 0.5 and 0.1. This can be compared to Fig. 11 above to see the collapse of the non-equilibrium field for slower speeds.

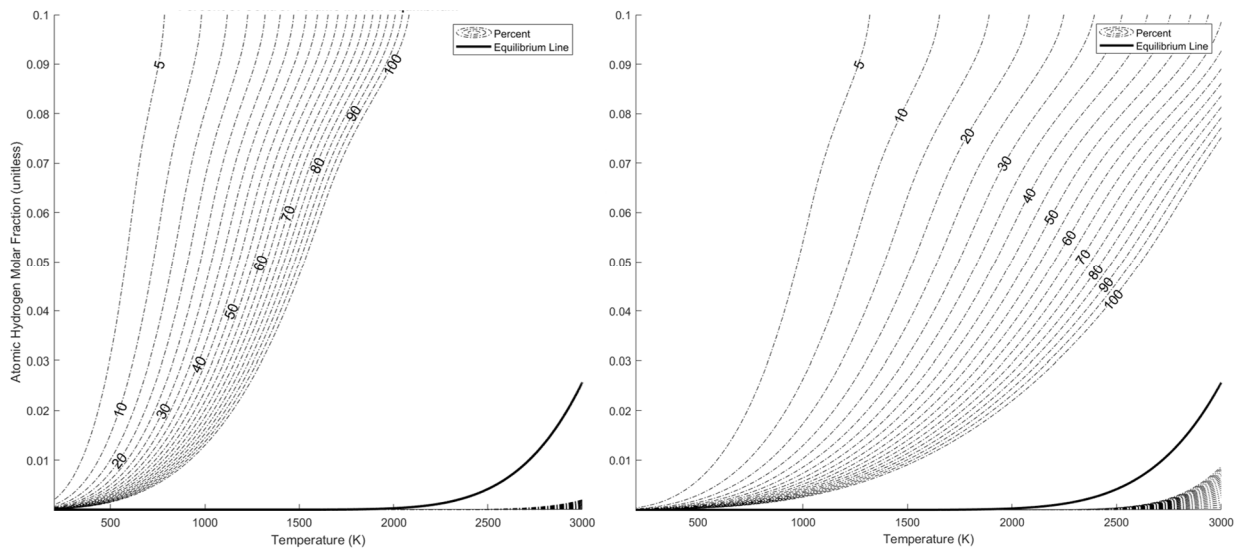


Fig. 13. Expansion of equilibrium zone at slower flow speeds for Mach 0.5 (left) and Mach 0.1 (right)

Considering the inlet speed of Mach number 0.02, the inlet would be represented by an even smaller non-equilibrium region than shown above. This representation shows that if flow

speeds are slow, non-equilibrium effects near the outlet will be reduced. However, it must be expected that heat addition in Rayleigh flow will accelerate the flow and the field could approach Fig. 11 shown above. Therefore, considering a Mach number of 1 remains the worst-case situation with all other flow speed cases approaching equilibrium.

For other temperature profiles, the equilibrium behavior is very similar, including non-equilibrium lag near the outlet. Linear, quarter-root, and square temperature profiles were considered to understand the behavior for varying temperature profiles in NTP reactors. Like the sinusoidal model, all temperature profiles have fast convergence to equilibrium at the reactor inlet due to rapid reaction rates. Likewise, equilibrium is maintained until approximately 1600 K. Beyond this point, the profiles lag equilibrium by producing atomic hydrogen rates lower than the simple equilibrium model, but all profiles closely approach equilibrium. Fig. 14 displays the molar fraction atomic hydrogen for varying temperature profiles.

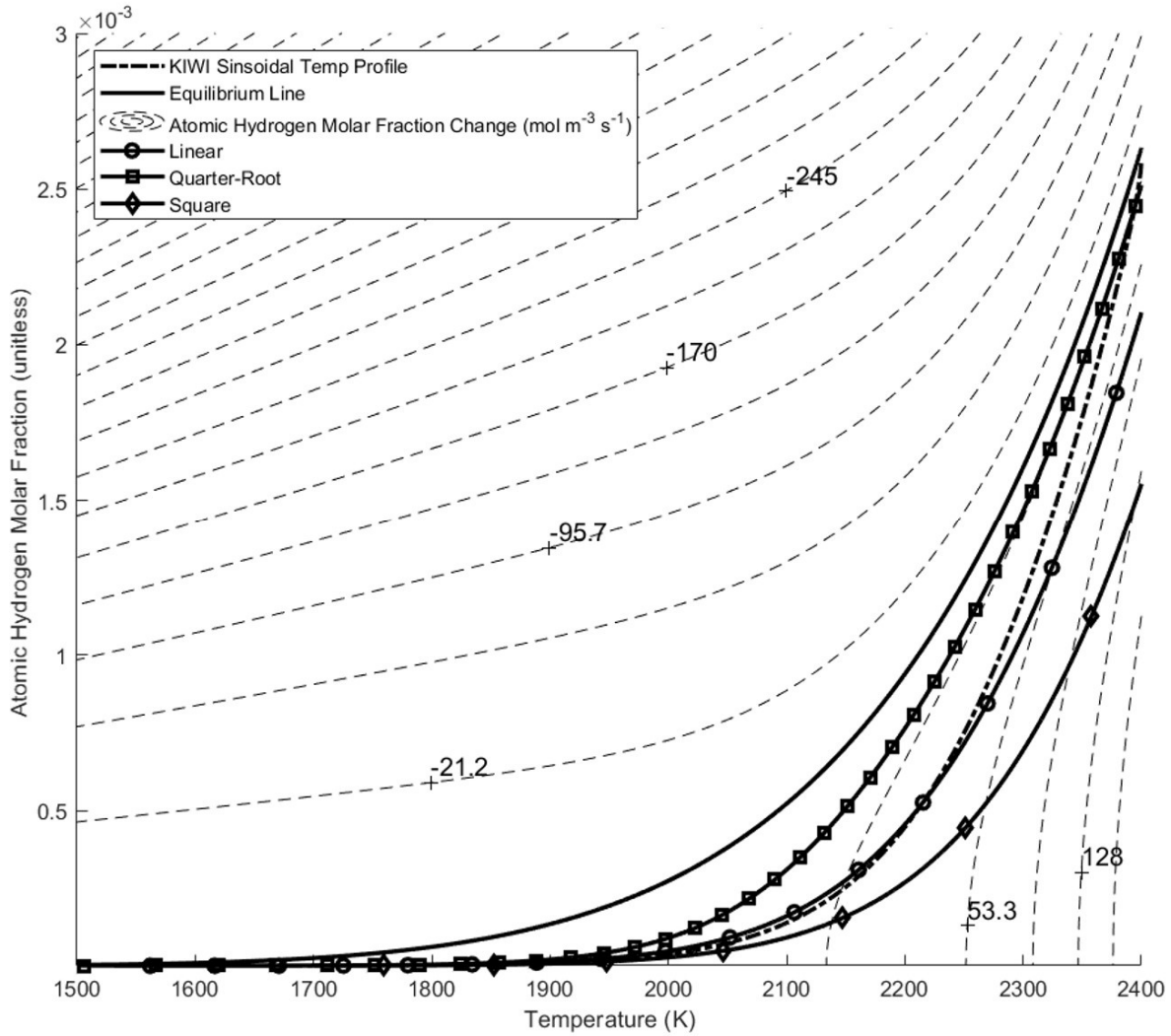


Fig. 14. Rise to equilibrium for varying temperature profiles

The square profile displays the greatest departure from equilibrium at the exit. This is due to high-temperature gradients near the outlet. Equation (19) shows the derivative relationship between molar fraction, temperature, and flow speed with respect to time.

$$\frac{dX_H}{dT} = \frac{dX_H}{dt} \left(\frac{dT}{dz} \frac{dz}{dt} \right)^{-1} \quad (19)$$

In considering the derivatives, the speed of sound increases in all profiles as temperature increases. The temperature gradient for the square profile is high near the outlet and highest of all profiles. At 1600 K, as the reaction enters non-equilibrium under positive reaction rates, the temperature gradient is positive and reduces the derivative in Equation (19). As the square profile approaches the outlet, the temperature gradient becomes increasingly positive which continues to slow the rise to equilibrium. The result is a square temperature profile that reaches the outlet well below equilibrium. This profile is interesting, but most reactor profiles do not follow the square profile and more closely resemble the other profiles.

The above findings and analyses are applicable to a variety of historic NTP engines and demonstrate a good correlation to equilibrium at all reactor exits. Like the KIWI-4BE in Fig. 14 above, the varying historic reactors all showed a chemical reaction in the engine that lagged equilibrium but reached equilibrium by the exit. The Phoebus-2A demonstrated the greatest non-equilibrium with the engine only at 50.97% of equilibrium at its furthest lag point to finally arrive at 84% of equilibrium at reactor outlet. The highest amounts of dissociated atomic hydrogen appear linked to the core exit temperature. The engines that followed closest to equilibrium appear linked to the operating pressure. To explore, ancillary analysis showed that increasing operating pressure increased equilibrium behavior in NTP reactors. Table 4 shows the results of the survey analysis.

Table 4. Historic NTP reactors & equilibrium behaviors of disassociated atomic hydrogen [66]

	KIWI-4BE	NRX-A6	Phoebus-2A	Pewee-1
Flow Rate (kg/s)	31.8	32.7	119.2	18.6
Core Inlet Temperature (K)	104	128	137	128
Core Exit Temperature (K)	2,330	2,472	2,283	2,556
Core Inlet Pressure (MPa)	4.02	4.96	4.73	5.56
Chamber Pressure (MPa)	3.49	4.13	3.83	4.28
Flow Percentage of Equilibrium Molar Fraction at Greatest Non-Equilibrium Point	53.35%	55.81%	50.97%	59.39%
Flow Percentage of Equilibrium Molar Fraction at Reactor Outlet	82.26%	93.91%	84.00%	95.60%
Molar Fraction Atomic Hydrogen at Outlet (Percentage of Total Concentration)	0.18%	0.33%	0.14%	0.48%

Extreme disturbances in the flow concentration beginning at 1600 K and 0.25% molar fraction operate at non-equilibrium but reach equilibrium at the reactor exit. Fig. 15 shows three cases to best understand the non-equilibrium affects near the equilibrium line.

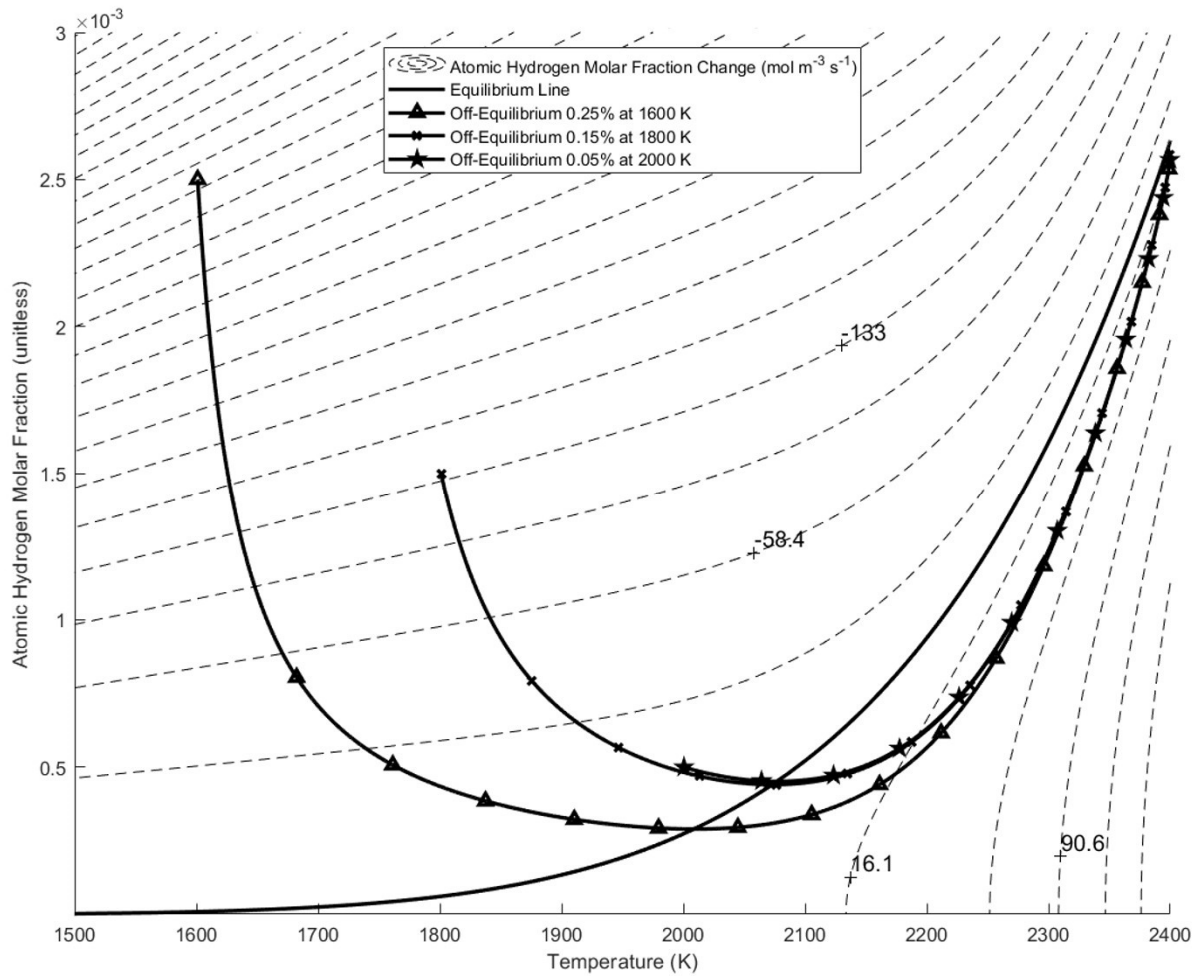


Fig. 15. Disturbances in high non-equilibrium reaching equilibrium at reactor outlet

For all cases, the curvature of the reaction rate is evident. Higher molar fractions had initial high reaction rates quickly correcting to equilibrium. However, as the test cases approached the equilibrium line, the low reaction rates froze the flow composition as temperature increased. Once the temperature increased beyond equilibrium, the positive reaction rates converged the flow to equilibrium. For initial atomic hydrogen values 1% molar fraction or less, equilibrium is achieved at the outlet.

Chapter 3 Surface Reaction Dissociation and Impact on NTP Flow

3.1. Materials and Methods

An appropriate model can be built that shows hydrogen absorption produces a significant perpendicular velocity into pipe walls altering the boundary layers in the pipe and changing the thermal heat transfer to the bulk flow. An appropriate model can simplify the phenomena for observation as the flow is heated along the reactor.

Molecular hydrogen adsorbs onto surfaces in a dissociative way. As the molecule approaches the surface, it dissociates, and each hydrogen atom binds to a unique surface location. Heriksson et al. show that previous experiments found adsorption sites to dissociate molecular hydrogen and highlighting that later the atoms would be found to occupy bridge sites [67]. Zheng and Gallagher found that at temperatures above 1200 K only atomic hydrogen was prevalent on the surface [68]. Each incident molecule provides two atoms of hydrogen. Opposite to adsorption, desorption of atomic hydrogen always recombines on leaving the surface. Two atoms that desorb will recombine to make a hydrogen molecule ejected from the surface [69]. This is an essential note for formulating the adsorption and desorption rate equations.

Coverage is calculated from occupied sites, n , versus total tungsten atoms, n_T , in Equation (20).

$$\theta = \frac{n}{n_T} \quad (20)$$

The surface is assumed to be clean, defect-free, surface tungsten oriented in a face-centered cubic structure commonly referred to as $\{0\ 0\ 1\}$. For every tungsten atom, there are two vacancies for atomic hydrogen. The coverage saturates at $n = 2 \times 10^{15} \frac{\text{atoms}}{\text{cm}^2}$ and $\theta = 2$ representing two hydrogen atoms to one tungsten atom and defining $n_T = 1 \times 10^{15} \frac{\text{atoms}}{\text{cm}^2}$ [70].

The temperature range of interest is from 200 K to 2900 K in flow and surface temperatures. In an NTP reactor, heat transfer causes the bulk flow to follow a sine distribution from 200 K to 2500 K. The NTP cladding surface is approximately 200 – 400 K hotter than the bulk flow [71]. This constrains the region of interest and establishes a relationship between bulk, also referred to as gas temperature, and surface temperature.

Both bulk flow and boundary layer contain a mixture of molecular and atomic hydrogen that follow equilibrium concentrations. NTP bulk flow was validated for assumption at equilibrium up to 1600 K [72]. Timescales can correctly assume chemical equilibrium throughout this study considering the flow decelerates to near zero velocity at the wall.

Dissociation in the bulk flow creates a mixture of molecular and atomic hydrogen. The contribution of atomic hydrogen to adsorption, desorption, and absorption is neglected due to the much smaller ratio of atomic hydrogen at comparable sticking coefficients, s . The sticking coefficient for atomic hydrogen was found to be less than 0.6 in molecular dynamic simulations [73]. The amount of atomic hydrogen in the bulk flow is no more than 0.5% and will not climb above 1.9% in the boundary layer [74]. Considering both effects, the atomic hydrogen that approaches and directly sticks to the surface is considered negligible.

The above assumptions can be used to solve a rate equation for the generation of hydrogen on NTP cladding walls and investigate absorption. NTP reactors typically operate with predictable surface temperature profiles between 300 K and 2900 K. Numerics is used with these known reactor surface temperatures along with an array of bulk gas temperatures to illustrate coverage of hydrogen at all possible conditions. This coverage is time-dependent and time-stepped until reaching a limiting value of θ_{eq} where rate equations equal zero as described in the following section of theory. Numerics uses each θ_{eq} to calculate the absorption at each surface temperature

which correlates to a specific position in the reactor. The applicable thermal boundary layer is overlaid the data set and NTP behaviors observed.

3.2. Theory

The overall hydrogen removed from the flow is governed by the rate of hydrogen coverage on the NTP surface cladding material. The rate of adsorption and desorption is much faster than the rate of absorption meaning $\frac{dn}{dt} \gg \frac{dn}{dt_{abs}}$ at all considered gas and surface temperatures. Absorption is not considered in the initial rate equation and surface equilibrium is accepted for all surface conditions. Equation (21) displays the rate of atomic hydrogen coverage change on the surface where n is the number of adsorbed hydrogen atoms on the surface.

$$\frac{dn}{dt} = \frac{dn}{dt_{ads}} - \frac{dn}{dt_{des}} \quad (21)$$

Because of the faster surface reaction, the coverage can be assumed to be at equilibrium between adsorption and desorption throughout the reactor. This powerful concept means that the calculation for absorption can use the equilibrium value for coverage, θ_{eq} , throughout the study. This value is observed as $\lim \frac{dn}{dt} \rightarrow 0$ in Equation (21) on the tungsten surface.

3.2.1 Adsorption Equation

The rate of adsorbed atoms is governed by the incident molecular hydrogen flux and the sticking coefficient. Equation (22) displays the adsorption equation where s is the sticking coefficient and $0 \leq s \leq 1$, and the term in the parentheses is the incident flux, ϕ [75].

$$\frac{dn}{dt_{ads}} = s \left(\frac{P}{\sqrt{2\pi mkT_g}} \right) = s\phi \quad (22)$$

P is the operating pressure assumed constant at NTP conditions of 3.49 MPa, m is the mass of one hydrogen molecule, k is the Boltzmann constant, and T_g is the gas temperature, or bulk temperature, beyond the boundary layer.

The adsorption equation has two key dependencies worth investigating. The sticking coefficient, s , is a function of the coverage, θ , and an initial sticking coefficient, s_0 , as shown in Equation (23).

$$s = s_0 \left(1 - \frac{\theta}{2} \right) \quad (23)$$

The initial sticking coefficient is known to change with gas temperature. NTP systems span a reactor condition from 200 K to 2500 K which equates to a range of incident energies. Fig. 16 displays a literature review spanning this region.

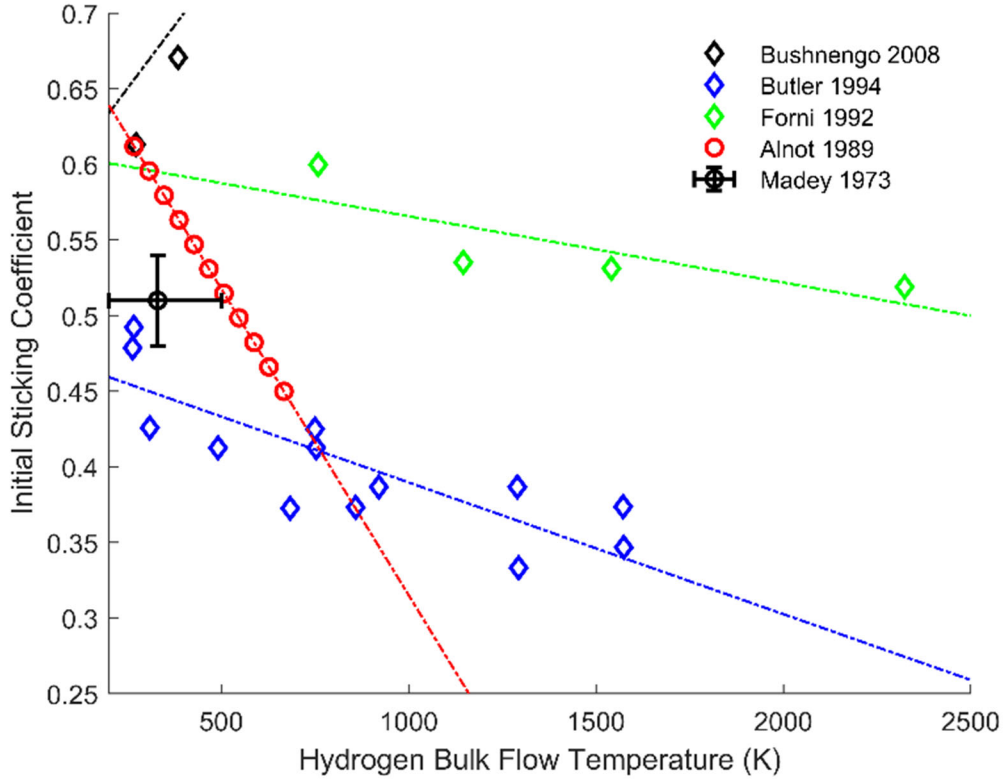


Fig. 16. Initial sticking coefficient of tungsten for NTP reactor incident temperatures

The initial sticking coefficient of tungsten $W\{1\ 0\ 0\}$ to hydrogen at varying bulk flow temperatures has a controversial past. The earliest results by Madey captured a $s_0 = 0.5 \pm 0.03$ [76]. Alnot provided an expression of $s_0 = 0.72 - 4.05 \times 10^{-4} T_g$ [77]. Forni includes a classical quantum calculation with resulting values between 0.4 and 0.6 for a large range of energies [78]. Butler would later support the trend of Alnot's data, but present a slightly different data set [79]. Bushnengo would attempt to resolve these differences but instead introduce data that is off-chart high, climbing to nearly $s_0 = 0.93$ by 1170 K [80].

Butler's data is selected as the most conservative approach. Less than 1000 K, the initial sticking coefficient is clustered between 0.4 and 0.6 with the exception of Bushnengo's data.

However, above 1000 K, all data sets tend to diverge. Forni, Butler, and Alnot correlate a trend. However, Alnot's data is not reported above 667 K while Butler's data extends into NTP temperature areas. Further, Alnot's data reaches $s_0 = 0$ while no other data set indicates this condition.

3.2.2 Desorption Equation

The rate of desorbed atoms is governed by several variables including coverage (θ) the total hydrogen saturation value (n_s), a frequency factor (ν), an energy of desorption (E_d), and the surface temperature (T_s). Equation (24) shows the governing equation [81].

$$\frac{dn}{dt_{des}} = \frac{1}{2} \left(\frac{n_s}{2} \right)^2 \theta^2 \nu e^{-\frac{E_d}{RT_s}} \quad (24)$$

The surface atoms rearrange to a more stable pattern decreasing the frequency factor and energy of desorption as adsorption increases surface coverage. At approximately $\theta = 0.5$ the field of attractive and repulsive forces moves the hydrogen atoms to new stable positions that alter the interatomic distances and binding sites spread along the tungsten surface. This new pattern includes a much smaller desorption energy along with a smaller frequency factor. The results are a varying frequency factor and energy of desorption that must be modeled with coverage [82]. This approach is validated in other work. Hodille showed a similar energy change with results about 18% higher than Alnot. Hodille recognizes this expectation, given his surface is damaged while Alnot's is clean and defect-free [83]. The rearrangement does not alter the adsorption rate.

3.2.3 Absorption Equation

The rate of absorption is the speed with which the adsorbed atoms move into the NTP surface governed by the number of occupied sites, as shown in Equation (25). Because $\frac{dn}{dt} \gg \frac{dn}{dt_{abs}}$, Equation (21) can be expressed with the equilibrium coverage (θ_{eq}).

$$\frac{dn}{dt_{abs}} = k_{abs}n = k_{abs}n_t\theta_{eq} \quad (25)$$

The reaction coefficient, k_{abs} , is governed by the surface temperature as shown in Equation (26).

$$k_{abs} = 5.66 \times 10^{12} e^{-\frac{206500}{RT_s}} [s^{-1}] \quad (26)$$

This equation is found in molecular dynamic simulations. The simulations look specifically at a surface-bound hydrogen atom that penetrates the surface. It is a careful consideration of the most likely path the atom will travel along the surface and sublayer potential energy surfaces, including bridge, saddle, and centered interstitial sites [84]. The energy barrier of this absorption is very high, hence the very slow speed compared to the other phenomena of adsorption and desorption.

3.2.4 Mass Flow, Calculation of v_w into Wall

The mass flow rate of atomic hydrogen into the NTP cladding is expressed through a simple mass flux rate comprised of the velocity into the wall, v_w , and the surface area of the NTP cladding, A in Equation (27).

$$\dot{m} = \rho v_w A \quad (27)$$

The hydrogen density, ρ , is governed by the ideal gas law in the boundary layer.

Consider the units of Equation (25) above where $\frac{dn}{dt_{abs}} \equiv \left[\frac{atoms}{m^2s} \right]$. If $m \equiv \left[\frac{kg}{atom} \right]$, then

Equation (27) can be rearranged to solve for the velocity into the wall in Equation (28).

$$v_w = \frac{m}{\rho} \frac{dn}{dt_{abs}} = \frac{n_T k}{P} k_{abs} T_s \theta_{eq} \quad (28)$$

The leading term in Equation (28) is constant. $k_{abs} T_s$ is a function of surface temperature and θ_{eq} is calculated in a previous step.

3.3. Findings/Results

3.3.1 Coverage Decreases with Increasing Surface Temperature and Gas Temperature

Fig. 17 shows the θ_{eq} across the considered NTP surface temperatures for varying gas temperatures.

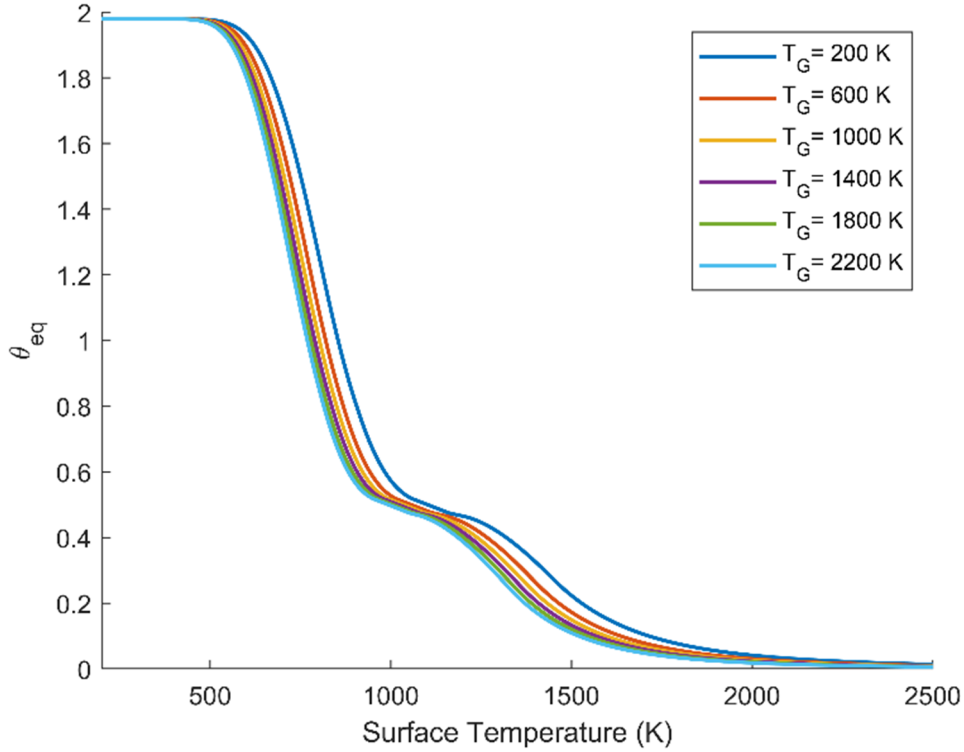


Fig. 17. Adsorption/desorption equilibrium levels on tungsten cladding

The hydrogen coverage decreases as surface temperature increases and approaches $\theta = 0$ near 2500 K. The coverage decreases as gas temperatures increase. The coverage is strongly affected by surface temperatures while weakly affected by gas temperature.

Numerics run for the same cladding but at LEU representative pressures of ~ 7 MPa shift the θ_{eq} to the left in Fig. 17 by only 100 – 200 K. The increase of 3 MPa between the KIWI engine and modern LEU designs shows little change in equilibrium coverage.

3.3.2 Coverage Approaches $\theta_{eq} = 0$ beyond 2000 K.

Fig. 18 shows the surface coverage as a percentage of saturation for all gas and surface temperatures. The lines plotted represent a 400 K and 200 K difference in gas and surface temperatures to illustrate a range of thermal boundary layers.

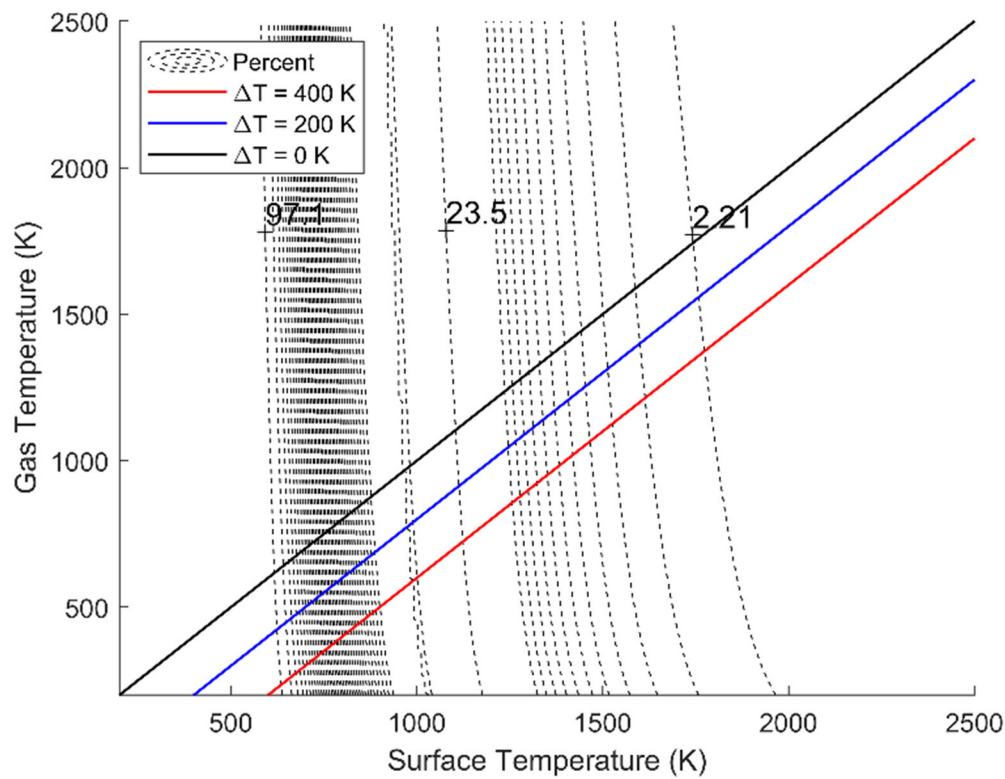


Fig. 18. Surface coverage of hydrogen at equilibrium as a percent of saturation

The surface coverage decreases at increasing surface temperatures. The coverage is high for all gas temperatures below a surface temperature of 650 K. The coverage is only 23.5% of saturation approaching 1000 K surface temperature. The coverage percentage is less than 2.21%

at all gas temperatures near a surface temperature of 2000 K. Here are a couple examples to illustrate the sensitivity of temperature change. To raise the gas temperature from 600 K to 1000 K at a constant surface temperature of 600 K, the surface coverage only changes by -0.1%. To raise the surface temperature from 600 K to 1000 K at a constant gas temperature of 600 K results in a change in -72.2% of surface coverage.

Zheng and Gallagher provide similar results by experimentally observing the mechanism for adsorption, namely hydrogen dissociation, has only a 5 - 6% probability of occurring at surface temperatures at 2200 K and pressure independent [85].

3.3.3 Crossflow is Maximum at NTP Reactor Outlet

Fig. 19 displays the total calculation of the crossflow velocity, v_w , into the wall. The maximum for $\Delta T = 400 K$ is approximately $v_w \approx 80 mm/s$. There is negligible crossflow into the wall below a surface temperature of 1500 K despite the higher surface coverage. The crossflow velocity climbs from low values at 1500 K to a peak value near the outlet of the reactor.

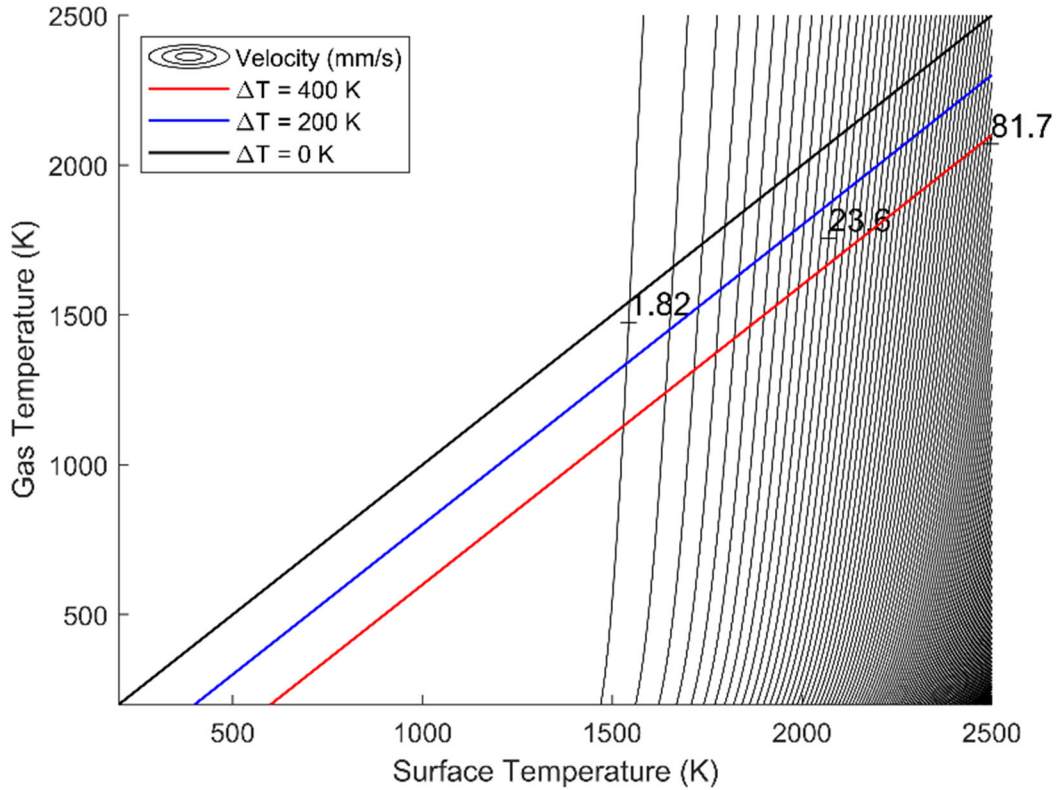


Fig. 19. Crossflow velocity due to hydrogen absorption

Higher temperatures are necessary to induce absorption and so align with the reactor outlet, or highest temperatures. Johnson et al. have shown details in molecular dynamic simulations that surface absorption into the first and second layer contain a high energy barrier of 2 eV [86].

Modern LEU systems at ~ 7 MPa reduce the maximum crossflow velocity to $v_w \approx 56 \frac{mm}{s}$. This is a 30% reduction in the wall velocity over historic KIWI B4E engine. This value is a comparison to the conditions in LEU engines and not a direct measurement of molybdenum-tungsten alloy cladding. See the previous comments in Chapter 1 on the selection of pure tungsten over the alloy.

3.4. Discussion

Cross-flow velocity is present at historic and modern NTP operational conditions. A characterization of these findings follows describing the severity and end with a description of impact to NTP operations. The historic KIWI B4E engine is used as a reference point with delineations to modern engines noted.

There is no appreciable crossflow velocity of hydrogen within the plotted boundary layer representation at low surface temperatures. Adsorption dominates desorption below 1000 K creating high coverages, as shown in Fig. 18. The absorption energy barrier at these temperatures is too high, negating any penetrating effect. Fig. 19 demonstrates that notable absorption begins around a surface temperature of 1500 K.

The maximum crossflow velocity is found at the highest surface temperatures. At a $\Delta T = 0\text{ K}$ the maximum crossflow velocity is 78 mm/s. The maximum crossflow velocity of 81 mm/s occurs at more realistic boundary layers of $\Delta T = 400\text{ K}$. These values represent a significant speed of hydrogen penetration but may not represent a significant change to the velocity and temperature profiles.

A worthwhile comparison of crossflow velocity can be made to other wall suction fluid mechanics attributes. The parameter of interest is F , shown in Equation (29) as the ratio of the crossflow velocity to the freestream velocity, U_e .

$$F = \frac{v_w}{U_e} \quad (29)$$

This data jumps from $F = 0$ to $F = 0.003$. Much lower values of F are needed to observe the extreme bulk flow speeds (U_e) in NTP reactors.

White conducts a significant analysis of flat-plate flow with turbulence and suction at lower values of F [87]. White plots expressions from Moffat and Kay comparing F values for Stanton numbers and turbulent velocity profiles in Figs. 20 and 21, respectively. For the KIWI-B4E NTP engine, the Mach number is anticipated to be 0.5 from Rayleigh heating but cannot be above 1.0. Given the speed of sound is 1190 m/s, this results in a freestream velocity as low as 595 m/s [88]. This speed provides a value of $F = -2.19 \times 10^{-4}$ indicating suction by the negative sign.

Lushchik et al. demonstrated even for larger F values, the temperature profile is only altered in the wake, and beyond region [89]. This effect is much smaller than the changes in velocity. The thermal profile become thinner with the entire profile becoming blunter. This change appears to be experimentally very small with little notable change across Reynolds numbers.

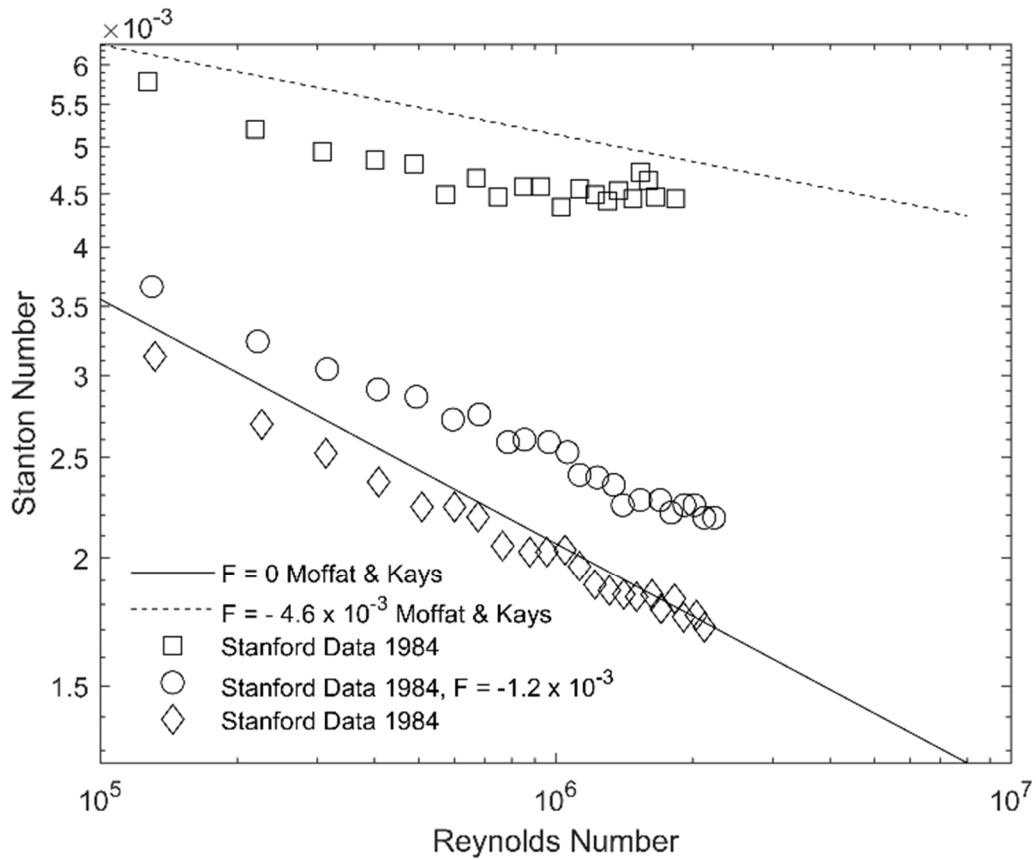


Fig. 20. Stanton numbers for various F values [90]

Fig. 20 shows the impact to heat transfer by observing the change to the NTP Stanton Number. The KIWI-B4E is about 18% of the Stanford data, depicted as circles. The trend of this data indicates that the KIWI-B4E engine likely lies very close to the $F = 0$ line. Flat plate flow follows predictable skin friction coefficients and Stanton numbers along the line $F = 0$.

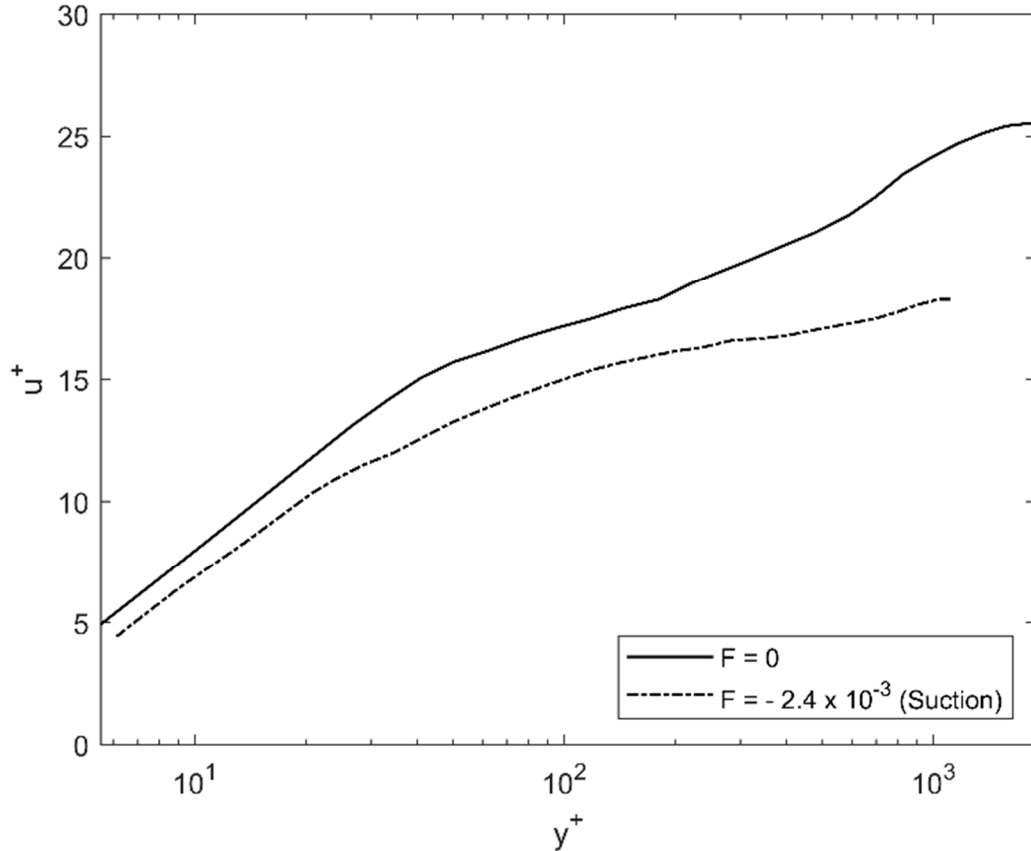


Fig. 21. Velocity profiles for various F values [91]

The F value of -2.4×10^{-3} in Fig. 21 is 10 times that of the KIWI-B4E engine. The actual location of NTP F value may not reside near $F = 0$. The viscous sublayer appears to be very similar for all F values admittedly suggesting that NTP contains a viscous sublayer that matches $F = 0$ sublayers. Beyond the buffer layer an inertial sublayer appears to diverge indicating that $F = -2.19 \times 10^{-4}$ merits further CFD investigation and solution of turbulent NTP duct flow.

Further analysis shows that due to the change in the boundary layer along the reactor, wall suction may create near-wall regions of rotation and potentially backflow. White highlights that

suction draws in the turbulent boundary layer and changes the overall shape. The wall Reynolds number of Equation (30) dictates the shape of the velocity profile [92].

$$Re_w = \frac{v_w r_0}{\nu} \quad (30)$$

Calculations show values as high as $Re_w = 1.43$ near the outlet, and possibly higher toward the middle of the reactor, indicating a notable reshaping of the velocity profile due to suction. The reshaping of the profile changes along the axis of the reactor and only in areas of significant absorption. The changing boundary layer along the reactor leads to regions of decelerating flow due to momentum transfer into the wall. Fig. 21 above describes how absorption will decrease u^+ while Fig. 19 shows cross flow velocity increasing throughout the reactor. The result is a deceleration of the outer wake as the flow progresses through the reactor. This is confirmed in direct numerical simulations (DNS) that show under increasing suction values a decreasing flow velocity in the outer wake [93]. The NTP will also experience an increase in flow velocity as heat is transferred to the flow. This decrease in the velocity profile coupled with the increasing flow velocity requires further research in CFD analysis to observe any significant performance change on the engine to include rotational flow.

All previous analyses involved flat-plate flow. Further concern is expressed by stepping into pipe flow. White approaches porous pipe flow through the Reynolds-Averaged Navier-Stokes (RANS) equations assuming the form of a stream-wise function. He finds that porous pipe flow suffers from non-uniqueness and continuity of analytical solutions for various Re_w [94]. He concludes that fully developed flow may not occur for many cases. This serves as another indication that further research is required under CFD. Suction solutions of porous pipe flow are shown in Table 5.

Table 5. White’s exploration of porous pipe flow [95]

Re_w	Solution
0 – 2.3	Double solutions, one with backflow
2.3 – 9.1	No solutions within this range
> 9.1	Multiple sets of double solutions.

The above discussion outlines several issues that arise due to the crossflow in NTP engines that impact design and operation including changing boundary layer shape, reduced mass flow rate, and potentially backflow. The central concerns surround the impacts in temperature, mass, and velocity.

The above analysis describes a relatively low mass loss to the wall. The decelerating turbulent boundary layer is a concern for its degrading effect on the energy provided to the crossflow velocity into the wall with the momentum of the flow is redirected from the chamber into the reactor wall. Additionally, backflow can complicate the heat transfer reducing the effectiveness of the reactor heat transfer. The implications to NTP are an expectation of a propulsion system that overestimates performance when $T_{chamber}$ is decreased, subsequently reducing V_{exit} and m_{dot} or \dot{m} is decreased due to the reduced mass flow through the walls. Additionally, the velocity from the reactor to the chamber is also reduced while axial velocity is converted into radial velocity and not useful for thrust in the axial direction.

Changing reactor cladding materials is expected to increase the cross-flow removing mass from the flow and altering the velocity profile. To select Mo-W is to increase the permeability of the cladding as mentioned above. This could provide the flow a stable and asymptotic turbulent boundary layer but the variability of cladding absorption through the reactor would not support

this. Currently, molybdenum is accepted due to an acceptable penetration depth ZrC historically was used but the coefficient of thermal expansion differences between the cladding and the fuel were found to be too large resulting in cracking and hydrogen penetration directly into the underlying uranium composite fuel. Additionally, the carbide reacted with hydrogen, albeit at low levels, to produce methane and acetylene [96]. These heavy byproducts drive the molecular weight of the propellant flow up reducing the exit velocity albeit slightly.

Chapter 4 CFD Analysis of Dissociation Reactions in NTP Flow

4.1 Methods and Measurements

An extensive campaign to mesh, solve, and converge a CFD model is presented below. The result is CFD data that is smooth and continuous with no imbalances and all residuals below 10^{-5} .

4.1.1 Basic CFD Geometry Setup and Boundary Condition Assumptions

The setup is a 2-D axisymmetric pipe with no swirl out of the 2-D plane. The hot wall is a sinusoidal model fit from the KIWI-4BE geometry. The temperature profile is modeled from the concept in Emrich's description in his book and validated by other text [97, 98]. The absorption into the wall is modeled as a Dirichlet boundary condition at local radial positions in the flow. This boundary condition is a function of the axial position and changes in a sinusoidal pattern along the length of reactor.

4.1.2 Rejection of LES and Selection of RANS

Large eddy simulation (LES) was initially considered for this study. However, the cell count became prohibitive in managing smaller eddies near the wall. Decreasing cell height to account for eddies required decreasing cell width to manage the aspect ratio. The overall cell count became prohibitive, and the approach was abandoned for the Reynolds-Averaged Navier-Stokes (RANS) equations using the $k - \omega$ SST model. This wall model was selected to balance the blending of the $k - \epsilon$ model closer to the free-stream with accurate turbulent kinetic energy (k) and dissipation rates (ϵ) near the wall. Further, the lack of excessive cells was enticing for computational resources and time, redirecting the focus to ensuring cell height was small enough to resolve the high-temperature gradients and potentially fast crossflow into the wall. This made the cell width less important within the expected slow axial speed region of the boundary layer,

but cell height was very important to resolve temperature gradients as well as crossflow velocities. RANS also included a possibility of unsteady considerations that were also considered, given the potential for transient solutions.

4.1.3 Solution Steering

Initial solutions were oscillatory and divergent, challenging the establishment of under-relaxation factors. Initially, under-relaxation factors of as high as 0.9 provided initial convergence but became oscillatory and required reduction as low as 0.4 for flow, turbulent kinetic energy, and dissipation rate. Second-order solutions were switched to first-order upwind solutions that eliminated oscillations and drove very slow convergence. The concern for accuracy under this method led to ANSYS Fluent's Solution Steering feature that blends between first and second-order modeling while iterating to seek the highest order within the flow field while seeking convergence.

After 100,000 iterations and 50 hours of run-time, the solutions provided a flow field with a weak convergence of mass, momentum, and energy to residuals no better than 10^{-3} . Additionally, local and global imbalances of discontinuous solution values occurred within the flow indicating the transients preventing a final steady solution.

4.1.4 RANS Convergence and the Transient State

After 270,000 iterations over 130 hours of run-time, the model demonstrated a continual transient state with residuals and imbalances that were periodic in nature. Using the transient setting in Fluent produced convergence for some flow variables with very long iteration counts but required even more computational time and resources and did not lead to convergence of all mass, momentum, and energy. Residuals would move toward convergence but solution monitoring

would show periodic unexplained regions of circulation, reverse flow, and other disturbances that would resolve within the flow solution only to reappear in later solutions. Best convergence was 10^{-1} for hydrogen species, 10^{-2} for energy, and 10^{-3} for velocity components. These traveling disturbances continued throughout flow solution monitoring for weeks indicating a fully transitory behavior operating at different timescales within the flow.

4.1.5 Selection of the Pseudo-transient Method

The pseudo-transient method achieved a steady-state solution after the realization of the multiple timescales at work with the flow. Table 6 shows the representative timescales within the flow.

Table 6. Timescale of the various flow phenomena

Phenomena	Timescale 10^n (seconds) (n =)
Dissociation / Recombination	-12
Adsorption / Desorption	-9
Flow Residence Time (1 Cell)	-6
Absorption into Cladding	-3

ANSYS Fluent contains a solver that can relax the flow's solution using a pseudo-transient time step. Under-relaxation factors can aid convergence by reducing the incremental solution among the nodes. However, when varying timescales are at work, a single under-relaxation factor can be unsuitable for capturing the events occurring at different positions and resolutions of time. Some events even move forward and backward in action, confounding simplifying assumptions in CFD. The Fluent solver introduces a pseudo time step and gradients into the underrelaxation factor,

which aids in driving the solution matrix toward a diagonally dominant matrix that can converge to a solution [99].

4.2 Theory

Chapters 2 and 3 present equations and modeling for bulk dissociating flow and surface reactions, respectively.

4.2.1 Compressible, Reynolds-Averaged Navier-Stokes Equations

The ANSYS Fluent program contains many methods, techniques, and controls for solving computational fluid dynamics problems. Laminar calculations are inaccurate when pipe flow extends $Re_D > 3500$. This study explores $10^4 < Re_D < 10^6$ well above this limit, indicating fully turbulent flow. The Reynolds-Averaged Navier-Stokes (RANS) equations provide the equations of motion for this turbulent case. Equation (31) shows the mass equation where ρ is the mixture density, x is the coordinate along the reactor axis, u is the velocity in the axial direction, v is the velocity in the radial direction, r is the radius of the pipe, and S_{mass} is a source, or sink, term where mass is inserted or removed from the flow [100].

$$\frac{\partial \rho}{\partial t} + \nabla \cdot \rho \bar{v} = S_{mass} \quad (31)$$

The momentum equation assumes a 2-D axisymmetric case without swirling and is shown in Equation (32).

$$\frac{\partial}{\partial t}(\rho \bar{v}) + [\nabla \cdot \rho \bar{v} \bar{v}] = -\nabla \bar{p} - [\nabla \cdot (\bar{\tau}^v + \bar{\tau}^t)] \quad (32)$$

The ensemble time average velocity, \bar{v} , includes the average velocity as well as velocity fluctuations. The viscous and turbulent stresses, $\bar{\tau}^v + \bar{\tau}^t$, describe the flow. The time-averaged

pressure the vector form shown in the above equation must be carefully expanded, following the Navier-Stokes conventions, to the 2-D axisymmetric case within the cylindrical coordinate system while retaining the turbulent components. The unsteady terms are retained in the equations to emphasize the unsteady case, as described above, when the engine is initially started. However, the model does reach a steady state condition where transient terms can be assumed to be zero.

The energy equation is shown in Equation (33) where \bar{e} is the internal energy, \bar{h} is the total enthalpy that includes the enthalpy of the individual species and S_h the reaction source term. The final term, S_h , adds or removes energy from the flow due to the chemical reactions.

$$\frac{\partial}{\partial t} \rho \left(\bar{e} + \frac{1}{2} \bar{v}^2 \right) + \nabla \cdot \left[\rho \vec{v} \left(\bar{h} + \frac{1}{2} \bar{v}^2 \right) \right] = -\nabla \cdot (\bar{q}^v + \bar{q}^t) + \mu(\bar{\Phi}_v^v + \bar{\Phi}_v^t) + S_h \quad (33)$$

4.2.2 Species Conservation

To track the amount of atomic hydrogen in the flow, the continuity of species is also tracked in Equation (34) [101]. The mass fraction, ω_i , transports the value for each species while R_i and S_i handle any internal chemical reactions and external species sources, respectively.

$$\frac{\partial}{\partial t} (\rho \omega_i) + \nabla \cdot (\rho \vec{v} \omega_i) = -\nabla \cdot \vec{J}_i + R_i + S_i \quad (34)$$

This equation is paramount to calculating the mixture densities used in the in the governing equations above.

4.2.3 Selection of $k - \omega$ SST Model

Turbulence can greatly affect the behavior of boundary layers near walls. Evolution of wall functions have tried to best model the changes to near-wall fluid properties. Two additional partial differential transport equations calculate the turbulent kinetic energy, κ , and turbulent dissipation

rate, ϵ , and provide it at each location in the flow known as $\kappa - \epsilon$ models and is a model for RANS closure [102]. This method has blended with ever increasing accuracies of two-equation models. This analysis uses the $k - \omega$ SST model that includes a blending between near-wall and bulk flow for highest accuracies. ω is the dissipation per unit turbulent kinetic energy and has found to perform very well in a variety of flows including circular ducts. The cladding material contains no unusual roughness and is assumed smooth. No damping coefficients were changed from those that worked in the original publication [103].

4.2.4 Calculation of y^+ for Placement.

The radial placement of the mesh was closely considered due to the turbulent duct flow, high temperature gradients, and velocity gradients. The first layer was placed at 30% radius of the $y^+ = 1$ value and the subsequent 30 layers were very closely placed to ensure capture of these gradients. A fine mesh was used on to $y^+ = 300$. Equation (35) shows the calculation.

$$y^+ = \frac{yv_*}{\nu} \quad \text{where } v_* = \sqrt{\frac{\tau_w}{\rho}} \quad (35)$$

$$\tau_w \approx 0.079Re_D^{-0.25} \quad \text{and } Re_D = \frac{UD}{\nu}$$

Concern for initial y^+ calculation without final knowledge of the freestream velocity, U led to a worst-case calculation for the friction velocity, v_* . $y^+ = 1$ was located at $y = 2e-5$ m. Later refinement of the mesh to large first grid size provided bad convergence and was returned to this value very small value.

4.3 Results

4.3.1 Temperature and Velocity Boundary Layer Development of the Chemically Reacting Flow

Centerline flow measurements did not differ from 10% radius values and so were removed for clarity. The centerline reached a value 2432 K while the near-wall value of 90% radius reached 2579 K. Fig. 22 shows the behavior of the steady-solution of the dissociating bulk and surface reacting flow. The wall temperature is shown as a reference. Along the reactor, the temperature increases with the wall rise in temp and the temperature profile becomes more pronounced.

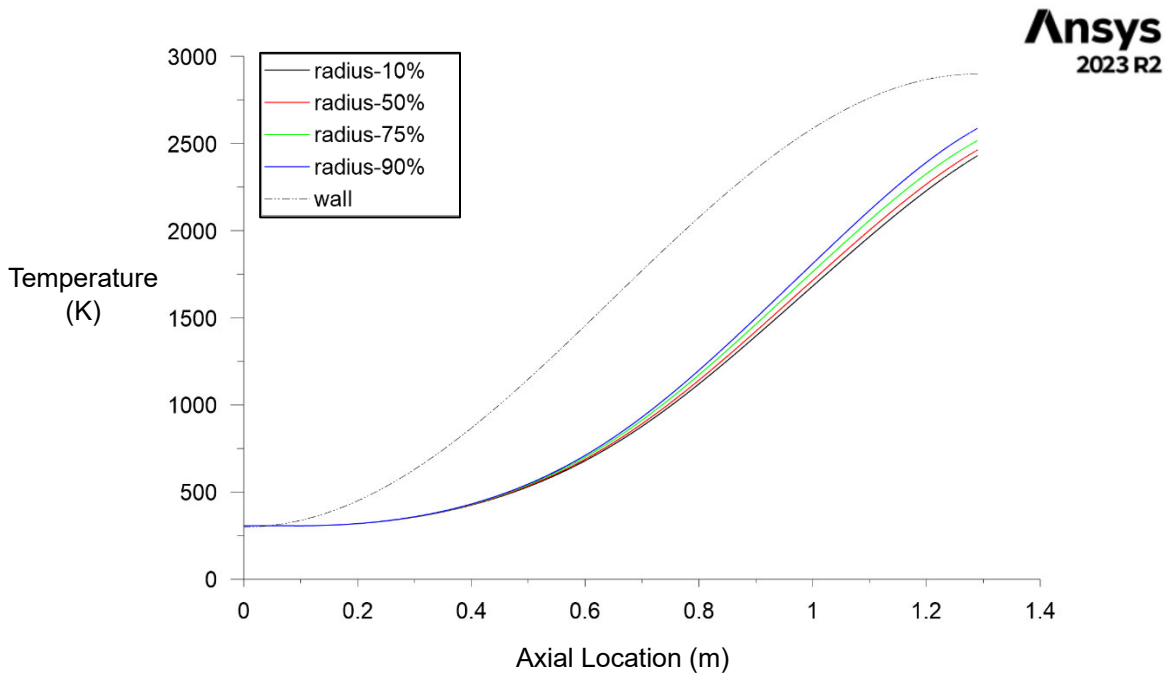


Fig. 22. Plot of total temperature at percentage of circular duct radii

For analysis, equally spaced cross-sectional areas are placed at axial locations in the reactor labeled as “cross-1” through “cross-11” show in Table 7.

Table 7. Cross-section locations for analysis along reactor

	x (m)		x (m)
cross-1	0	cross-7	0.774
cross-2	0.129	cross-8	0.903
cross-3	0.258	cross-9	1.032
cross-4	0.387	cross-10	1.161
cross-5	0.516	cross-11	1.226
cross-6	0.645	Radius: $0 < r < r_{wall}$	

Fig. 23 shows the changing thermal boundary layer profiles at the cross sections. The left axis is a radial measurement from the centerline. Note, cross-11 is not located at the exact outlet of the reactor. The degree of curvature in the thermal profile is evident with increasing temperature. “Cross-7” contains the largest curvature approximately in the center of the reactor at the highest wall temperature gradients. Where the gradients are the lowest, the beginning and end of the reactor, the profiles become more vertical.

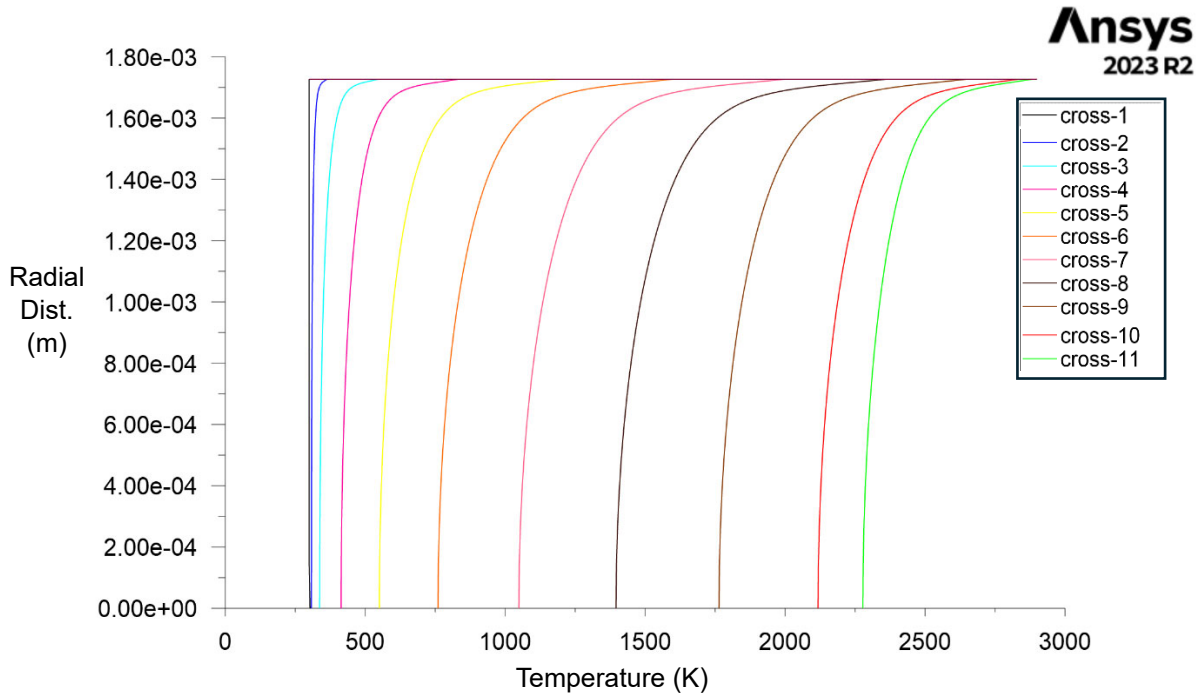


Fig. 23. Thermal boundary profile at selected cross sections along the axis of the reactor. Wall is at a radial distance from centerline of 1.727 mm.

The boundary is essentially vertical near the entry of the reactor but changes shape throughout the reactor as shown in Fig. 24. The centerline reaches 671 m/s leading up to the reactor outlet. The very low viscosity of the hydrogen flow made this subsonic flow have a $Re_D \approx 10^4$ indicating turbulent pipe flow.

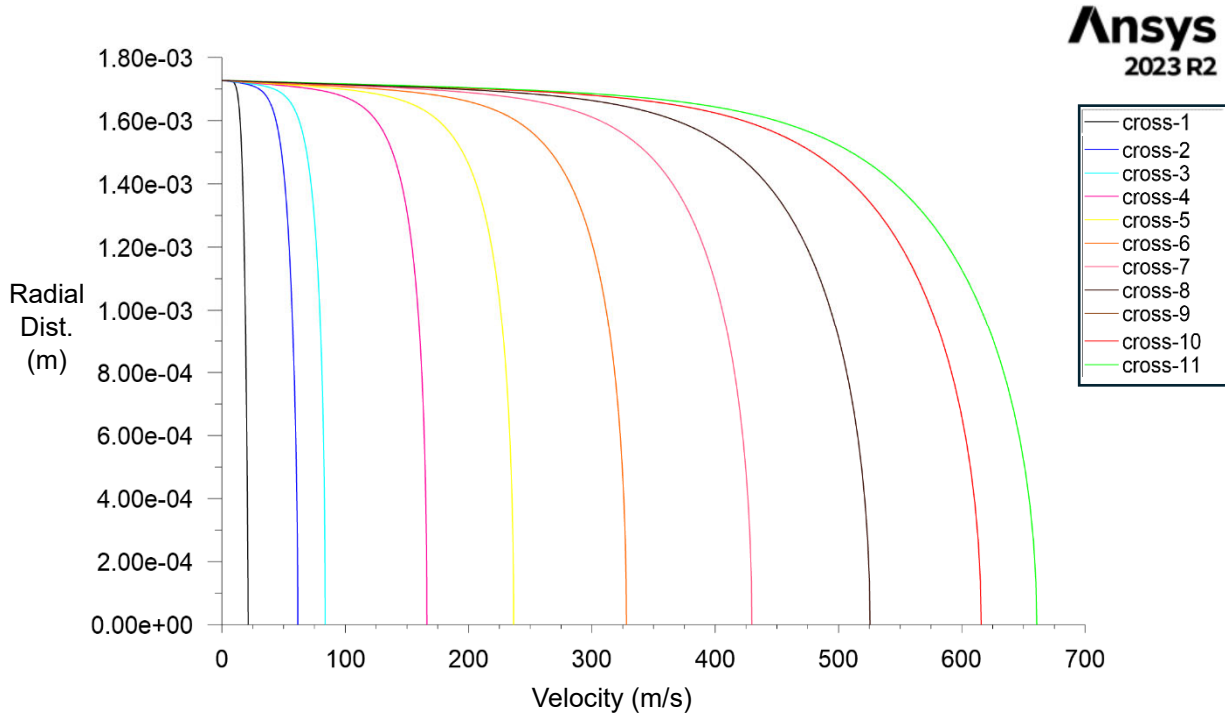


Fig. 24. Turbulent boundary layer profile at selected cross sections along the axis of the reactor. Wall is at a radial distance from centerline of 1.727 mm.

4.3.2 Atomic Hydrogen near Reactor Outlet

Fig. 25 displays the mole fraction of the flow as molecular hydrogen. Near the outlet, the species profile shows an increasing amount of atomic hydrogen closer to the wall.

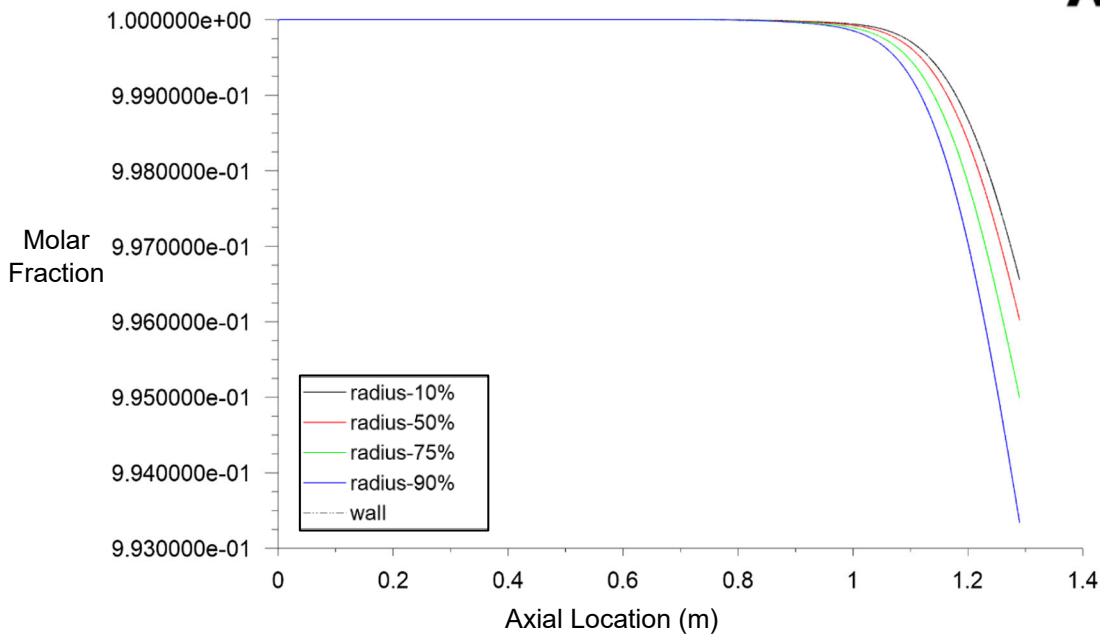


Fig. 25. Molecular hydrogen species molar fraction (X_{H_2}) throughout reactor. Atomic hydrogen species molar fraction is $1 - X_{H_2}$.

Below approximately 1500 K, the amount of atomic hydrogen is insignificant, being virtually all molecular hydrogen. The average mole fraction of hydrogen entering the nozzle is $X_H = 0.48\%$. Comparison to the conclusions in Chapter 2 is described in 4.4.1 below.

4.4 Discussion

4.4.1 Atomic Hydrogen Species Profile

Near the end of the reactor, the atomic hydrogen mole fraction profile becomes very pronounced as shown in Fig 26. Only cross section 8 and above showed any significant atomic hydrogen amount and profile.

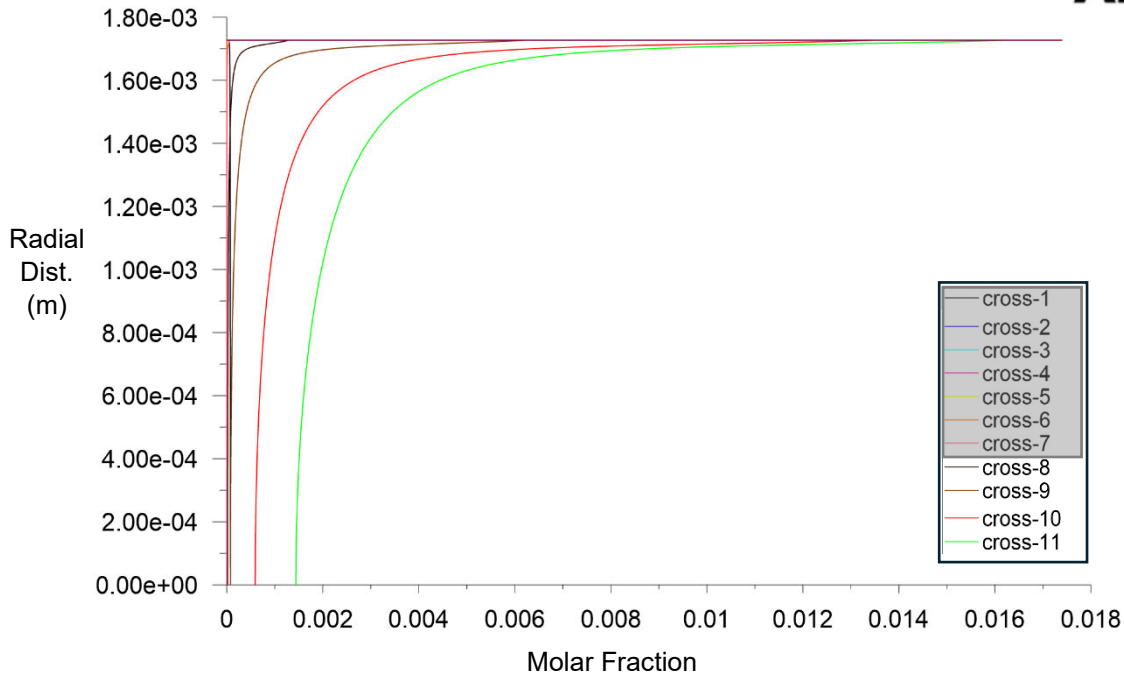


Fig. 26. Atomic hydrogen species profile approaching the chamber

Cross section 11 shows a center-line value of $X_H \approx 0.15\%$ but integrating along the curve shows nearly a two-fold increase when considering the species profile resulting in a $X_{H,avg} \approx 0.29\%$. At maximum, near the wall the flow is nearly 1.8% atomic hydrogen by mole fraction. This is due to the elevated temperatures in the boundary layer near the wall.

This behavior presents a higher value atomic hydrogen species near the outlet than that calculated in Chapter 2 due to the species profile. This analysis validates the center-line values of KIWI 4BE at 0.18% in Chapter 2 but it does highlight the shortfall of assuming equilibrium produces atomic hydrogen concentration based on centerline temperature. This behavior indicates that the boundary layer consideration drives the species roughly twice as high as the centerline

value. For this analysis, this updates the expected species in the KIWI 4BE engine as closer to 0.7% mole fraction of atomic hydrogen.

4.4.2 Total Temperature Remains Relatively Unchanged between the Cases.

KIWI B4E reached a reactor outlet temp of 2330 K while this CFD analysis averaged 2572 K under ideal conditions considering the average temperature profile entering the chamber. If previous KIWI data was reported near centerline, this would only be 4% error. This help explains the elevated atomic hydrogen levels in this analysis, but does not negate the doubling effect.

There is a notable difference in temperature between chemically reacting and non-chemically reacting flows but the effect is largely insignificant. In Chapter 2 it was noted that thermal conductivity can increase greatly due to dissociation. The relatively small amount of atomic hydrogen produced in the boundary layer only slightly enhances the temperature increase while the bulk flow is less impacted. Fig. 27 shows that in the middle of the highest absorption region at cross-9 there is only a 12-degree temperature change between the chemically reacting and non-reacting flows.

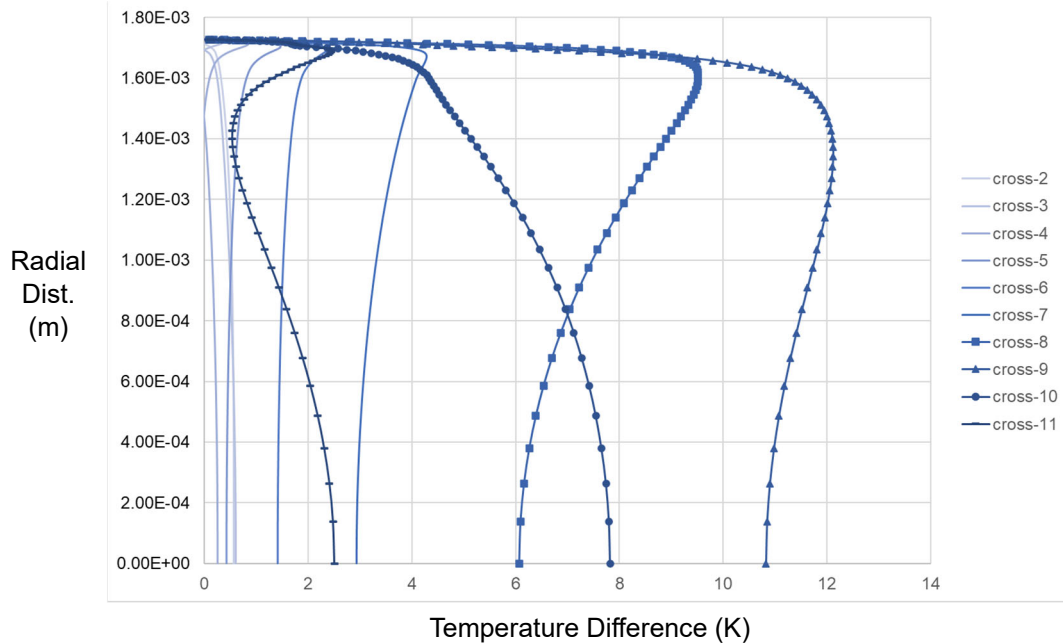


Fig. 27. Temperature difference between non-chemically reacting and chemically reacting flow. Non-Chemically reacting flow was always higher than chemically reacting flow indicated by a positive temperature difference.

All other cross-sections show a much-reduced effect including “cross-11” that is near the outlet. This effect is not surprising as the prediction made by White indicated for small F values the Stanton number will only minimally change as demonstrated in this analysis [104].

The increased temperature difference is also due to the increase in thermal conductivity due the elevated temperatures. Fig 28 shows that for increasing temperatures near the wall the thermal conductivity increases.

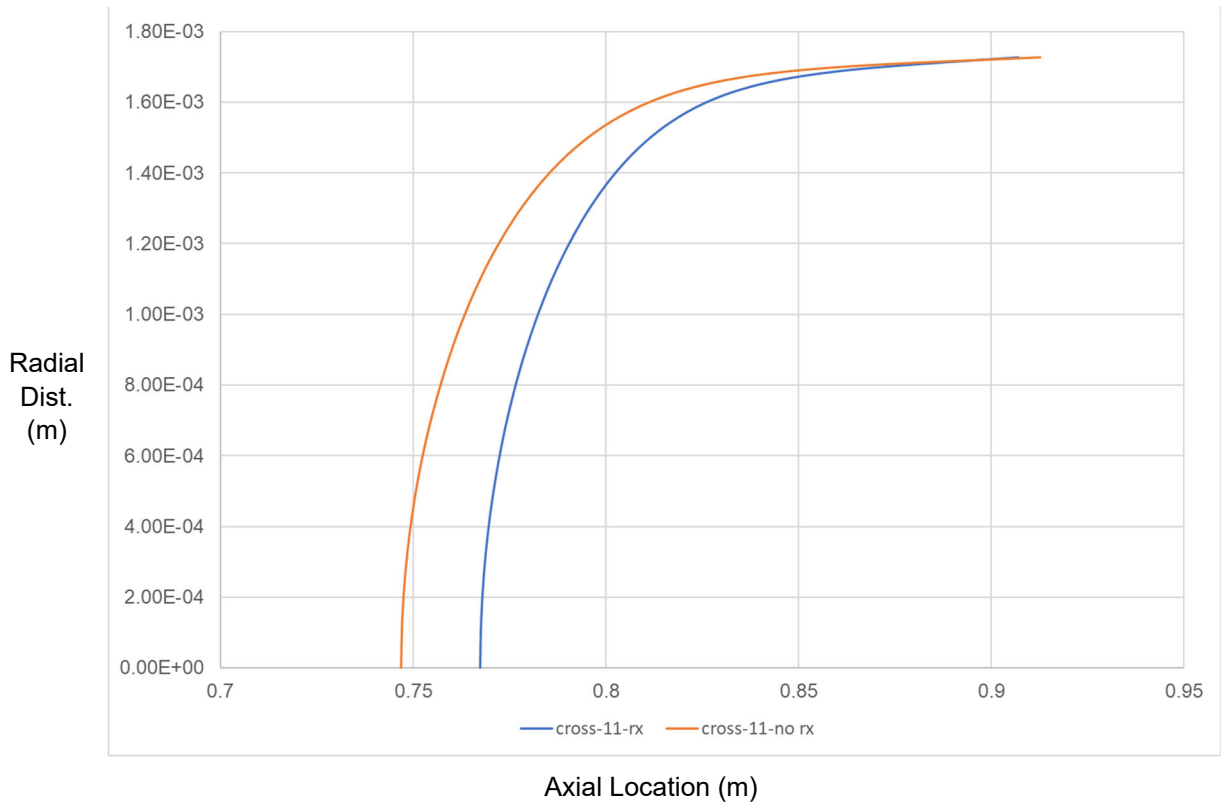


Fig. 28. Increasing thermal conductivity in the boundary layer

4.4.3 Boundary Layer Average Velocity is Reduced from Non-Chemically Reacting Flow

Two effects are evident in the velocity of the flow exiting the reactor. First, the chemically reacting flow is notably reduced in speed from the non-chemically reacting flow. Fig. 29 shows the difference in boundary layers between chemically reacting and non-chemically reacting flows.

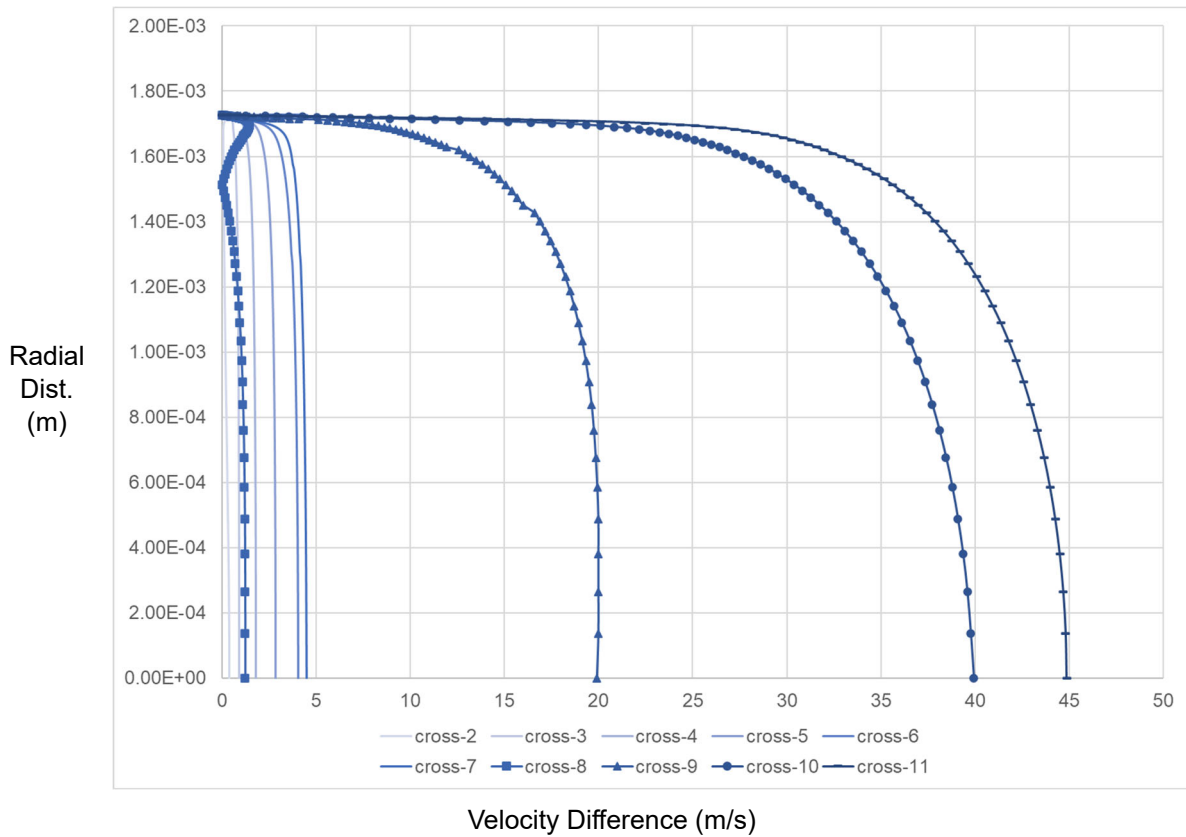


Fig. 29. Velocity difference between non-chemically reacting and chemically reacting flow. Non-Chemically reacting flow was always higher than chemically reacting flow indicated by a positive velocity difference.

At maximum, this only produces a 7% reduction in centerline flow velocity. This is expected due to the mass loss into the walls from the surface reaction and absorption causing the axial flow to slow. Fig. 30 shows the significant radial velocity of the flow with a maximum 110 mm/s with an average of approximately 70 mm/s confirming Chapter 3’s analysis.

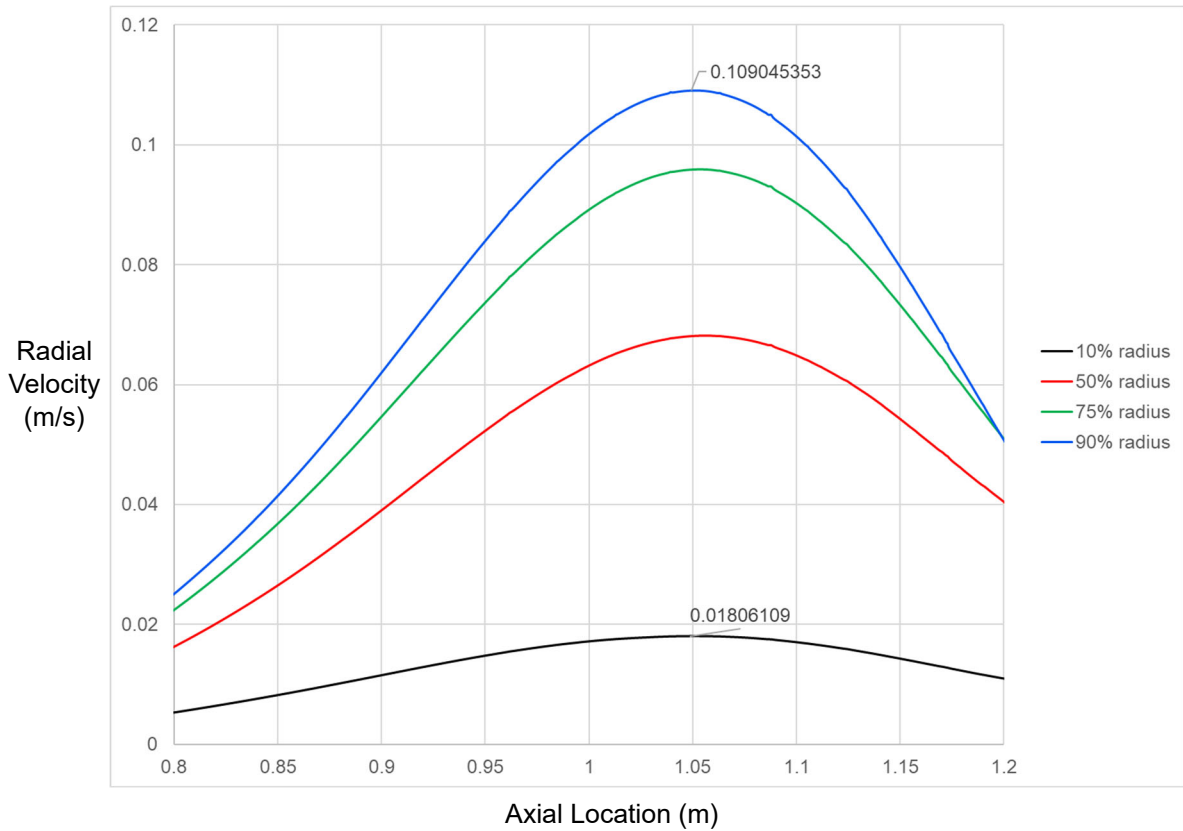


Fig. 30. Radial velocity in the region of significant absorption under chemically reacting flow

There is also a distinct change in the boundary layer profile throughout the reactor through the region of absorption shown in the above figure. Fig. 31 shows a normalized velocity profile of the chemically reacting flow.

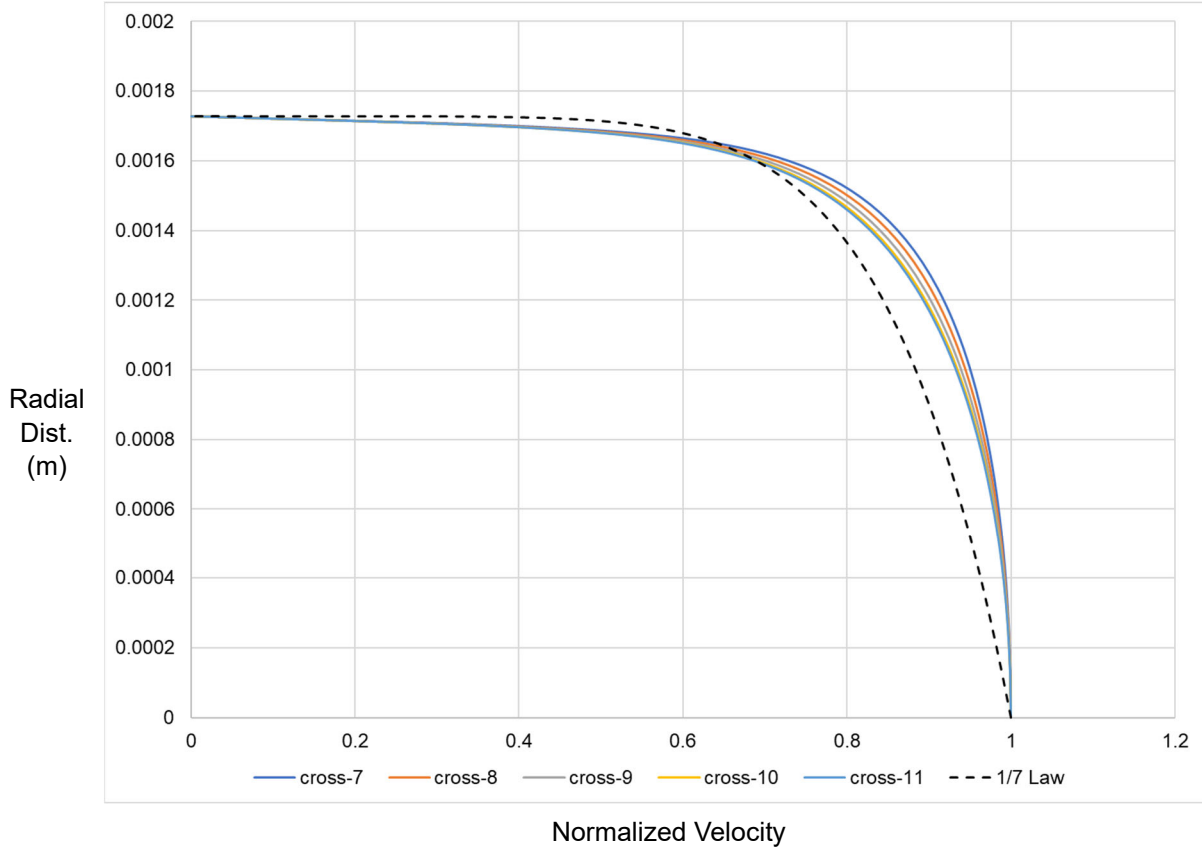


Fig. 31. Comparison of turbulent boundary layer at same locations under chemically reacting flow. Velocity is normalized by V_{max} at centerline flow.

Bird et al. indicate that $10^4 < Re_D < 10^5$ should approximately follow Equation (36) as shown below.

$$\frac{u}{u_{max}} \approx \left(1 - \frac{r}{R}\right)^{\frac{1}{7}} \quad (36)$$

Comparison of this value to the 1/7th approximation shows that the turbulent boundary layer approximation underestimates the velocity profile. By replacing the 7 with a 10, the approximation better approximates the centerline flow, but because more inaccurate near the wall. Additional research is needed here to confirm a turbulence boundary layer model.

4.4.4 ZrC Cladding as a Superior Cladding

Molybdenum-tungsten shows a decreasing performance asking whether better claddings are present. Equation (37) shows the expression for penetration either expressed as Fick's Law of diffusion or through surface coverage.

$$J = D \frac{\partial C}{\partial x} = k_{abs} n = k_{abs} n_T \theta \quad (37)$$

Considering a depth of one layer of atoms, the concentration can be expressed in terms of the surface coverage and the single layer thickness as in Equation (38).

$$\frac{\partial C}{\partial x} \approx \frac{\left(\frac{n_T \theta}{\delta}\right)}{\delta} \quad (38)$$

This provides a comparison to other cladding materials as in Equation (39).

$$k_{abs} = \frac{D}{\delta^2} \quad (39)$$

This relates the hydrogen atom penetrative diffusion values of zirconium carbide (ZrC) and provides a comparison to tungsten mass diffusivity or absorption coefficient varied with temperature which is shown in Fig. 32.

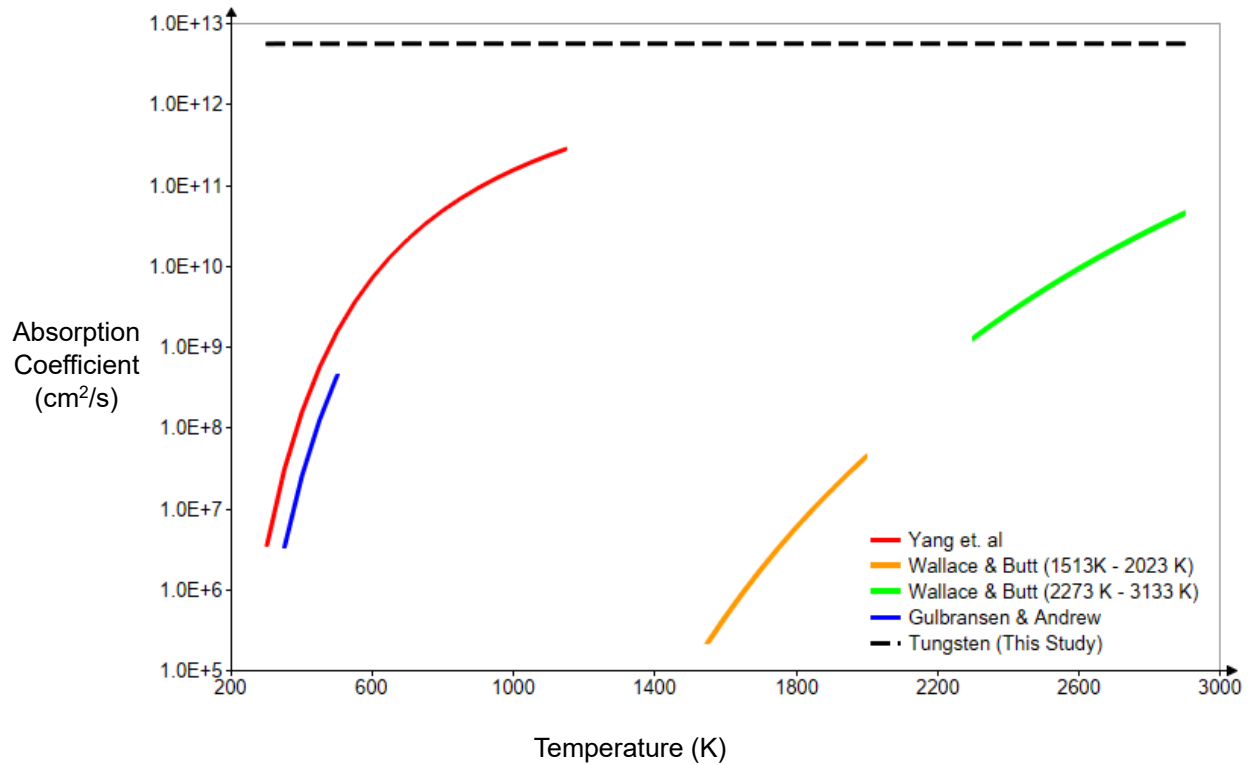


Fig. 32. Absorption coefficient comparison between tungsten cladding (dashed line) versus zirconium cladding as colored lines calculated absorption coefficients from literature [105, 106, 107]

4.4.5 Reactor Channel CFD Performance

Fig. 33 provides an overview of the complete CFD performance of a single reactor channel. The channel length is much greater than the radius denying a complete plot of the channel. Inlet, midsection, and outlet are shown below. The grid and node values are displayed to illustrate the changing cell size approaching the high-speed, high-temperature outlet. Temperature gradients approach wall values and velocity gradients approach zero at the wall. The inlet total pressure contains a slight error of 0.75% that could not be resolved.

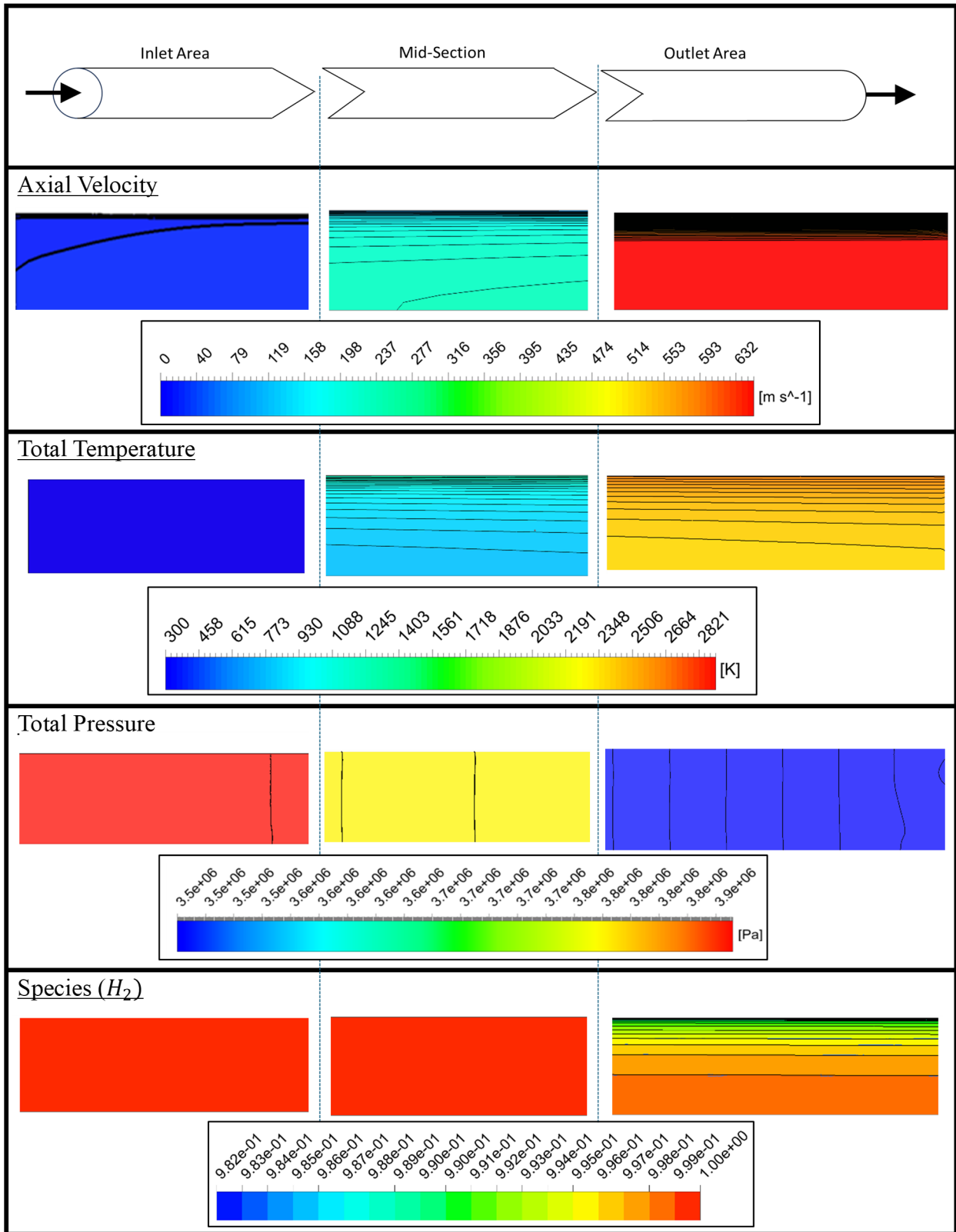


Fig. 33 Reactor channel, chemically reacting, CFD results with increasing grid resolution at inlet, middle, and outlet.

Chapter 5 NTP Rocket Performance with Dissociated Hydrogen Chamber Conditions

5.1 Methods and Measurements

5.1.1 NASA Chemical Equilibrium Analysis (CEA) for Rocket Applications

This analysis uses the National Aeronautics and Space Administration's Chemical Equilibrium Analysis (CEA) code. The program models combustion reactions and converging and diverging nozzle expansion [108]. Options include frozen flow, equilibrium flow, as well as a range of other setting for unique temperature and pressure combustion. The program can calculate the changing chemical equilibrium within the nozzle and report back on a range of values throughout the nozzle. The code contains several assumptions within rocket propulsion that require specific knowledge including combustion chamber velocity, adiabatic chamber conditions, and very specific propulsion and isentropic flow knowledge to correctly operate the application.

5.1.2 Finite Area Combustor Analysis

The CEA was updated to include a finite combustor area option that allows acceleration of flow prior to nozzle expansion. Chambers usually assume a negligible velocity. This feature incorporates an option to assume a flow rate leaving the chamber as opposed to a zero velocity [109]. This feature is critical to the use of CEA as NTP contains no combustion chamber and has a non-trivial subsonic velocity prior to expansion. Fig. 34 shows the basic concept of the finite area option.

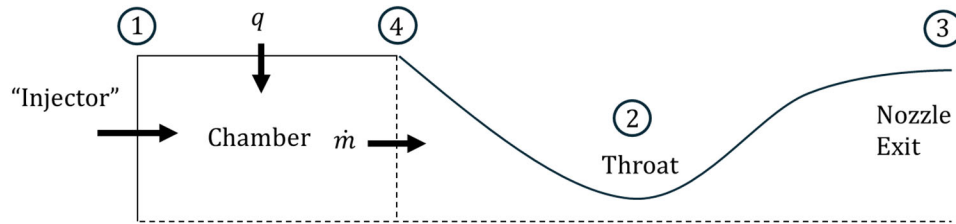


Fig. 34. Notional “combustion chamber” finite area between stations 1 and 4

5.1.3 NTP Property Alignment with Combustor Outlet

NTP engines contain no combustion but do have considerable subsonic velocity flow, high temperature, as well as a difference between stagnation and static pressure departing the chamber. Because there is no injector, combustion, or chamber effect, this requires a careful alignment of the NTP conditions in Chapter 4 to the conditions at chamber station 4. The CEA code takes in several inputs between stations 1 and 4. The CEA code reports back conditions at station 4 prior to expansion. With this approach, the mass flow rate, density, speed, and temperature can be validated at station 4 for confident use of CEA though NTP has no combustion chamber.

5.2 Theory

NTP achieves maximum specific impulse by maximizing chamber temperature while minimizing propellant molecular weight. The concept of specific impulse is outlined in Chapter 4.

5.2.1 Non-chemically Reacting Flow versus Chemically Reacting Equilibrium and Frozen Flow

Three cases will be generated for the nozzle: a non-chemically reacting solution and two chemically reacting flow solutions: a frozen flow solution and an equilibrium chemically reacting flow solution. The accepted chemically reacting solution will fall between the bounding conditions of frozen flow and equilibrium chemically reacting flow.

Frozen flow assumes no chemical reactions and should produce the lowest temperature at the nozzle exit. There is no dissociation nor recombination under this case and therefore produces no exothermic energy in the nozzle. Equilibrium chemically reacting flow is expected to produce a higher exit temperature than frozen flow. As the flow experiences the decreasing pressure and temperature of isentropic expansion, atomic hydrogen will recombine in the nozzle. This exothermic energy release should occur continually from chamber to nozzle exit. Because of this, the flow will receive more energy as it expands providing additional thermal energy to the flow. In fact, this equilibrium case provides the highest possible energy transfer to the flow from chemical reactions.

The diverging section of the nozzle will contain supersonic flow with similar timescales between control-volume residence time and chemical reaction time. This will establish the flow as a non-equilibrium chemically reacting flow within the control volumes. Because it is non-equilibrium, less atomic hydrogen will recombine in each control volume and release less exothermic energy to the flow than in the equilibrium case. This places the numerical solution for exit temperature below the equilibrium case but above the frozen flow case.

Separately, due to the decreasing temperature from chamber to exit, the equilibrium constant will continually decrease reducing the quantity of atomic hydrogen. The equilibrium constant provides a ratio of atomic hydrogen to molecular hydrogen and is a function of temperature alone. As the flow decreases in temperature, equilibrium states that this ratio should also decrease. Therefore, a general trend of decreasing atomic hydrogen levels should occur between chamber and exit for all cases.

5.2.2 Nozzle Expansion is Isentropic with Chemical Reactions

All channels, including boundary layer and bulk flow, are culminated in one representative chamber condition prior to isentropic expansion in a de Laval nozzle. Equation (40) shows the isentropic compressible flow equation that describes the one-dimensional flow conditions from chamber to nozzle expansion. No chemical interactions are considered in the nozzle in frozen flow.

$$\frac{P_0}{P} = \left(1 + \frac{\gamma - 1}{2} M^2\right)^{\frac{\gamma}{\gamma - 1}} \text{ where } P = \rho RT \quad (40)$$

Equation (40) assumes a calorically perfect gas. That is a constant specific heat ratio from chamber to exit and that there are no chemical reactions. However, if chemical reactions are assumed, then the flow is neither calorically perfect nor thermally perfect. This means that both internal energy and enthalpy must be functions of temperature and pressure.

However, chemically reacting flow can be isentropic if the flow is able to reach equilibrium within the control volume as mentioned earlier. The combined first and second law of thermodynamics are shown in Equation (41).

$$Tds = dh - vdp \quad (41)$$

The governing equations for quasi-one-dimensional flow are shown in Equation (42).

$$dh + udu = 0 \quad (42)$$

Additionally, the momentum equation is shown in Equation (43).

$$dp = -\rho u du \quad (43)$$

Combining Equations (41) through (43) gives Equation (44) as shown below that demonstrates that equilibrium chemically reacting flows are indeed isentropic.

$$Tds = 0 \quad (44)$$

Therefore, as mentioned above, if the chemical reactions are considered much faster than the time it takes for the flow to travel the control volume, equilibrium chemical reactions can be calculated.

Finally, to calculate one-dimensional flow, the equilibrium chemically reacting gas now becomes a function of stagnation conditions and velocity as in Equation (45) and no longer a property of Mach number. To solve, a numerical integration of the 1-D continuity, momentum, and energy equations are required while varying thermodynamic properties at each step considering species mixture, temperature, and chemical reactions.

$$\frac{A}{A^*} = f_1(P_0, T_0, u), \quad \frac{T}{T_0} = f_2(P_0, T_0, u), \quad \frac{P}{P_0} = f_3(P_0, T_0, u) \quad (45)$$

5.3 Results

5.3.1 Specific Impulse

The specific impulse was found to be $I_{sp} = 8772 \frac{m}{s}$ for the chemically reacting equilibrium flow. See Table 7 for complete calculations from “combustor” station 4 through supersonic expander exit.

Table 8. CEA calculations at throat and supersonic expander exit for KIWI B4E with chemically reacting flow

CEA Analysis*	Combustor End	Throat	Exit
Temperature (K)	2576.28	2269.63	292.42
Density (kg/m ³)	3.5261E-01	2.2331E-01	9.0073E-04
C_p (kJ/kg·K)	20.5616	18.5315	14.2838
γ	1.2692	1.2940	1.4060
a_e (m/s)	3677.6	3482.0	1302.2
M	0.174	1.00	6.629
I_{sp} (m/s) (Vacuum)			8772.2

* NASA-Glenn Chemical Equilibrium Program CEA 2, February 5, 2004 By Bonnie McBride and Sanford Gordon, Refs: NASA RP-1311, Part I, 1994 & NASA RP-1311, Part II, 1996

The chemically reacting frozen flow was $I_{sp} = 8769 \frac{m}{s}$. For both these cases, the initial species was $X_H = 0.7\%$. Due to this very small window, the non-equilibrium case was not directly calculated as it was expected to lie between these values. This is further explored below. The non-chemically reacting flow throughout the reactor and nozzle had an $I_{sp} = 8695 \frac{m}{s}$. The non-chemically reacting case assumed a 100% mole fraction of molecular hydrogen.

5.3.2 Atomic Hydrogen Recombination in Nozzle

Decreasing temperature and pressure in the converging section of the nozzle showed a decrease in molar fraction of atomic hydrogen. The atomic hydrogen dropped from $X_H = 0.57\%$ at the chamber inlet to $X_H = 0.18\%$ at the nozzle throat. Further recombination drove the atomic hydrogen to $X_H \approx 0\%$ at the nozzle exit. Complete recombination of the atomic hydrogen to molecular hydrogen occurred between the nozzle throat and the nozzle exit.

5.4 Discussion

5.4.1 Specific Impulse Increase in Efficiency

The specific impulse increased a small amount by 0.9% between the assumption of chemically reacting flow and non-chemically reacting flow. Equilibrium and frozen flow both showed very similar values due to the small amount of atomic hydrogen in the converging-diverging nozzle. However, the small amount of atomic hydrogen in the equilibrium flow effectively generated a lighter propellant by containing a percentage of lighter dissociated molecules as opposed to the heavier 100% molecular hydrogen.

This small effect is unsurprising compared to, the extremely minimal, historic work on dissociation. Stubbs et al. noted that unless chamber temperatures were well above 2700 K, or chamber pressures were drastically reduced, the dissociation effect is relatively insignificant [110].

5.4.2 Superiority of Specific Impulse to Liquid Engines

The values for specific impulse are nearly twice as efficient as modern liquid engines and approach the theoretical limit for solid-core NTP. The LE-5A Liquid Engine is cited as having one of the highest specific impulse at $I_{sp} = 4434 \frac{m}{s}$ [111]. This analysis shows that performance of the KIWI 4BE engine is a 98% performance increase over the best liquid engine. The KIWI is within 9.6% of the reported theoretical limit of solid core NTP of $I_{sp} = 9600 \frac{m}{s}$ considering the melting point of cladding and fuel materials [112].

Chapter 6 Conclusions and Future Works

Hydrogen dissociation is largely ignored in NTP research. Pinpointing chamber conditions including temperature, velocity, and atomic hydrogen species is critical to identifying performance. Ignoring volumetric and surface Reactions in NTP propulsion modeling overestimates the temperature and velocity profile entering a chamber region prior to expansion. However, dissociation causes a net minimal increase in the final rocket performance.

All historic reactor inlet conditions can be assumed to be at equilibrium for atomic hydrogen values at, or below, 1% and remain at equilibrium until approximately 1600 K. Beyond this temperature, all reactors operated in non-equilibrium, with one reactor operating as low as 51% of equilibrium but converged toward equilibrium at the outlet. All historic NTP reactors correlated with equilibrium at reactor outlet within 82%. Hydrogen dissociation is present in all historic NTP reactors, but all atomic hydrogen levels were below 0.5% molar fraction of total concentration when considering bulk flow temperatures in the reactor.

Historic reactors demonstrate that similar NTP systems must consider non-equilibrium near the outlet above 1600 K as well as if the flow is disrupted from trace amounts below 1600 K. Highest core exit temperatures contains the highest dissociated atomic hydrogen while highest operating pressures cause the reactor to closely follow equilibrium. Reactor inlets that contain less than 1% molar fraction atomic hydrogen can be assumed to reach equilibrium by the reactor outlet.

Additionally, the cross-flow velocity was determined by calculating the absorption rate of hydrogen into NTP cladding materials. This demonstrated that the fluid mechanics of NTP reactors must consider the surface reaction of dissociated hydrogen flow in design and optimization of NTP engines. NTP reactors contain a notable crossflow velocity near the reactor outlet due to the absorption of hydrogen into the NTP cladding material. Tungsten is selected as the cladding of

choice due to concerning indications of high hydrogen penetration rates in molybdenum-tungsten alloy. Zirconium carbide was rejected due its historic issues with mass loss and chemical reaction but proves to be a promising future candidate. The velocity profile has a notable decelerating effect from a crossflow velocity as high as 80 mm/s into NTP cladding resembling a form of wall suction. The absorption of hydrogen has a small effect on the thermal boundary layer. Flat-plate wall suction flow calculations indicate possible regions of backflow requiring further CFD analysis. This study is limited by the approximation of the adsorption sticking coefficient from the literature survey and would benefit from direct experimental testing. The following CFD would look closely at the boundary layer effects, assuming wall transpiration of hydrogen and provide the most accurate velocity and mass flow rates exiting the reactor and entering the chamber. Future research should closely generate adsorption, desorption, and absorption surface reaction models for molybdenum-tungsten alloy to best capture the current engine design efforts.

A 2-D axisymmetric computational fluid dynamics (CFD) model of the KIWI 4BE nuclear reactor provided the highest quality of chamber conditions for NTP. Atomic hydrogen was found to double over previous assumptions in Chapter 2 with an acceptable value of 0.7% molar fraction of atomic hydrogen entering the NTP “Chamber” accompanied by a significant velocity decrement of 7% less when considering chemical reactions. Thermal boundary layer profiles and hydraulic boundary layers change under the conditions of chemical reaction. The thermal boundary layer changes appear relatively insignificant while the “1/7th” turbulent velocity profile was not accurate and needs further update. Analysis of zirconium carbide indicated that hydrogen absorption maybe greatly suppressed but further operational conditions are needed for testing. Further computations were completed in 1-D rocket nozzle expansion to fully understand the performance effect.

The culmination of thousands of NTP channels provides a chamber condition for nozzle expansion and rocket thrust. Calculation of the changing atomic hydrogen level requires a chemical analysis throughout nozzle expansion. NASA Chemical Equilibrium Analysis Application provides the tools to complete this analysis. The specific impulse is found for the chemically reacting flow and non-chemically reacting low cases and compared. The specific impulse demonstrates the superior efficiency of the KIWI B4E engine over liquid engines. Consideration of chemically reacting flow provides a slight increase in efficiency of 0.9% over the assumption of non-chemically reacting flow. Modeling of NTP engines will underestimate the performance if chemically reacting flow is not considered.

Future works should explore the efficiency increase of NTP engines due to dissociated hydrogen while avoiding detrimental effects of decreased thermal hydraulic performance and cladding melting points. The increased efficiency due to a lighter propellant with decreased hydraulic performance is an interesting optimization problem. The molar fraction of atomic hydrogen will continue to rise as NTP flow temperatures approach the cladding material melting point above 2900 K. Expectations are that the thermal hydraulic performance will fall. The optimization of this performance tradeoff must be analyzed for any performance effects that become dominant. Overall, a theoretical limit of the performance increase should be investigated and calculated that would divide solid core from liquid core NTP. This should be accomplished under a complete three-dimensional CFD model and include chamber culminating sections and supersonic expansion. At increased atomic hydrogen levels new analysis is required to better understand the wall absorption from atomic hydrogen.

References

- [1] Finseth, J L. Rover nuclear rocket engine program: Overview of rover engine tests. Final Report. United States: N., 1991. Web. OSTI Identifier: 5857913 p. 3, 10, 53-57, 54-55, 58, C-1. <https://www.osti.gov/biblio/5857913>
- [2] Angelo, Joseph A, and David Buden. Space Nuclear Power. Original ed., Orbit Book Co., 1985. pp. 177-178, 182, 184
- [3] The thermal conductivity of 10% molar fraction dissociated hydrogen gas is more than 6 times higher in thermal conductivity than an assumption of non-chemically reacting gas (i.e. 0% Molar Fraction).
- [4] Hanley, H.J.M., et al. "The Viscosity and Thermal Conductivity of Dilute Gaseous Hydrogen from 15 to 5000 K." Journal of Research of the National Bureau of Standards. Section A. Physics and Chemistry, vol. 74A, no. 3, 1970, pp. 341, 344. <https://doi.org/10.6028/jres.074A.029>
- [5] Finseth, J L. Rover nuclear rocket engine program: Overview of rover engine tests. Final Report. United States: N., 1991. Web. OSTI Identifier: 5857913 p. 3, 10, 53-57, 54-55, 58, C-1. <https://www.osti.gov/biblio/5857913>
- [6] Ward C. Roman, W., Hermanson, J., Hay, S., Breen, J.; Diagnostic Techniques for Hot Hydrogen Testing of Materials for SNTF. AIP Conference Proceedings 1 July 1994; 301 (1): pp. 920. <https://doi.org/10.1063/1.2950289>
- [7] El-Genk, M.S., et al. "Pellet Bed Reactor for Nuclear Thermal Propelled Vehicles. [BeO; B₄C; ZrC; TaC]." AIP Conference Proceedings (American Institute of Physics); (United States), vol. 217:2, 1991, pp. 616. <https://doi-org.ezproxy.library.unlv.edu/10.1063/1.40113>
- [8] Davis, J., Mills, J., Glass, J., Tu, W.; Advanced NTR options. AIP Conference Proceedings 5 January 1991; 217 (2): 749-750. <https://doi.org/10.1063/1.40135>
- [9] Stubbs, R.M., et al. "Analysis of Nuclear Thermal Propulsion Systems Using Computational Fluid Dynamics." AIP Conference Proceedings (American Institute of Physics); (United States),

vol. 271:3, 1993, pp. AIP Conference Proceedings (American Institute of Physics); (United States), 1993, Vol.271:3. <https://doi.org/10.1063/1.43055>

[10] Fang, Yuliang, et al. "Study on High-Temperature Hydrogen Dissociation for Nuclear Thermal Propulsion Reactor." *Nuclear Engineering and Design*, vol. 392, 2022, pp. 4. <https://doi.org/10.1016/j.nucengdes.2022.111753>

[11] Krecicki, M., et al. "Thermal Hydraulic Modeling of Solid Fueled Nuclear Thermal Propulsion Reactors Part I: Development and Verification." *Annals of Nuclear Energy*, vol. 173, 2022, pp. 11. <https://doi.org/10.1016/j.anucene.2022.109113>

[12] Angelo, J. A., & Buden, D. (1985). *Space nuclear power (Original ed.)*. Orbit Book Co. 184.

[13] Malefant, R. et al. "Nuclear Thermal Rocket Reactors and Engine Systems: A Retrospective," G.T. Seaborg Institute of Transactinium Science, Los Alamos National Laboratory, 2021 pp. 5

[14] Heinola, K., & Ahlgren, T. (2010). First-principles study of H on the reconstructed W(100) surface. *Physical Review. B, Condensed Matter and Materials Physics*, 81(7). pg. 1-3 <https://doi.org/10.1103/PhysRevB.81.073409>

[15] Moore, G., & Unterwald, F. (1964). Thermal dissociation of hydrogen. *The Journal of Chemical Physics*, 40(9), pg. 2639

[16] P. W. Tamm, L. D. Schmidt; Binding States of Hydrogen on Tungsten. *J. Chem. Phys.* 1 June 1971; 54 (11): pg. 4778

[17] Alnot, P., Cassuto, A., & King, D. (1989). Adsorption and desorption kinetics with no precursor trapping: Hydrogen and deuterium on W {100}. *Surface Science*, 215(1), pg. 29-46.

[18] Smith, A., Barker, R., & Estrup, P. (1984). Desorption of hydrogen from tungsten (100). *Surface Science*, 136(2), pg. 327-344.

[19] Guterl, J., Smirnov, R., Krashennnikov, S., Uberuaga, B., Voter, A., & Perez, D. (2015). Modeling of hydrogen desorption from tungsten surface. *Journal of Nuclear Materials*, 463, pg. 263-264.

[20] Frauenfelder, R. (1968). Permeation of hydrogen through tungsten and molybdenum. *The Journal of Chemical Physics*, 48(9), pg. 3955

[21] Liu, Changsong, "Retention and diffusion of hydrogen in tungsten: effects of temperature, alloying elements and vacancy clusters," Key Laboratory of Materials Physics, Institute of Solid State Physics, Chinese Academy of Sciences, Hefei, PR China pg. 15

[22] Guterl, J., Smirnov, R. D., & Snyder, P. (2019). Effects of surface processes on hydrogen outgassing from metal in desorption experiments. *Nuclear Fusion*, 59(9), 96042. pg. 4
<https://doi.org/10.1088/1741-4326/ab280a>

[23] Ibid.

[24] Henriksson, K. O. E., Vörtler, K., Dreißigacker, S., Nordlund, K., & Keinonen, J. (2006). Sticking of atomic hydrogen on the tungsten (0 0 1) surface. *Surface Science*, 600(16), 3174.
<https://doi.org/10.1016/j.susc.2006.06.001>

[25] Zheng, W., & Gallagher, A. (2006). Hydrogen dissociation on high-temperature tungsten. *Surface Science*, 600(10), 2210. <https://doi.org/10.1016/j.susc.2006.03.032>

[26] Guterl, J., Smirnov, R. D., & Snyder, P. (2019). Effects of surface processes on hydrogen outgassing from metal in desorption experiments. *Nuclear Fusion*, 59(9), 96042.
<https://doi.org/10.1088/1741-4326/ab280a>

[27] Alnot, P., Cassuto, A., & King, D. (1989). Adsorption and desorption kinetics with no precursor trapping: Hydrogen and deuterium on W {100}. *Surface Science*, 215(1), pg. 29-46.

[28] Emrich, Jr., William J. (2016). Principles of Nuclear Rocket Propulsion. In *Principles of Nuclear Rocket Propulsion*. Elsevier Science & Technology. pg. 132, 137

[29] Gorrell, A., Morris, M., & Chen, Y.-T. (2023). Non-Equilibrium behavior of dissociated hydrogen in historic Nuclear thermal propulsion reactors. *Nuclear Engineering and Design*, 413, 112494., 6. <https://doi.org/10.1016/j.nucengdes.2023.112494>

[30] Johnson, D. F., & Carter, E. A. (2010). Hydrogen in tungsten: Absorption, diffusion, vacancy trapping, and decohesion. *Journal of Materials Research*, 25(2), 316. <https://doi.org/10.1557/JMR.2010.0036>

[31] Gorrell, A., Morris, M., & Chen, Y.-T. (2023). Non-Equilibrium behavior of dissociated hydrogen in historic Nuclear thermal propulsion reactors. *Nuclear Engineering and Design*, 413, 112494., 6. <https://doi.org/10.1016/j.nucengdes.2023.112494>.

[32] Ultra Safe Nuclear, NTP Engines, <https://www.usnc.com/ntp/>

[33] Chen, W., Wei, T., Wang, D., & Zhao, Y. (2022). Effect of Elemental Doping on the Adsorption Behavior and the Mechanism of Hydrogen Adsorption on the Zirconium Surface. *Journal of Physical Chemistry. C*, 126(37), 15945. <https://doi.org/10.1021/acs.jpcc.2c03661>

[34] Storms, E., “The behavior of $ZrC(1-x)$ and $U(y)Zr(1-y)C(1-x)$ in flowing hydrogen at very high temperatures”, 22. bzuz.rept, 1992. <https://ui.adsabs.harvard.edu/abs/1992bzuz.rept.....S/abstract>

[35] Wallace, T. C. (1991). Review of Rover fuel element protective coating development at Los Alamos. *AIP Conference Proceedings (American Institute of Physics); (United States)*, 217:3. 1028. <https://doi.org/10.1063/1.40061>

[36] Wang, X., Xu, C., Hu, S., Zhang, H., Zhou, X., & Peng, S. (2019). The structure stability, diffusion behavior and elastic properties of stoichiometric ZrC bulk with interstitial hydrogen defect: A first-principles study. *Journal of Nuclear Materials*, 521, 146–154. <https://doi.org/10.1016/j.jnucmat.2019.04.041>

[37] Oyama, S. T. (1996). *The Chemistry of Transition Metal Carbides and Nitrides* (1st ed. 1996.). Springer Netherlands : Imprint: Springer. 58

[38] Wang, X., Xu, C., Hu, S., Zhang, H., Zhou, X., & Peng, S. (2019). The structure stability, diffusion behavior and elastic properties of stoichiometric ZrC bulk with interstitial hydrogen defect: A first-principles study. *Journal of Nuclear Materials*, 521, 153.
<https://doi.org/10.1016/j.jnucmat.2019.04.041>

[39] Sutton, G. P., & Biblarz, O. (2017). *Rocket propulsion elements* (Ninth edition.). 52. Wiley.

[40] Emrich, J., William J. (2023). *Principles of nuclear rocket propulsion* (Second edition..). Butterworth-Heinemann. 15

[41] Krecicki, M., & Kotlyar, D. (2020). Low enriched nuclear thermal propulsion neutronic, thermal hydraulic, and system design space analysis. *Nuclear Engineering and Design*, 363, 110605. Pg. 2 <https://doi.org/10.1016/j.nucengdes.2020.110605>

[42] Anderson, J. D. *Modern Compressible Flow: With Historical Perspective*. McGraw-Hill. (2003) pg. 646

[43] Vamos, J., & Anderson, J. (1973). Time-Dependent Analysis of Nonequilibrium Nozzle Flows with Complex Chemistry. *Journal of Spacecraft and Rockets*, 10(4), 225-226.

[44] Moeller, Trevor, et al. "Studies of Nonequilibrium Hydrogen/Nitrogen Plasmas Using a Cascade Arc." *AIP Conference Proceedings*, vol. 387, no. 1, 1997, pp. AIP conference proceedings, 1997, Vol.387 (1). pp. 318 <https://doi.org/10.1063/1.52009>

[45] NIST Chemistry Webbook, "Hydrogen Atom, $e^- + H^+ = H$ " Gibbs Free Energy of Formation, <https://webbook.nist.gov/cgi/cbook.cgi?ID=C12385136&Mask=6FF>

[46] Nguyen, Ngo, "Elementary Reactions," LibreTexts™ Chemistry, 2023

[https://chem.libretexts.org/Bookshelves/Physical_and_Theoretical_Chemistry_Textbook_Maps/Supplemental_Modules_\(Physical_and_Theoretical_Chemistry\)/Kinetics/03%3A_Rate_Laws/3.02%3A_Reaction_Mechanisms/3.2.01%3A_Elementary_Reactions#:~:text=An%20elementary%20reaction%20is%20a,transition%20state%20and%20no%20intermediates.](https://chem.libretexts.org/Bookshelves/Physical_and_Theoretical_Chemistry_Textbook_Maps/Supplemental_Modules_(Physical_and_Theoretical_Chemistry)/Kinetics/03%3A_Rate_Laws/3.02%3A_Reaction_Mechanisms/3.2.01%3A_Elementary_Reactions#:~:text=An%20elementary%20reaction%20is%20a,transition%20state%20and%20no%20intermediates.)

[47] McCay, T. Dwayne, and Carol E Dexter. "Chemical Kinetic Performance Losses for a Hydrogen Laser Thermal Thruster." *Journal of Spacecraft and Rockets*, vol. 24, no. 4, 1987, pp. 373, 376. <https://doi.org/10.2514/3.25927>

[48] Baulch, D. L., et al. "Evaluated Kinetic Data for Combustion Modeling: Supplement II." *Journal of Physical and Chemical Reference Data*, vol. 34, no. 3, 2005, pp. 761, 905, 909, <https://doi.org/10.1063/1.1748524>

[49] Kim, Suk C, and Robert M Stubbs. "Numerical Study of Low-Pressure Concept for Nuclear Thermal Rockets." *Journal of Propulsion and Power*, vol. 10, no. 1, 1994, pp. 27. <https://doi.org/10.2514/3.23707>

[50] Baulch, D. L., et al. "Evaluated Kinetic Data for Combustion Modeling: Supplement II." *Journal of Physical and Chemical Reference Data*, vol. 34, no. 3, 2005, pp. 761, 905, 909, <https://doi.org/10.1063/1.1748524>

[51] Cohen, N., and K. R. Westberg. "Chemical Kinetic Data Sheets for High-Temperature Chemical Reactions." *Journal of Physical and Chemical Reference Data*, vol. 12, no. 3, 1983, pp. 559-560. <https://doi.org/10.1063/1.555692>

[52] Chapter by Jürgen Warnatz; Burcat, A, et al. "Rate Coefficients in the C/H/O System." *Combustion Chemistry*, Springer New York, United States, 1984, pp. 215,

[53] Baulch, D. L., et al. "Evaluated Kinetic Data for Combustion Modeling: Supplement II." *Journal of Physical and Chemical Reference Data*, vol. 34, no. 3, 2005, pp. 761, 905, 909, <https://doi.org/10.1063/1.1748524>

[54] D. R. Stull and H. Prophet, *JANAF Thermochemical Tables*, 2nd ed., NSRDS-NBS 37, N.B.S., Washington D.C., 1971, M. W. Chase, C. A. Davies, J. R. Downey, D. J. Frurip, R. A. McDonald, and A. N. Syverud, *J. Phys. Chem. Ref. Data* 14, Supplement 1, 1985

[55] Anderson, J. D. *Modern Compressible Flow: With Historical Perspective*. McGraw-Hill. (2003) pp. 629, 664-666

[56] Hanley, H.J.M., et al. “The Viscosity and Thermal Conductivity of Dilute Gaseous Hydrogen from 15 to 5000 K.” *Journal of Research of the National Bureau of Standards. Section A. Physics and Chemistry*, vol. 74A, no. 3, 1970, pp. 341, 344.
<https://doi.org/10.6028/jres.074A.029>

[57] Stiel, L. I, and George Thodos. “Viscosity of Hydrogen in Gaseous and Liquid States for Temperatures Up to 5000° K.” *Industrial & Engineering Chemistry Fundamentals*, vol. 2, no. 3, 1963, pp. 234–235. <https://doi.org/10.1021/i160007a014>

[58] White, Frank Mangrem. *Viscous Fluid Flow*. McGraw-Hill, 1974. Pp. 415, 426 (Fig 6-8)

[59] Finseth, J L. Rover nuclear rocket engine program: Overview of rover engine tests. Final Report. United States: N., 1991. Web. OSTI Identifier: 5857913 p. 3, 10, 53-57, 54-55, 58, C-1.
<https://www.osti.gov/biblio/5857913>

[60] Ibid.

[61] Anderson, J. D. *Modern Compressible Flow: With Historical Perspective*. McGraw-Hill. (2003) pp. 629, 664-666

[62] Kubin, R.F. and Presley, L.L., “Thermodynamic Properties and Mollier Chart for Hydrogen from 300° K to 20,000° K,” NASA Case File, Ames Research Center, 1964, pp. 48.
<https://ntrs.nasa.gov/citations/19640008593>

[63] Ibid.

[64] Angelo, J. A., & Buden, D. (1985). *Space nuclear power (Original ed.)*. Orbit Book Co. 184.

[65] Krecicki, M., et al. “Thermal Hydraulic Modeling of Solid Fueled Nuclear Thermal Propulsion Reactors Part I: Development and Verification.” *Annals of Nuclear Energy*, vol. 173, 2022, pp. 11. <https://doi.org/10.1016/j.anucene.2022.109113>

[66] Angelo, J. A., & Buden, D. (1985). Space nuclear power (Original ed.). Orbit Book Co. 184.

[67] Henriksson, K. O. E., Vörtler, K., Dreißigacker, S., Nordlund, K., & Keinonen, J. (2006). Sticking of atomic hydrogen on the tungsten (0 0 1) surface. *Surface Science*, 600(16), 3174. <https://doi.org/10.1016/j.susc.2006.06.001>

[68] Zheng, W., & Gallagher, A. (2006). Hydrogen dissociation on high-temperature tungsten. *Surface Science*, 600(10), 2210. <https://doi.org/10.1016/j.susc.2006.03.032>

[69] Guterl, J., Smirnov, R. D., & Snyder, P. (2019). Effects of surface processes on hydrogen outgassing from metal in desorption experiments. *Nuclear Fusion*, 59(9), 96042. <https://doi.org/10.1088/1741-4326/ab280a>

[70] Alnot, P., Cassuto, A., & King, D. (1989). Adsorption and desorption kinetics with no precursor trapping: Hydrogen and deuterium on W {100}. *Surface Science*, 215(1), pg. 29-46.

[71] Emrich, Jr., William J. (2016). Principles of Nuclear Rocket Propulsion. In *Principles of Nuclear Rocket Propulsion*. Elsevier Science & Technology. pg. 132, 137

[72] Gorrell, A., Morris, M., & Chen, Y.-T. (2023). Non-equilibrium behavior of dissociated hydrogen in historic Nuclear thermal propulsion reactors. *Nuclear Engineering and Design*, 413, 112494., 6. <https://doi.org/10.1016/j.nucengdes.2023.112494>

[73] Johnson, D. F., & Carter, E. A. (2010). Hydrogen in tungsten: Absorption, diffusion, vacancy trapping, and decohesion. *Journal of Materials Research*, 25(2), 316. <https://doi.org/10.1557/JMR.2010.0036>

[74] Gorrell, A., Morris, M., & Chen, Y.-T. (2023). Non-equilibrium behavior of dissociated hydrogen in historic Nuclear thermal propulsion reactors. *Nuclear Engineering and Design*, 413, 112494., 6. <https://doi.org/10.1016/j.nucengdes.2023.112494>.

[75] Smith, A., Barker, R., & Estrup, P. (1984). Desorption of hydrogen from tungsten (100). *Surface Science*, 136(2), pg. 331.

[76] Madey, T. E. (1973). Chemisorption of H₂ on W(100): Absolute sticking probability, coverage, and electron stimulated desorption. *Surface Science*, 36(1), 281–294.
[https://doi.org/10.1016/0039-6028\(73\)90262-8](https://doi.org/10.1016/0039-6028(73)90262-8) pg. 284-285

[77] Alnot, P., Cassuto, A., & King, D. (1989). Adsorption and desorption kinetics with no precursor trapping: Hydrogen and deuterium on W {100}. *Surface Science*, 215(1), pg. 29-46.

[78] Forni, A., Desjonquères, M. C., Spanjaard, D., & Tantardini, G. F. (1992). A Monte Carlo quasi-classical trajectories study of the chemisorption of hydrogen on the W(001) surface. *Surface Science*, 274(1), 165. [https://doi.org/10.1016/0039-6028\(92\)90110-R](https://doi.org/10.1016/0039-6028(92)90110-R)

[79] Butler, D. A., Hayden, B. E., & Jones, J. D. (1994). Precursor dynamics in dissociative hydrogen adsorption on W (100). *Chemical Physics Letters*, 217(4), 427.
[https://doi.org/10.1016/0009-2614\(93\)E1395-W](https://doi.org/10.1016/0009-2614(93)E1395-W)

[80] Busnengo, H. F., & Martínez, A. E. (2008). H₂ Chemisorption on W(100) and W(110) Surfaces. *Journal of Physical Chemistry. C*, 112(14), 5584. <https://doi.org/10.1021/jp711053c>

[81] Smith, A., Barker, R., & Estrup, P. (1984). Desorption of hydrogen from tungsten (100). *Surface Science*, 136(2), pg. 331

[82] Alnot, P., Cassuto, A., & King, D. (1989). Adsorption and desorption kinetics with no precursor trapping: Hydrogen and deuterium on W {100}. *Surface Science*, 215(1), pg. 35.

[83] Hodille, E. A., Markelj, S., Pecovnik, M., Ajmalghan, M., Piazza, Z. A., Ferro, Y., Schwarz-Selinger, T., & Grisolia, C. (2020). Kinetic model for hydrogen absorption in tungsten with coverage

- [84] Johnson, D. F., & Carter, E. A. (2010). Hydrogen in tungsten: Absorption, diffusion, vacancy trapping, and decohesion. *Journal of Materials Research*, 25(2), pg. 315–327. <https://doi.org/10.1557/JMR.2010.0036>
- [85] Zheng, W., & Gallagher, A. (2006). Hydrogen dissociation on high-temperature tungsten. *Surface Science*, 600(10), 2210. <https://doi.org/10.1016/j.susc.2006.08.010>
- [86] Johnson, D. F., & Carter, E. A. (2010). Hydrogen in tungsten: Absorption, diffusion, vacancy trapping, and decohesion. *Journal of Materials Research*, 25(2), pg. 321, Table 1. <https://doi.org/10.1557/JMR.2010.0036>
- [87] White, F. (1974). *Viscous fluid flow*. New York: McGraw-Hill. Figure 6-44, 6-45 pg. 492-493
- [88] Gorrell, A., Morris, M., & Chen, Y.-T. (2023). Non-equilibrium behavior of dissociated hydrogen in historic Nuclear thermal propulsion reactors. *Nuclear Engineering and Design*, 413, 112494., pg. 5. <https://doi.org/10.1016/j.nucengdes.2023.112494>
- [89] Lushchik, V. G., Makarova, M. S., & Popovich, S. S. (2023). Numerical Investigation of the Influence of the Coolant's Prandtl Molecular Numbers and the Permeability of the Pipe Wall on Turbulent Heat Transfer. *Thermal Engineering*, 70(12), 1038. <https://doi.org/10.1134/S0040601523120091>
- [90] White, F. (1974). *Viscous fluid flow*. New York: McGraw-Hill. Figure 6-44, 6-45 pg. 492-493
- [91] White, F. (1974). *Viscous fluid flow*. New York: McGraw-Hill. Figure 6-44, 6-45 pg. 492-493
- [92] White, F. (1974). *Viscous fluid flow*. New York: McGraw-Hill. Figure 6-45 pg. 493
- [93] Ibid.

[94] Ibid.

[95] White, F. (1974). *Viscous fluid flow*. New York: McGraw-Hill. pg. 140

[96] Pelaccio, D. G., El-Genk, M. S., & Butt, D. P. (1995). Hydrogen corrosion considerations of carbide fuels for nuclear thermal propulsion applications. *Journal of Propulsion and Power*, 11(6), 1341. <https://doi.org/10.2514/3.2397>

[97] Emrich, J., William J. (2023). *Principles of nuclear rocket propulsion (Second edition..)*. Butterworth-Heinemann. 152.

[98] Angelo, J. A., & Buden, D. (1985). *Space nuclear power (Original ed.)*. Orbit Book Co. 184.

[99] ANSYS Fluent Theory Guide, ANSYS 2023, R2, Section 24.6. 984.

[100] ANSYS Fluent User Manual, ANSYS 2023, R2, Section 1.2.

[101] ANSYS Fluent Theory Guide, ANSYS 2023, R2, Section 7.1.1. 228.

[102] White, F. M. (2006). *Viscous fluid flow (Third Ed.)*. McGraw-Hill., 449

[103] Menter, F. R. (1993), "Zonal Two Equation $k-\omega$ Turbulence Models for Aerodynamic Flows", AIAA Paper 93-2906.

[104] White, F. M. (2006). *Viscous fluid flow (Third Ed.)*. McGraw-Hill., 493

[105] Yang, X.-Y., Lu, Y., & Zhang, P. (2016). First-principles study of the stability and diffusion properties of hydrogen in zirconium carbide. *Journal of Nuclear Materials*, 479, 130–136. <https://doi.org/10.1016/j.jnucmat.2016.07.008>

[106] Wallace, T. C., & Butt, D. P. (n.d.). Review of diffusion and vaporization of Group 4 and 5 transition metal carbides. In *The Chemistry of Transition Metal Carbides and Nitrides* (pp. 53–90). Springer Netherlands. https://doi.org/10.1007/978-94-009-1565-7_3

[107] Gulbransen, E. A., & Andrew, K. F. (1954). Diffusion of Hydrogen and Deuterium in High Purity Zirconium. *Journal of the Electrochemical Society*, 101(11), 560–566. <https://doi.org/10.1149/1.278115>

[108] McBride, B., & Gordon, S. Computer Program for Calculation of Complex Chemical Equilibrium Compositions and Applications, NASA Lewis Research Center, pg. 1

[109] Gordon, S. & Bride, B. Finite Area Combustor Theoretical Rocket Performance, NASA Lewis Research Center, pg. 1-3

[110] Stubbs, et.al. Analysis of nuclear thermal propulsion systems using computational fluid dynamics, <https://doi.org/10.1063/1.43055>

[111] Sutton, G. P., & Biblarz, O. (2017). *Rocket propulsion elements* (Eighth edition). Wiley. 404.

[112] Angelo, J. A., & Buden, D. (1985). *Space nuclear power* (Original ed.). Orbit Book Co. 179.

Curriculum Vitae

Lieutenant Colonel R. Adam Gorrell

mobile.rag@gmail.com

Education

Doctor of Philosophy in Mechanical Engineering May 2024
University of Nevada, Las Vegas, NV

Master of Science in Operational Art and Strategy June 2016
Air University, Montgomery, AL

Master of Engineering in Space Operations June 2010
University of Colorado, Colorado Springs, CO

Bachelor of Science in Aerospace Engineering May 2004
Missouri University of Science and Technology, Rolla, MO

Publications and Research

Gorrell, R., Chen, Y. (2024). *Rocket chamber conditions from analytical velocity, temperature profiles of dissociated hydrogen in nuclear propulsion*. AIAA Journal of Propulsion and Power (In Preparation)

Gorrell, R., Chen, Y. (2024). *Boundary layer effects from adsorption, desorption, and absorption of dissociated hydrogen in the cladding of nuclear thermal propulsion reactors*. Intl. Journal of Hydrogen Energy, 69, 1036

Gorrell, A., Morris, M., & Chen, Y. (2023). *Non-equilibrium behavior of dissociated hydrogen in historic nuclear thermal propulsion reactors*. Nuclear Engineering and Design, 413, 112494.

Gorrell, R., MacPhail, A. and Rice, J. (2016). *Countering A2/AD with Swarming*, Air Command and Staff College, Air University, AD1031572

“Technology Innovation Study Panel: Countering Small Unmanned Aircraft Systems” presentation for the USAF Chief Scientist, Technology Innovations Study Panel, March 2015

Teaching Experience

Astronautics Instructor & Asst. Professor, Department of Astronautics May 2013 – June 2015
United States Air Force Academy, Colorado Springs, CO

- Taught Astro Engr 310, Intro. to Astronautics, 5 semesters, 60 students per term, 300 total.
- Taught Astro Engr 351, Rocket Propulsion, 2 semesters, 15 students per term, 30 total.

Awards: Engineering Division Award (#1/45), Dept. Instructor Award (#1/17, Peer Selected), 2 x Senior-Officer Award, #1/4 Rookie Instructors, “Top 1% of Majors in my Career” (Dpt. Head)

Instructor, Unmanned Aircraft Flight Test, Department of Aeronautics August 2014 – June 2015
United States Air Force Academy, Colorado Springs, CO

- Taught Sys Engr 365, Flight Test Fundamentals, 2 semesters, 8 students per term, 16 total.
- Airworthiness authority, UAS test manager for the US Air Force Academy Research Center.

Affiliations

Senior Member, *American Institute of Aeronautics and Astronautics* January 2001 – Present
Member, *Tau Beta Pi* February 2023 – Present
Member, *American Society of Mechanical Engineers* November 2023 – Present

Work Experience

Commander, MQ-9 Launch and Recovery Training March 2022 – March 2024
11th Attack Squadron, Creech AFB, NV

- Led hiring, development, and training for 90 military, civilian, and contract personnel.
- Trained launch and recovery aircrew for 4 worldwide geographic regions & 7 United States.

Staff Officer January 2022 – March 2022
432nd Operations Group, Creech AFB, NV

Director of Operations, MQ-9 Launch and Recovery Training June 2020 – January 2022
11th Attack Squadron, Creech AFB, NV

- Led flight training of 320 student aircrew to launch and land the MQ-9 in combat zones.
- Supervised 70 active duty and contract personnel in daily flight training operations.

Ready/Deployed Launch and Recovery Pilot June 2019 – June 2020
489th Attack Squadron, Creech AFB, NV
Kandahar Air Base, Afghanistan

Commander, MQ-9 Operational Test and Evaluation May 2016 – June 2019
Detachment 4, 53rd Test Management Group, Creech AFB, NV

- Led 50 engineers, analysts, aircrew in \$500K of acquisition, testing, & program management
- Tested guidance, sensors, and weapons on the MQ-9 for senior-leader deployment decisions.

Graduate Student June 2015 – May 2016

Air Command and Staff College, Air University, Montgomery, AL

Awards: Distinguished Graduate (Top 10% of all graduates)

Selected to Dean's Research Group, Top 6% of graduate research.

Astronautics Instructor & Asst. Professor, Department of Astronautics May 2013 – June 2015
United States Air Force Academy, Colorado Springs, CO

Instructor, Unmanned Aircraft Flight Test, Department of Aeronautics August 2014 – June 2015
United States Air Force Academy, Colorado Springs, CO

- Secured \$25K in RDT&E funding for UAS research & flight test with the Dept. of Research

MQ-9 Operational Test Pilot and Program Manager May 2010 – May 2013
556th Test and Evaluation Squadron, Creech AFB, NV

Awards: US Air Force Warfare Center Flight Commander of the Year

- Evaluated wide-area airborne sensors for city-wide surveillance & forensic terrorist activity.
- Developed the Electronic Combat Officer's Course for self-protect of MQ-9 Command Link.

MQ-9 Combat Pilot and Deployed Pilot March 2008 – May 2010
42nd Attack Squadron, Creech AFB, NV
Kandahar Air Base, Afghanistan

- Provided persistent attack and reconnaissance for Operations Enduring and Iraqi Freedom.

B-1B Lancer Pilot August 2005 – March 2008
9th Bomb Squadron, Dyess AFB, TX

Al Udeid Air Base, Qatar

Awards: Distinguished Graduate

- Piloted the USAF's supersonic bomber in Operations Enduring and Iraqi Freedom.